A NEW METHOD FOR MELT DETECTION ON ANTARCTIC ICE-SHELVES AND SCATTEROMETER CALIBRATION VERIFICATION

by

Lukas B. Kunz

A thesis submitted to the faculty of

Brigham Young University

in partial fulfillment of the requirements for the degree of

Master of Science

Department of Electrical and Computer Engineering

Brigham Young University

December 2004

BRIGHAM YOUNG UNIVERSITY

GRADUATE COMMITTEE APPROVAL

of a thesis submitted by

Lukas B. Kunz

This thesis has been read by each member of the following graduate committee and by majority vote has been found to be satisfactory.

Date   David G. Long, Chair

Date   Karl F. Warnick

Date   A. Lee Swindlehurst

ABSTRACT

A NEW METHOD FOR MELT DETECTION ON ANTARCTIC ICE-SHELVES AND

SCATTEROMETER CALIBRATION VERIFICATION

Lukas B. Kunz

Department of Electrical and Computer Engineering

Master of Science

Ku-band dual-polarization radar backscatter measurements from the SeaWinds on QuikScat scatterometer and microwave radiometer measurements from the Special Sensor Microwave/Imager (SSM/I) are used to determine periods of surface melt and freeze in the Antarctic ice-shelves. The normalized radar backscatter (σ^o) and backscatter polarization ratio (PR) are used in the maximum likelihood estimation of the ice-state. This method is used to infer the daily ice-surface conditions for 25 selected study points located on the Ronne, Ross, Larsen, Fimbul, Amery, and Shackleton Ice-shelves. The temporal and spatial variations of the radar response are also observed for various neighborhood sizes surrounding each given point during the study period.

Criteria for determining the dates of melt-onset and freeze-up for each Austral summer are also presented. Validation of the ice-state and melt-onset date estimates is performed by analyzing corresponding brightness temperature (T_b) measurements from radiometers. QuikScat σ^o measurements from 1999 through 2003 are analyzed and it is shown that Ku-band scatterometers are very useful for determining periods of melt in Antarctic ice-sheets

and provide high temporal and spatial resolution ice-state estimates. These estimates can be important for long-term studies of the climatic effects of the seasonal and inter-annual melting of the Antarctic ice-sheets.

The SeaWinds on QuikScat (QuikScat) and SeaWinds on ADEOS-2 (SeaWinds) scatterometers are identical radar sensors on different spaceborne platforms traversing similar orbits. QuikSCAT and SeaWinds data are used to infer near-surface wind vectors, polar sea-ice extent, polar-ice melt events, among others. In order to verify the relative calibration of these two sensors a simple cross-calibration method is implemented based on land measurements. A first-order polynomial model for the incidence angle dependence of σ^o is used to account for biases in the σ^o measurements. This model is applied to selected regions of the Amazon rainforest and the Sahara desert. It is shown that the two sensors are well calibrated. Additionally, evidence of a previously presumed diurnal cycle in the Amazon rainforest backscatter is given.

ACKNOWLEDGMENTS

Contents

List of Tables

List of Figures

Chapter 1

Introduction

For centuries the polar regions of the Earth have been the object of curiosity and the destination of many expeditions. Perilous journeys into these extreme environs have cost many men and women their lives in the pursuit of knowledge and adventure. Much of our understanding about these areas and their impact on the global climate is a direct result of such early explorations.

The more recent concerns of global warming and changing weather patterns have fueled the excitement for continued study of the polar ice-sheets. The inter-annual variation of the conditions of these ice-sheets is of primary interest as significant changes or trends may be linked with changes in the global climate. Specifically, the time of year marking the beginning and end of seasons of surface melting on the ice-sheets is of considerable importance. Accurate observations of this behavior are critical in order to facilitate our understanding of global geophysical conditions.

Until the past few decades, observations of weather and the physical state of the polar ice-sheets were possible only by making on site measurements. The harsh weather of these regions makes such *in situ* observations very challenging and sometimes dangerous. The advent of satellite-based remote sensing has provided the means for making daily global observations. In particular, satellite sensors in polar orbits collect measurements over the entire Arctic and Antarctic regions many times a day, offering unprecedented information about these areas with high temporal and spatial resolution.

A distinct advantage of spaceborne radar instruments is that they can be configured to observe a wide range of properties of the Earth's surface. Sensors tuned to optical frequencies provide snapshot views of the Earth with remarkable clarity and high-precision detail. Such

sensors are useful for observing hurricanes, land topography, and other surface conditions, but are limited by clouds. Radar instruments operating at much lower frequencies can penetrate clouds and the surface layer and gather additional information. These observations are at a much coarser resolution than optical sensors.

Microwave instruments have shown great utility for use in polar studies. These sensors are particularly useful since they do not rely upon solar illumination of the imaging surface to make observations and are unaffected by cloud cover. Much of the polar regions are frequently obscured by clouds that obstruct the view of optical sensors.

Microwave radar is divided into two categories, passive and active. Active instruments called scatterometers transmit pulses of electromagnetic energy toward the desired target and measure the power reflected back to the sensor. These measurements are called backscatter. Passive sensors, or radiometers, do not transmit energy. Instead, they observe the power radiated by the surface, measured by the brightness temperature. These sensors are affected by energy radiated from cloud cover.

A significant number of studies have been conducted using spaceborne passive microwave sensors to detect the surface melt of Arctic sea-ice [1, 2, 3]; however, the use of active microwave sensors in such studies has been limited [4]. Even more limited has been the use of active instruments in detecting surface melt on Antarctic sea-ice [5] and on Antarctic ice-shelves. Measurements from active microwave sensors are very sensitive to changing ice-surface conditions and are useful in determining annual melt-season duration and in observing the formation of melt ponds. Recently, the presence of surface melt ponds on Antarctic shelf-ice and longer melt-season duration have been linked to shelf break-up [6].

This thesis presents a new method for exploiting the sensitivity of active microwave measurements in order to determine the presence of surface melt on Antarctic ice-shelves. To our knowledge this is the first study of melt seasons over the Antarctic ice-shelves using scatterometers. The data collected by the SeaWinds on QuikSCAT (QuikSCAT) scatterometer from 1999 through 2003 is analyzed using this melt detection method. These melt classification results are compared with results from several passive microwave melt detection methods applied to data recorded by the Special Sensor Microwave Imager (SSM/I) radiometers from the same time period.

A maximum likelihood (ML) approach is employed to determine daily ice-state classifications from QuikSCAT backscatter measurements. Yearly maps of melt-onset dates are created and the total number of days classified as melt is also given for each year. It is shown that these ice-state and melt-onset date estimates not only agree with corresponding estimates from SSM/I data but provide added insight from the higher spatial-resolution and increased sensitivity achieved by using an active microwave system.

This thesis also examines the sensor calibration of QuikSCAT and SeaWinds on ADEOS-2 (SeaWinds). SeaWinds is a scatterometer with specifications identical to those of QuikSCAT and was operational during 2003. This calibration verification evaluates the compatibility of measurements from different instruments and also between different antennas within the same sensor. The measurements collected by spaceborne instruments are used in numerous areas of research and inferring geophysical phenomena from this data relies heavily upon the accuracy of the given measurements. Post-launch calibration and verification is required to ensure that such measurements are valid for use in such applications.

The QuikSCAT and SeaWinds scatterometers are instruments that yield a particularly useful data set since the two sensors are identical and follow similar orbital paths. Combining data from these sensors provides high spatial- and temporal-resolution with increased insight into the diurnal cycle. Proper calibration of these instruments is essential in order to maximize the utility of the combined data.

A relative calibration method is proposed and applied to data collected by QuikSCAT and SeaWinds. Measurements from 2003 Julian Day 169 to Julian Day 224 are used to evaluate the relative calibration in the backscatter values. The data set used in the analysis comes from selected subregions of the Amazon rain forest, the entire Amazon region spatially masked as described by Zec, Long, and Jones [7], and a spatially masked region of the Sahara desert in northern Africa.

The results from the sensor calibration yield evidence of diurnal variation in the Amazon's radar response and indicate that the QuikSCAT and SeaWinds instruments are relatively calibrated to within ∼0.05dB. The melt classifications performed by the ML melt detection method are shown to match well with results from previous algorithms for radiome-

3

ter data. The melt detected by the ML method also illustrates the inter-annual variation of the onset, duration, and extent of melt seasons on Antarctic ice-shelves.

Discussions of the instruments used, the methodologies implemented, and results obtained are organized as follows. Chapter 2 provides background into the principles of active and passive microwave radar and Chapter 3 contains the explanation of the proposed melt detection method as well as results. Chapter 4 discusses the calibration of the two scatterometers and offers results and Chapter 5 concludes the work and suggests areas of future research. Appendix A and Appendix B contain extended results from the melt detection application and sensor calibration, respectively.

Chapter 2

Background

This chapter discusses the specifications of the QuikSCAT, SeaWinds, and SSM/I instruments. QuikSCAT and SeaWinds are active microwave systems and the SSM/I sensors are passive microwave systems. The basic theory behind each system type is summarized and the application of both systems to melt detection is illustrated.

2.1 QuikSCAT and SeaWinds

The SeaWinds on QuikSCAT (QuikSCAT) scatterometer [8] was launched in June 1999 and remains operational to this date. It was designed to measure vector winds over the ocean and transmits electromagnetic pulses at 13.6 GHZ (Ku-band). This instrument has two scanning pencil-beam antennas. The inner beam has a nominal incidence angle of 46° and traces out a 1400km-wide swath on the Earth's surface. It measures the horizontal ('h') polarization backscatter. The outer beam measures vertical ('v') polarization backscatter at an incidence angle of ∼54°. Its footprint traces out a 1800km-wide swath. The polar orbiting QuikSCAT provides daily complete coverage of the polar regions and ∼92% of the Earth's surface regardless of cloud cover or solar illumination. As a result, QuikSCAT is well-suited for polar studies.

The SeaWinds on ADEOS-2 (SeaWinds) scatterometer was launched in December 2002 and has identical specifications as QuikSCAT. The SeaWinds mission ended prematurely due to a failure in the power system. Data from its mission is available from Julian Day 100 to JD 297 of 2003.

Although these sensors are identical, their respective platforms are different. The QuikSCAT orbital attitude is more stable than its ADEOS-2 counterpart. The QuikSCAT

satellite is in a geodetic orbit so the spacecraft is always oriented with respect to the Earth's local normal. The ADEOS-2 satellite is in a geocentric orbit where the spacecraft orientation reference is the center of the Earth. If the Earth were a perfect sphere these orbits would be identical. But, since the Earth is slightly ellipsoidal, a satellite in geocentric orbit does not always point normal to the Earth's surface whereas a satellite in geodetic orbit does maintain the correct orientation. As a result, there is a larger standard deviation in incidence angle for SeaWinds than QuikSCAT.

The SeaWinds instrument trails QuikSCAT along its orbital path and crosses the equator on ascending and descending passes approximately 6 hours after QuikSCAT. This temporal sampling is key in observing diurnal variation of backscatter measurements. These issues are discussed in more detail in Chapter 4.

2.1.1 Active Microwave Theory

Active microwave theory is based on the amount of power reflected by the imaging surface when electromagnetic energy is transmitted incident to the surface. Spaceborne scatterometers are active microwave sensors that transmit pulses toward the Earth's surface and observe the power that is reflected back to the instrument (backscatter). Figure 2.1 illustrates the surface interaction of incident electromagnetic pulses. The radar cross section (σ) of a surface depends on its size, orientation, shape, and material and is related to the transmitted (P_t) and received (P_r) power by the radar equation [9]

$$P_r = \frac{P_t G^2 \lambda^2 \sigma}{(4\pi)^3 R^4},\tag{2.1}$$

where λ is the wavelength in meters, G is the antenna gain, and R is the distance from the antenna to the surface. The backscatter (σ^o) is the radar cross section normalized by the area of the antenna footprint. This is the quantity of primary interest in active microwave remote sensing applications.

These measurements depend upon the dielectric properties and roughness of the surface as well as the operating frequency of the transmitter and may vary in both azimuth and incidence angle. σ^o values are particularly sensitive to the water content of the illuminated surface since the amount of water greatly affects the dielectric constant describing the surface.
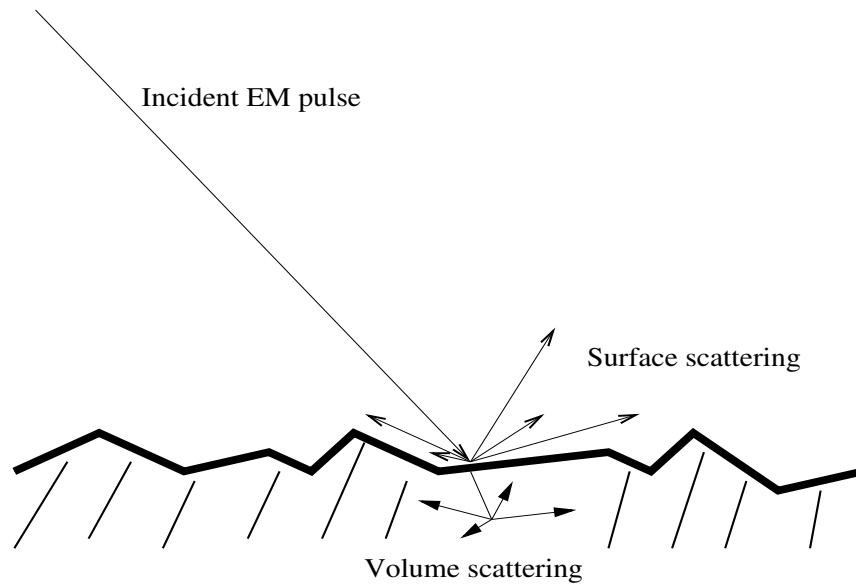
Figure 2.1: The surface and volume scattering of an incident electromagnetic pulse transmitted by a scatterometer. The scattered energy depends upon the incidence and azimuth angles and frequency of the transmitted pulse as well as the roughness and material composition of the surface. There is some contribution to the backscatter over ice from volume scattering, but most of the reflected power is due to surface scattering.

The backscatter signatures observed from illuminating snow-covered ice and liquid water are markedly different [10]. Volume scattering is the predominant factor in the radar response to dry snow cover for active microwave sensors. As the amount of liquid water in the snow cover increases, the wet snow at the surface causes a dramatic decrease in the radar backscatter [11]. These backscatter signatures are of primary interest in the analysis presented in Chapter 3.

7

2.2 SSM/I

The Special Sensor Microwave Imager (SSM/I) radiometers are passive microwave instruments on board Defense Meteorological Satellite Program (DMSP) satellites. These sensors provide a data set covering 1988 to the present. The SSM/I radiometers measure the brightness temperature (T_b) of the Earth's surface on seven channels: dual-polarization at 19.35, 37.0, and 85.5 GHz, and 'v'-pol at 22.235 GHz. Each channel provides insight into the surface properties of the imaging area at different depths. These instruments provide complete coverage of the polar regions many times each day.

2.2.1 Passive Microwave Theory

The mechanism in passive microwave theory differs from active microwave systems. No energy is transmitted by the sensor toward the imaging surface. Instead, observations are made of energy emitted by the surface itself. This presentation follows Ulaby et al [12]. All physical materials radiate electromagnetic energy. *Blackbodies* are idealized materials that perfectly absorb all incident radiated energy and perfectly emit radiation. The physical temperature (T) of a blackbody is related to its radiated energy, or spectral brightness (B_f), through Planck's radiation law

$$B_f = \frac{2hf^3}{c^2(e^{hf/kT} - 1)},$$

(2.2)

where h is Planck's constant, f is the frequency in Hertz, k is Boltzmann's constant, and c is the speed of light in meters per second. For frequencies below $\sim$100 GHz the Rayleigh-Jeans approximation simplifies the relationship to

$$B_f = \frac{2kT}{\lambda^2},$$

(2.3)

where λ is the wavelength in meters.

No materials act as perfect blackbodies, and as a result they emit less radiation and are unable to absorb all incident energy. The energy radiated is incidence and azimuth angle dependent whereas the radiation is uniform in all directions for blackbodies. A metric called the brightness temperature (T_b) relates the physical temperature of an object to how well it represents a perfect blackbody. The emissivity ($e(\theta, \phi)$) of a material is defined as the ratio

of its brightness to the spectral brightness of a blackbody at the same physical temperature. Consequently, the emissivity, physical temperature, and brightness temperature are related by

$$T_b(\theta, \phi) = e(\theta, \phi)T. \tag{2.4}$$

The emissivity is positive and less than one for real materials so the observed brightness temperature is always less than the actual physical temperature of the object. Thus, ascertaining the true physical temperature of an object requires knowledge of the material's emissivity.

Further complicating the determination of the physical temperature are the effects of atmospheric radiation illustrated in Figure 2.2. Downwelling (T_{dn}) and upwelling (T_{up}) atmospheric radiation and surface-scattered (T_{sc}) radiation are also observed along with the brightness temperature. Usually these contributions are much less than the actual brightness temperature; however, for certain frequencies and weather conditions the effects are more severe.

The brightness temperature measurements from radiometers are useful in analyzing the content of liquid water in the snow cover. The relative permittivity of wet snow is considerably higher than for dry snow, so absorption is higher and results in a decrease of volume scattering. As liquid water is introduced into the snow layer the imaginary part of the dielectric constant increases significantly. This increases the emissivity and causes the brightness temperature of the wet snow to dramatically increase [11]. This behavior motivates the use of radiometers in detecting surface melt of polar ice-sheets.

The principles of active and passive microwave theory discussed in this chapter are the bases for algorithms used to detect melting of snow-cover over ice surfaces. Chapter 3 presents a new method to detect melt using active microwave observations and also contains results from several algorithms for passive microwave data to detect surface melt. The properties of backscatter from active microwave systems are used in a scatterometer calibration method explained in Chapter 4.
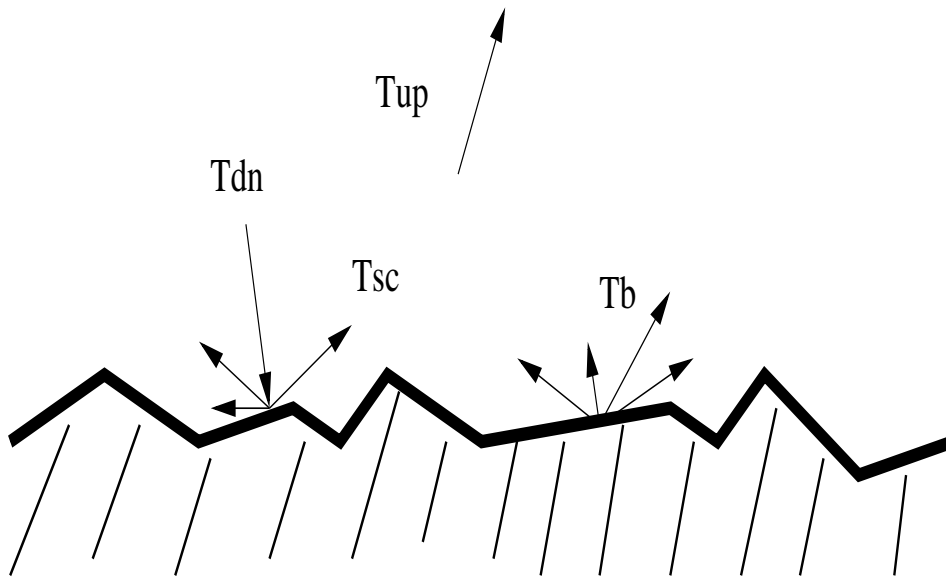
Figure 2.2: Atmospheric radiation interferes with the observation of brightness temperatures (T_b). T_{db} is downwelling radiation that results in scattering (T_{sc}) and T_{up} is upwelling radiation. Each of these contribute to noise that masks the true surface brightness temperature.

Chapter 3

Melt Detection of Antarctic Ice-shelves

Spaceborne passive microwave sensors have been used to detect the surface melt of Arctic sea-ice [1, 2, 3] and the Greenland ice-sheet [13, 14]; however, the use of active microwave sensors in such studies has been limited [4]. The use of these instruments in detecting surface melt on Antarctic sea-ice [5] and on Antarctic ice-shelves is even more limited. Recently, longer melt season duration and the presence of surface melt ponds on Antarctic ice-shelves have been linked to shelf break-up [6]. Active microwave measurements are very useful in determining annual melt season duration and in observing surface melt pond formation. These measurements are also sensitive to changing ice-surface conditions that may indicate the initial signs of shelf retreat. This chapter proposes a method to determine the presence of surface melt on Antarctic ice-shelves that exploits the sensitivity of active microwave measurements.

A maximum likelihood (ML) approach is employed to determine daily ice-state classifications from active microwave backscatter measurements. The yearly progression of melt-onset dates is mapped and the total number of days classified as melt is also given for each year. The ML ice-state and melt-onset date estimates agree with results from passive microwave data and yield more insight into the spatial variation of Antarctic surface melt.

Section 1 provides more background to the problem, Section 2 explains the calculation of the melt- and non-melt period distributions, Section 3 presents the ML melt detection method and some results, Section 4 discusses the criteria for determining melt-onset and refreeze dates as well as the mapped results, and Section 5 compares the ML method results with observations from radiometer measurements.

3.1 Background

As discussed in Chapter 2, scatterometer measurements are sensitive to the water content of the illuminated surface. Brightness temperature measurements from passive microwave radiometers are also useful in analyzing the content of liquid water in the snow cover. Several algorithms have been implemented on passive microwave data to map snowmelt-onset dates on Arctic sea-ice [4] and on the Greenland ice-sheet [14]. Similar algorithms are used in this paper in order to validate the melt detection results from the active microwave measurements.

High-resolution images of the measurements from the QuikSCAT scatterometer and the SSM/I radiometers produced using the Scatterometer Image Reconstruction (SIR) algorithm [15] are used in the analysis presented. This algorithm combines all passes from a given day to significantly improve the spatial resolution of the data images at the expense of some temporal resolution. The QuikSCAT SIR image data used in this study is available from the NASA Scatterometer Climate Record Pathfinder (SCP) project [16].

3.2 Ice-state Distribution Estimations

To observe the intra- and inter-shelf radar response characteristics, 25 points are selected from each of the major ice-shelves (Figure 3.1). The yearly and seasonal variations in the statistics of the measured backscatter values for each point are observed. These empirically calculated statistics form the basis of the ML test for ice-state estimation.
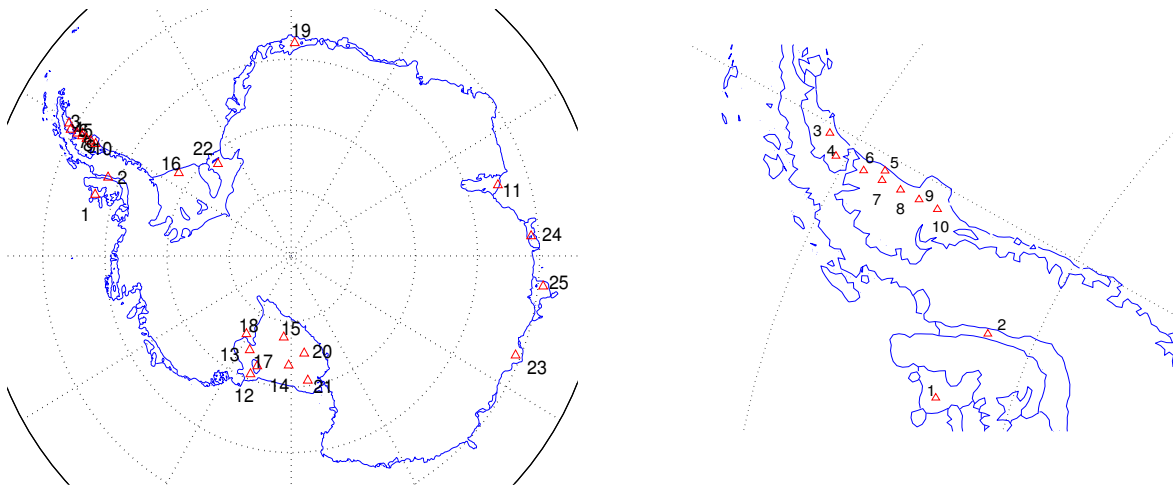
Figure 3.1: The 25 study points over Antarctic ice-shelves (left) with close-up of points 1-10 located on the Antarctic peninsula (right). See also Table 3.2.

Table 3.1: Latitude and longitude for each of the 25 study points.

Point	Longitude	Latitude
1	073.50°W	70.25°S
2	067.90°W	70.90°S
3	060.50°W	65.35°S
4	061.50°W	65.75°S
5	060.91°W	66.95°S
6	061.50°W	66.50°S
7	061.50°W	67.00°S
8	061.50°W	67.50°S
9	061.50°W	68.00°S
10	061.50°W	68.50°S
11	072.00°E	69.00°S
12	160.00°W	78.50°S
13	155.00°W	80.50°S
14	178.61°W	79.99°S
15	174.45°W	82.52°S
16	055.00°W	76.75°S
17	162.00°W	79.40°S
18	148.77°W	81.66°S
19	001.00°E	70.50°S
20	172.00°E	81.00°S
21	172.00°E	78.50°S
22	040.00°W	79.00°S
23	112.75°E	66.50°S
24	085.50°E	66.75°S
25	096.50°E	65.50°S

The QuikSCAT scatterometer dual-polarization backscatter measurements (σ_H^o and σ_V^o) are very correlated but exhibit different sensitivities to the presence of liquid water. This variable sensitivity is easily observed from the 'quasi' polarization ratio (PR) defined by

$$PR = \sigma_V^o - \sigma_H^o, \tag{3.1}$$

where the values are in dB. This is not a true polarization ratio since the 'v'- and 'h'-pol measurements are from different incidence angles. In general, σ_V^o is $\sim$1 dB below the typical σ_H^o values. From the time-series in Figure 3.2 we see that PR fluctuates much more during each Austral summer than the winter. This results from the greater sensitivity of 'h'-pol backscatter to liquid water in the snow cover than 'v'-pol backscatter. This time-series is typical of most areas that experience surface melting. Backscatter values for locations with no melt events are nearly constant with time.
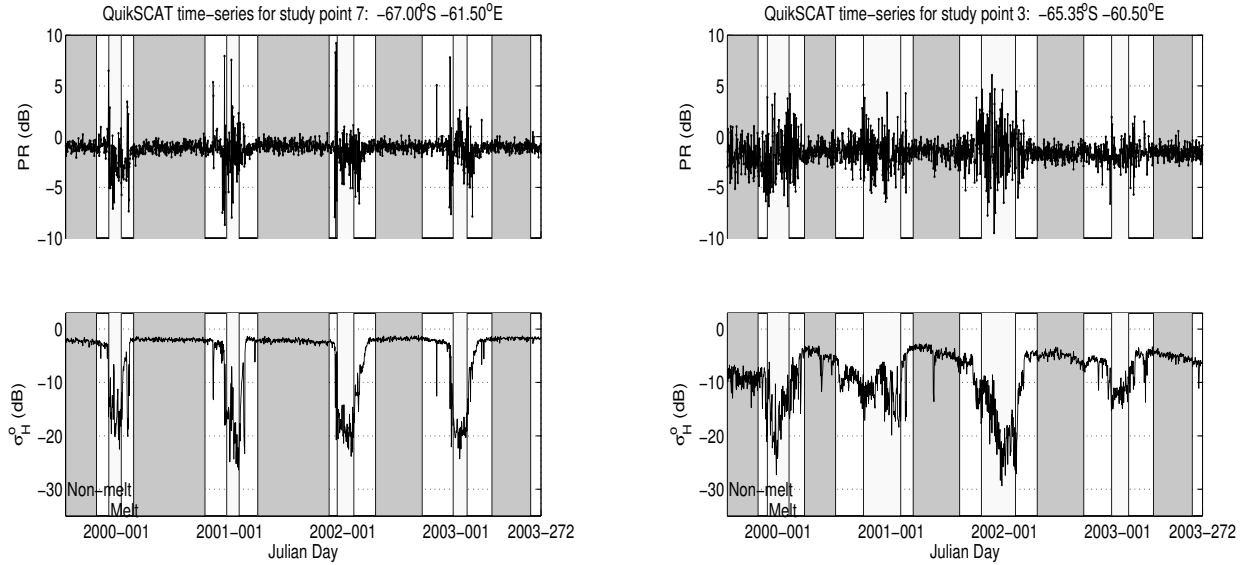
Figure 3.2: σ_H^o (bottom row) and PR (top row) time-series for study points 7 (left column) and 3 (right column) on the Larsen Ice-shelf. During each year, contiguous periods (shown as shaded and unshaded boxes) of alternating melt and non-melt are identified. Each period's mean and covariance are empirically computed and used in ML estimations of the daily ice-states. The variation in backscatter for point 3 is much more than for the other peninsular locations.
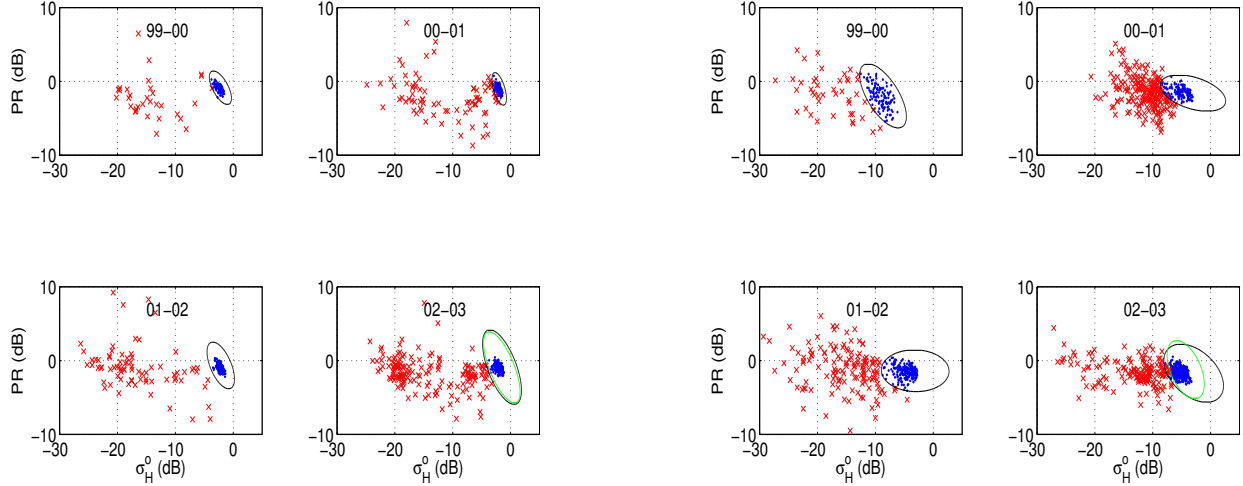
Figure 3.3: Yearly scatterplots of σ_H^o vs. PR for points 7 (left) and 3 (right). The ellipses are contours of equal Mahalonobis distance from the melt- and non-melt mean values illustrated in Figure 3.4.

Figure 3.3 shows corresponding scatterplots of σ_H^o vs. PR for each year of the time-series for points 7 and 3. Note the concentration of non-melt values around the point (-2 dB, -1 dB) in each plot for point 7. The remaining points, which are during summer melt, are loosely grouped. This suggests that the backscatter and PR observations during melting and non-melting periods may be modeled as random variables with separate means and covariances for melt and non-melt. For simplicity a gaussian distribution is assumed and the mean vector and covariance matrix during each specified period in Figure 3.2 are computed.

Figure 3.4 shows the resulting 1-σ contours for the QuikSCAT backscatter distributions during each year's melt- and non-melt periods for point 7. These contours describe fairly well the groupings from the scatterplots for this location shown in Figure 3.3. It is worth noting that the distributions are similar from year to year. The distributions calculated using all backscatter values from a neighborhood of radius 2.25 km and a larger neighborhood of radius 34 km for the study point are shown in Figure 3.4. There is very little change in the two distributions.

Study points 1-10 are all located on the Antarctic peninsula and have very similar non-melt and melt distributions (with the exception of point 3). These results indicate that the non-melt and melt distributions are approximately temporally- and spatially-invariant

16
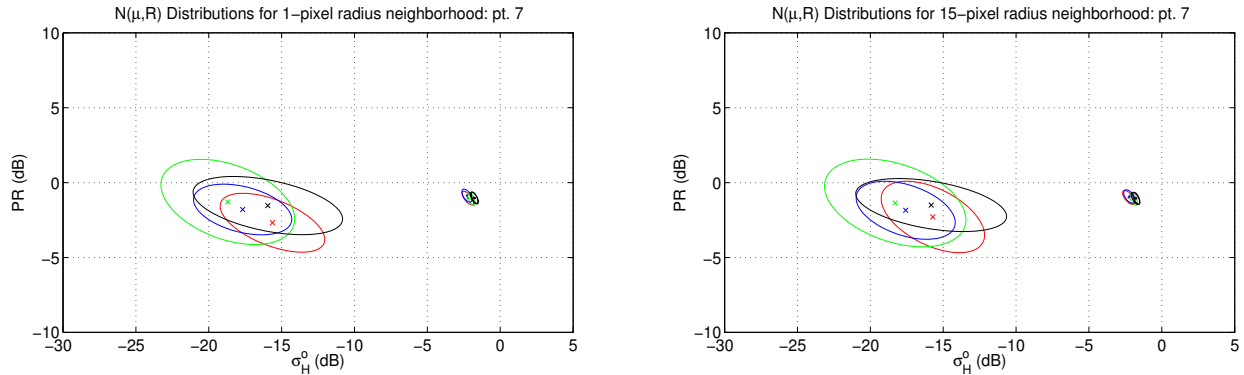
Figure 3.4: Yearly bivariate normal distribution 1-σ covariance contours for a 2.25km-radius (1-pixel radius) neighborhood (left) and a 34km-radius (15-pixel radius) neighborhood of study point 7 (right). The melt-period mean for each year is indicated by an 'x', and each year's non-melt mean by a dot at the middle of the respective contour. (The distributions for study points 1-10 are all similar.)

within a small local area. This invariance property generally does not hold for locations at ice-shelf boundaries, e.g. point 3.

Of particular interest is study point 3, the northern-most study point on the Larsen Ice-shelf. The time-series for this point varies significantly more than for the other peninsular points (Figures 3.2 and 3.3). Recently, this region has become the subject of interest for observing and understanding the causes and impacts of ice-shelf breakup [6]. In Section 5 the scatterometer observations for this location are shown to be more sensitive to changing shelf-surface conditions than passive microwave observations.

3.3 Maximum Likelihood Estimation of Ice-states

Given the scatterometer measurements, the daily ice-state for each location is inferred using the maximum likelihood ratio method,

$$l(\mathbf{x}) = \frac{f_{\mathbf{x}|H_1}(\mathbf{x}|h_1)}{f_{\mathbf{x}|H_0}(\mathbf{x}|h_0)} > \frac{L_{01}P(H_0)}{L_{10}P(H_1)}, \tag{3.2}$$

where $l(\mathbf{x})$ is the ratio of probability density functions $f_{\mathbf{x}|H_i}(\mathbf{x}|h_i)$ of $\mathbf{x}$ for each ice-state, H_0 denotes the conditions for no surface melting and H_1 represents the presence of surface melt, $\mathbf{x}$ is a two-element vector in the space spanned by the possible values of σ_H^o and PR, and $\mathbf{m_o}$ and $\mathbf{m_1}$ contain the estimated mean σ_H^o and PR values for the respective ice-states. L_{ij}

is the loss associated with choosing ice-state j when the true state of nature is i, and $P(H_i)$ is the prior probability that ice-state i is the true situation.

Bayes decision theory incorporates penalties for incorrect decisions in the form of loss functions and accounts for prior probabilities for the given states of nature [17]. For maximum likelihood estimation no *a priori* information is used and equal losses ($L_{01} = L_{10}$) are chosen. Assuming gaussian distributions the ratio test is

$$l(\mathbf{x}) = \frac{\frac{1}{2\pi|\mathbf{R_1}|^{1/2}}e^{-\frac{1}{2}(\mathbf{x}-\mathbf{m_1})^T\mathbf{R_1}^{-1}(\mathbf{x}-\mathbf{m_1})}}{\frac{1}{2\pi|\mathbf{R_0}|^{1/2}}e^{-\frac{1}{2}(\mathbf{x}-\mathbf{m_0})^T\mathbf{R_0}^{-1}(\mathbf{x}-\mathbf{m_0})}} > 1. \tag{3.3}$$

Forming the log-likelihood ratio $\Lambda(\mathbf{x}) = \log l(\mathbf{x})$ simplifies the hypothesis test to a comparison of weighted norms, the so-called Mahalonobis distance,

$$\phi(\mathbf{x}) = \begin{cases} 1 & \|\mathbf{x} - \mathbf{m_1}\|_{\mathbf{R_1}^{-1}} < \|\mathbf{x} - \mathbf{m_0}\|_{\mathbf{R_0}^{-1}} + \log\frac{|\mathbf{R_0}|}{|\mathbf{R_1}|} \\ 0 & \text{otherwise,} \end{cases} \tag{3.4}$$

where $\mathbf{R_0}$ and $\mathbf{R_1}$ are the respective covariance matrices for non-melt and melt conditions, $|\mathbf{R_i}|$ is the matrix determinant, and

$$\|\mathbf{x} - \mathbf{m_i}\|_{\mathbf{R_i}^{-1}} \overset{\triangle}{=} (\mathbf{x} - \mathbf{m_i})^T\mathbf{R_i}^{-1}(\mathbf{x} - \mathbf{m_i}). \tag{3.5}$$

The resulting test essentially scales the magnitude differences between a given $\mathbf{x}$ measurement vector and the non-melt and melt value vectors by the variance of the measurement under each case and chooses the shortest distance as the ice-state estimate.

This test is performed on the daily σ^o values for the 25 study points. Each day's measurements are used independently in the melt classification so the result from one day does not influence the ice-state estimation for any other day. The time-series data is divided into yearly segments and the mean and covariance from each given year are used in the ML test. For points that exhibit very few days of melting the covariance matrices empirically computed from the data are ill-conditioned. In these cases the covariance matrix from the nearest valid point is used instead. This substitution is necessary only for a few points on the Ronne and Ross Ice-shelves. Figure 3.5 illustrates the results of the ML ice-state estimation for point 7. The melt classification results for the other peninsular points are very similar.

This method performs well for this location since periods of reduced backscatter are classified as surface melt and periods of nearly constant σ^o_H are not. There are, however,
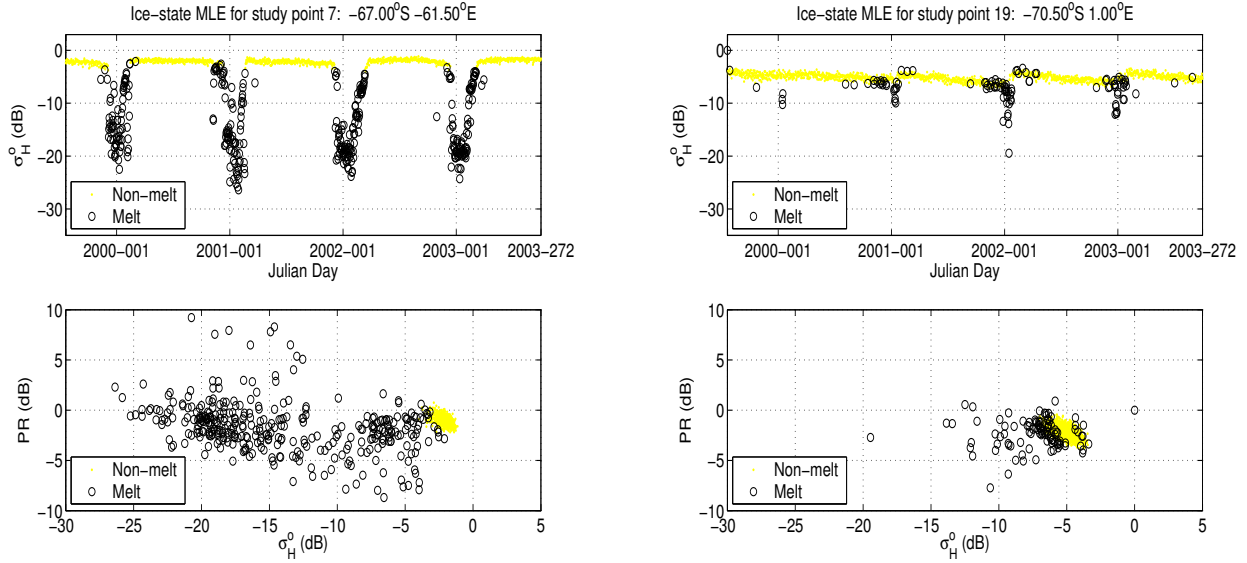
Figure 3.5: Time-series and scatterplots for study points 7 (left) and 19 (right) with resulting ML method surface-melt estimates. Note the presence of melt classifications for backscatter values higher than the winter mean for point 19.

some days during the summer with backscatter close to the winter mean value that are selected as melt events. This is observed in the melt classification results for many of the 25 study points.

Generally, the scatterometer measurements increase dramatically at the end of the Austral summer and indicate the onset of surface refreeze. Some years at the conclusion of the summer melt season, the backscatter measurements rise above the previous winter's mean value. Study point 24, located on the western Shackleton Ice-shelf, illustrates this behavior (Figure 3.6). The end of the 2000-2001 melt season is marked by σ_H^o values roughly 3 dB above the mean value for the previous winter of 2000. Note that this phenomenon follows a year of significantly more melt than the previous year.

Study point 19 more clearly shows that some potentially false melt classifications occur when backscatter measurements are higher than the winter non-melt values (Figure 3.5). This happens when the backscatter values lie to the right of the decision boundary in the σ_H^o vs. PR scatterplot (Figure 3.3). A slight modification to the decision boundary can compensate for this problem; however, since such measurements represent a distinct deviation from the normal non-melt conditions, the points classified as melt that have higher

19
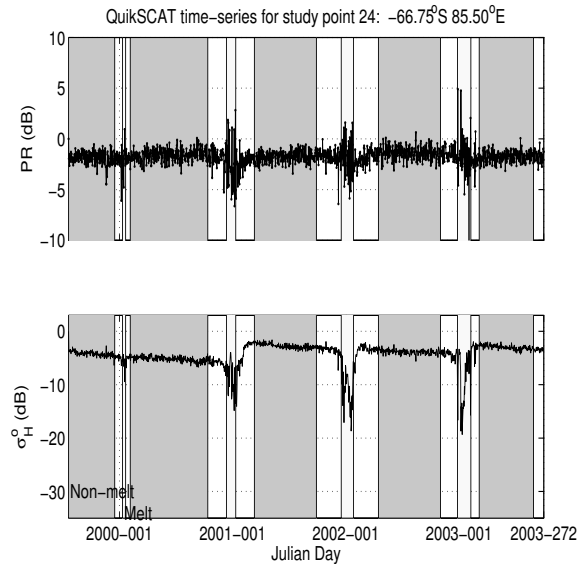
Figure 3.6: Time-series for study point 24. There is a significant increase in backscatter following the 2000-2001 melt season that rises ~3 dB above the previous winter's mean value.

backscatter values should be identified and analyzed further. Possible explanations for this behavior include a dramatic refreeze event, the formation of frost flowers, or a significant accumulation event, among others.

In order to validate the ice-state estimates from the dual-polarization maximum likelihood method, passive microwave observations are also analyzed. Section 5 compares the results from the ML algorithm for QuikSCAT with melt-detection results using algorithms developed for analyzing SSM/I brightness temperature measurements. A following section discusses mapping the progression of melt-onset and refreeze of the ice-shelves.

3.3.1 Motivation for 2-D Detection Threshold

Previous methods for melt detection over the Greenland ice-sheet used data from only one polarization of the QuikSCAT observations [14]. For completeness a comparison between the ML melt detection method using dual-polarization measurements and the ML method using only 'h'-pol backscatter is presented for some of the study points.
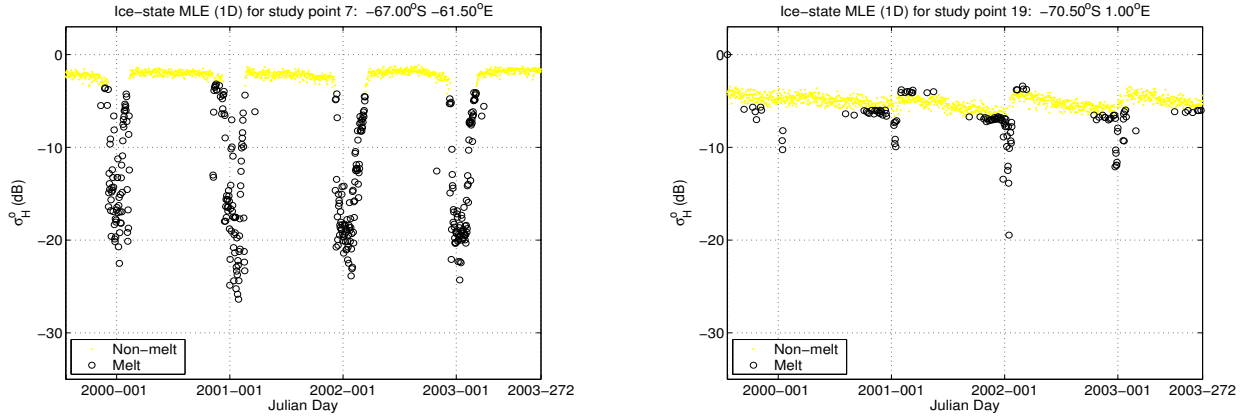
Figure 3.7: Time-series for study points 7 (left) and 19 (right) with resulting ML method surface-melt estimates using only 'h'-pol backscatter.
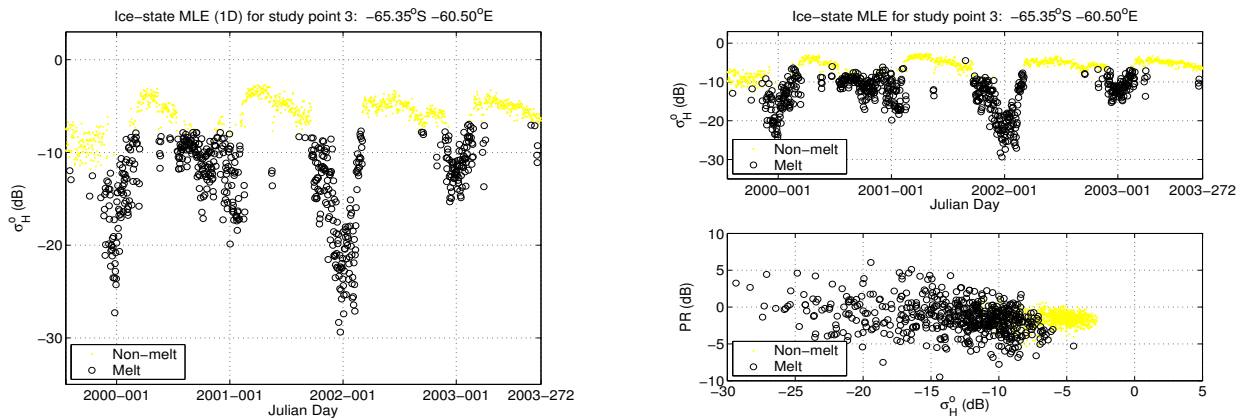
Figure 3.8: Time-series for study point 3 with resulting ML method surface-melt estimates using only 'h'-pol backscatter (left) and dual-polarization backscatter (right).

Figure 3.7 shows the results of the ML method for 'h'-pol only measurements for study point 7 and 19. There are no dramatic changes in the melt classifications from the dual-polarization classifications; however, for point 7 the start of the melt seasons for 2001-2002 and 2002-2003 are later for the 'h'-pol only case (refer to Figure 3.5 for the dual-polarization results). The ML method using horizontal backscatter also marks a premature end to these melt seasons. The melt detection results for study point 19 in Figure 3.7 still contain possibly false melt classifications similar to the dual-polarization case (Figure 3.5), but the number of false melt classifications is noticeably higher for the 'h'-pol only case for each Austral summer except for 2001-2002.

21

The ML melt detection results for study point 3 are shown in Figure 3.8. Note that there are no significant changes between the 'h'-pol only and dual-polarization melt classifications. This indicates that using only one polarization may be adequate in some situations. The main advantage to incorporating the polarization ratio (PR) in the melt detection method is that the melt-season onset and refreeze dates are more precisely identified. This is a result of the change in the variance of the PR values at the onset and end of the melt seasons. During peak melt times and deep winter non-melt periods the PR observations are not as important in determining the presence of surface melt. For these reasons the dual-polarization approach outperforms the 'h'-pol only approach and is adopted as the preferred melt detection method.

3.4 Determining Melt-Onset and Refreeze Dates

Computing the dates of melt-onset and refreeze is important in understanding the inter-annual variability of surface melt in Antarctica. Previous efforts to map these events have focused on Arctic and Antarctic sea-ice. Winebrenner et al. [18] used SAR and scatterometer data to map the melt-onset and refreeze dates of Arctic sea-ice and Drinkwater et al. [5] used scatterometry to map melt-onset of Antarctic sea-ice.

Using the ML method for melt detection on Antarctic ice-shelves we propose the following criteria for determining the melt-onset and refreeze dates. The melt-onset date is chosen to be the beginning of a three-day period of consecutive melt classifications and the refreeze date is selected as the day marking the start of a period of no melt classifications for at least 7 days. Figure 3.9 contains maps of the resulting melt-onset date estimates for each year over the Antarctic peninsula and Figure 3.10 maps the total number of days classified as melt events during each Austral summer for the peninsula. For each pixel in the images the distribution from the nearest study point is used in the ML ice-state classification. Only locations below 100m in elevation are used in the melt-onset progression maps.
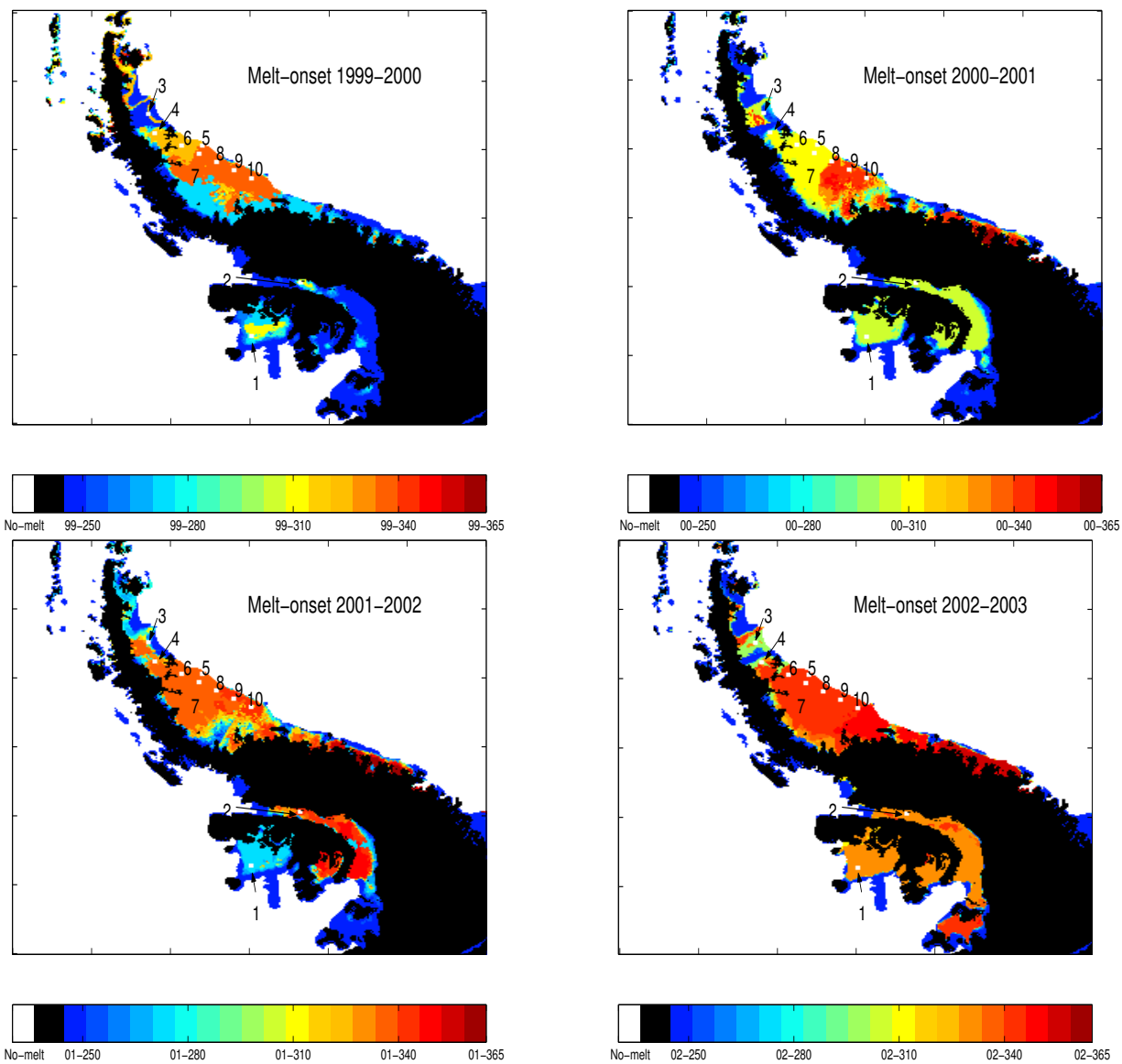
Figure 3.9: Melt-onset dates (yy-ddd) over the Larsen Ice-shelf for each Austral summer from 1999 to 2003. The 10 study points in this region are indicated.
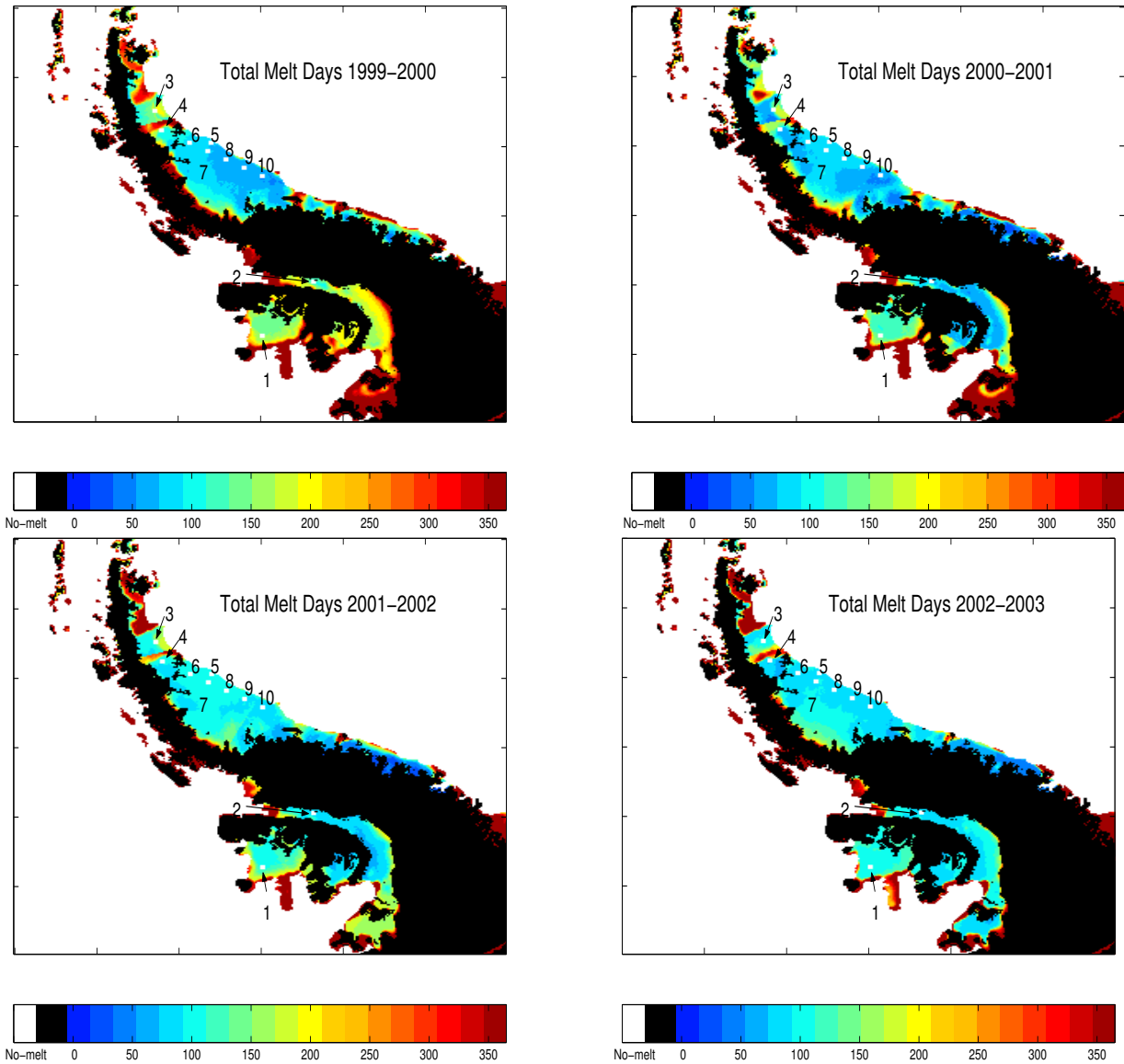
Figure 3.10: Total days classified as melt for the Larsen Ice-shelf during the each Austral summer from 1999 to 2003.

For the discussion of these melt maps we follow the terminology used by Vaughan and Doake [19]: the northernmost section of the Larsen Ice-shelf (just north of study point 3) is termed the Larsen "A", the section covered by points 3 and 4 is the Larsen "B", and points 5-10 span the Larsen "C". Point 1 is located on the Wilkins Ice-shelf and point 2 on the George VI Ice-shelf.

From Figures 3.9 and 3.10 we see that the Larsen A experiences a very early melt onset and over 300 days of melt each year. From 2001 to 2003 nearly every day is classified as melt. This is expected since the Larsen A disintegrated in 1995, thus removing all multi-year ice from the area [6]. The boundary between the Larsen A and Larsen B ice-shelves is marked by an abrupt change in the results from the melt-total and melt-onset maps for each year. The Larsen B melt season begins much later and ends earlier than for the Larsen A.

The Larsen C experiences significant melt much later than the Larsen A and B for the 1999-00, 2000-01, and 2002-03 melt seasons. The total number of melt days for each pixel of the Larsen C is almost uniform, but for 2000-01 the southern portion of the shelf begins its melt season more than a month later than the northern part. The maps also show that even though the Larsen C melt season occurs later for 2001-02 and 2002-03 than previous summers, the total number of melt days is very similar for each year.

The Wilkins and George VI Ice-shelves show considerable variation in their respective dates of melt-onset from year to year. The 1999-00 melt season begins earlier on the edges of both shelves than in the interior. This year also experiences a longer melt season duration than the other years. The 2000-01 Austral summer is marked by a later melt-onset than the previous year and the melt is uniform over the entire surface of each shelf. During the 2001-02 and 2002-03 melt seasons the total melt on each shelf is very uniform ($\sim$100-150 melt days) but the Wilkins shelf begins its melt season nearly 3 months earlier than the George VI shelf for 2001-02.

The ML method melt-onset and melt season duration results are realistic. The method consistently classifies melt over contiguous areas and some interesting features are observed in the variations of the melt seasons from year to year. In order to determine the validity of this melt detection method an analysis of passive microwave measurements were analyzed using previous methods and the results are given in the next section.

3.5 Validation Using Radiometer Data

Passive microwave brightness temperature measurements have previously been used to detect melt on Arctic sea-ice and the Greenland ice-sheet from SSM/I observations. The results from three melt detection methods using this data are compared to the ML method classifications using QuikSCAT data.

Anderson [4] used the horizontal range,

$$HR = T_b(19H) - T_b(37H), \tag{3.6}$$

to determine melting events on Arctic sea-ice. $T_b(19H)$ is the 'h'-pol 19 GHz channel value and $T_b(37H)$ is the 'h'-pol 37 GHz channel value for a given location. If HR drops below $2K$ a melt event is counted. Although this method has previously only been applied to Arctic sea-ice, here we use this algorithm with the brightness temperatures of Antarctic shelf-ice.

Abdalati and Steffen [13] used the cross-gradient polarization ratio (XPGR) to detect melt over Greenland. This method uses

$$XPGR = \frac{T_b(19H) - T_b(37V)}{T_b(19H) + T_b(37V)} > -0.0158 \tag{3.7}$$

to classify melt. Similar to the HR method, XPGR attempts to take advantage of the sensitivities of the different frequency channels to the changing water content in the snow cover. XPGR also uses both polarizations to further accentuate the differences in the observation responses.

A method for determining melt on the Greenland ice-sheet proposed by Ashcraft and Long [14] is implemented using SSM/I data. This method, hereafter T_b-α, uses a threshold set between the mean winter brightness temperature value (T_b^{dry}) and the brightness temperature for wet snow (T_b^{wet}). Melt is classified for

$$T_b > \alpha T_b^{dry} + (1 - \alpha)T_b^{wet} \tag{3.8}$$

where $T_b^{wet} = 273K$, $\alpha = 0.46$, and T_b is the 'v'-pol 19 GHz channel value [14].

The lower portions of Figures 3.11 and 3.12 show the time-series of available SSM/I data corresponding to the QuikSCAT dataset for four locations. Note that whenever the backscatter decreases significantly there is usually an accompanying rise in brightness temperature measurements. The data for point 3 in Figure 3.11 reveals a deviation from this

26

pattern. The drop in backscatter during the 2001-2002 Austral summer corresponds to varying responses in the T_b values for each SSM/I channel. Since passive microwave observations are more subject to changing atmospheric conditions, the discrepancy between the two sensors at this location may be due to atmospheric effects. The variation in responses between the SSM/I channels are due to the different operating frequencies and polarizations. Higher-frequency channels are effected more by interference from the atmosphere.
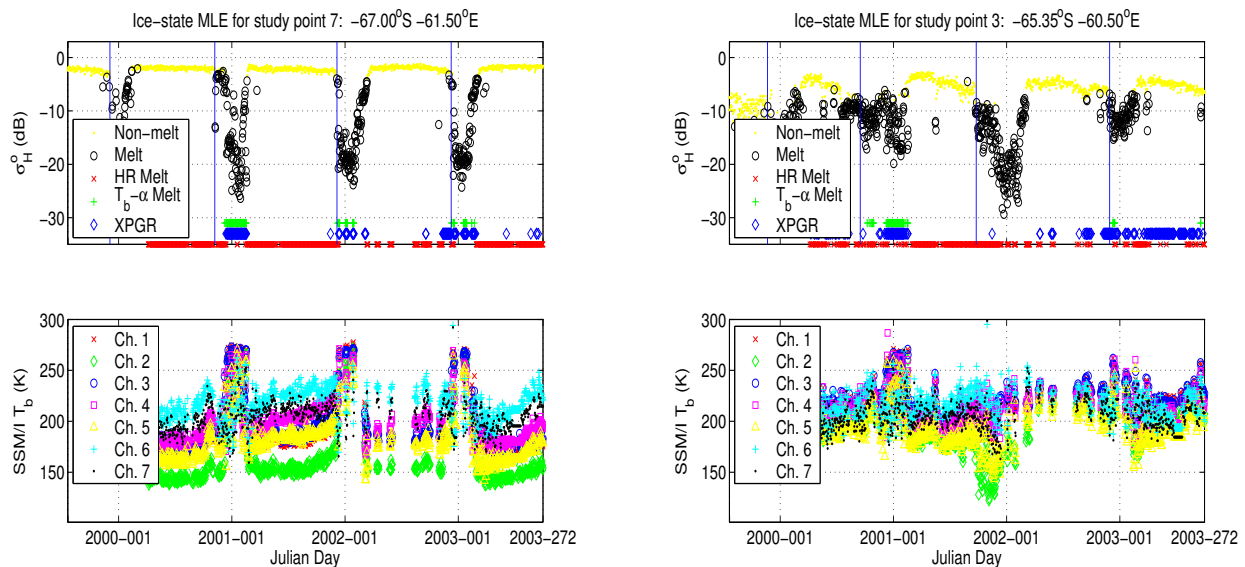

Figure 3.11: Results from the ML method (top row) and the methods using SSM/I data (bottom row) for points 7 (left column) and 3 (right column). Vertical lines mark the melt-onset dates from the ML method. ML, T_b-α, and XPGR melt classifications are consistent for point 7 but differ for point 3 where T_b-α and XPGR miss the melt season of 01-02 and diverge for 02-03. The HR method detects melt nearly every day and almost no melt during melt-periods detected by the other methods.

The results of the HR, XPGR, and T_b-α melt algorithms are shown in the upper portions of these figures along the bottom of each time-series. The HR method classifies nearly every day as melt for each of the 25 study points while the ML, XPGR, and T_b-α results are more consistent. This indicates that the HR method is not portable for use in melt detection outside of the Arctic region. The ML method generally results in more days
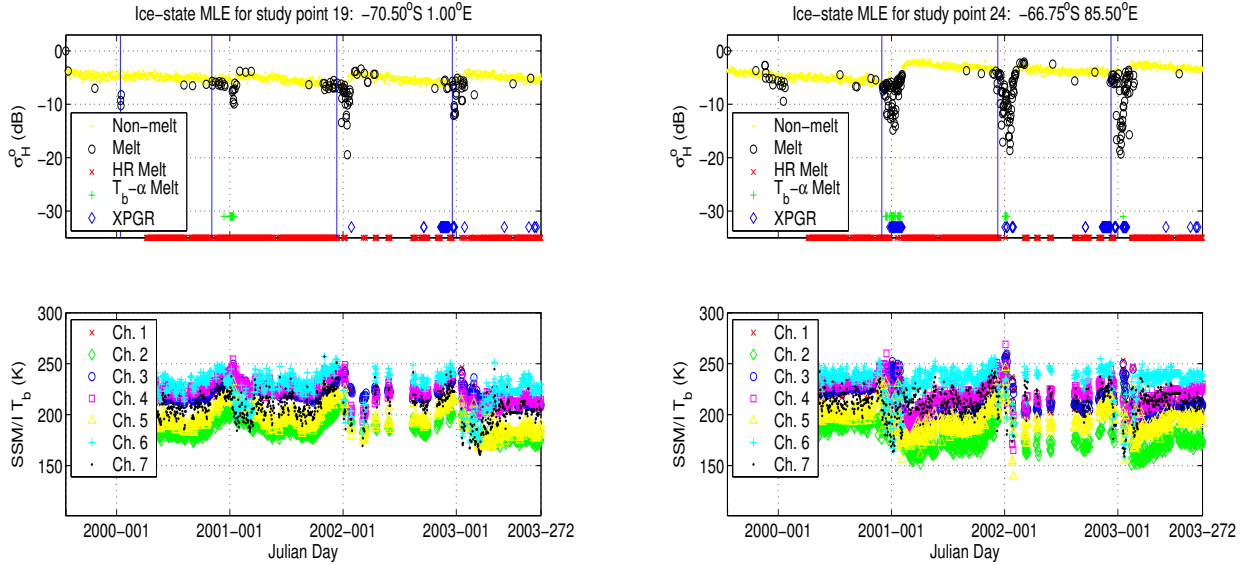
Figure 3.12: Results for points 19 (left) and 24 (right). The ML method shows an earlier end to the 2000-2001 melt season than Ashcraft's method for point 19.

classified as melt than the T_b-α method. XPGR results vary much more from year to year than the other methods as illustrated by the classifications for point 3 (Figure 3.11).

The ML method appears to be more sensitive to melt conditions in some cases than the methods using passive microwave data. This is evident in the results for study point 3 in Figure 3.11. The T_b-α method does not distinguish any melt events during the 2001-02 summer; however, the backscatter time-series clearly indicates substantial melting and the ML method appropriately identifies many days of surface melt. XPGR sporadically identifies a few days as melt during this period and overestimates the number of melt events for the 2002-03 summer and winter of 2003.

The total number of melt days and the melt-onset dates from the ML method for the 25 study points during each year of the study are given in Table 3.2. The melt-onset dates calculated by the ML algorithm are usually a few days prior to the first day of melt detected by XPGR and T_b-α. This is the case for the melt season of 2000-01 for point 7, and for 2000-01 and 2001-02 for points 19 and 24. The XPGR method detects melt prior to the ML method for point 7 during 2001-02 and 2002-03 and for points 3, 19, and 24 during 2002-03. Melt-onset dates from the ML and T_b-α results are very close during 2001-02 and

28

2002-03 for point 7, during 2000-01 and 2002-03 for point 3, and during 2000-01 for point 24. For most of the study points it is observed that when each of the ML, XPGR, and T_b-α methods detect melt during a given melt season the melt-onset dates for the ML and T_b-α methods are within a few days while the XPGR dates vary considerably.

Table 3.2: Melt-onset dates and total number of melt days for the 25 study points for each year from the ML QuikSCAT melt detection method. See Table 3.1 for the latitude and longitude of each study point.

Point	1999-00 Onset/Total	2000-01 Onset/Total	2001-02 Onset/Total	2002-03 Onset/Total
1	99-279 / 153	00-306 / 131	01-270 / 103	02-332 / 097
2	99-311 / 112	00-307 / 070	01-345 / 082	02-332 / 081
3	99-324 / 149	00-257 / 133	01-266 / 159	02-331 / 096
4	99-322 / 099	00-308 / 059	01-334 / 094	02-299 / 078
5	99-337 / 075	00-309 / 089	01-338 / 099	02-341 / 089
6	99-324 / 083	00-308 / 079	01-334 / 099	02-341 / 084
7	99-337 / 075	00-309 / 087	01-338 / 098	02-341 / 091
8	99-337 / 060	00-341 / 078	01-338 / 097	02-341 / 085
9	99-337 / 054	00-341 / 073	01-343 / 091	02-345 / 087
10	99-337 / 054	00-341 / 056	01-343 / 078	02-345 / 083
11	00-017 / 021	00-334 / 056	01-346 / 055	02-344 / 058
12	—— / 000	—— / 000	—— / 002	02-365 / 026
13	—— / 000	—— / 000	—— / 002	—— / 003
14	—— / 000	—— / 000	—— / 001	—— / 002
15	—— / 001	—— / 001	—— / 001	—— / 000
16	—— / 006	00-362 / 027	01-320 / 018	—— / 016
17	—— / 000	—— / 000	—— / 001	03-019 / 005
18	—— / 000	—— / 000	—— / 001	—— / 000
19	00-011 / 007	00-306 / 028	01-344 / 050	02-351 / 036
20	—— / 001	—— / 002	—— / 001	—— / 000
21	—— / 003	—— / 000	—— / 003	—— / 003
22	—— / 018	—— / 018	02-018 / 032	—— / 026
23	—— / 000	—— / 000	—— / 000	—— / 000
24	—— / 011	00-333 / 062	01-342 / 063	02-342 / 057
25	99-349 / 041	00-329 / 066	01-331 / 078	02-336 / 094

Chapter 4

Calibrating QuikSCAT and SeaWinds Scatterometers

The σ^o measurements collected by scatterometers are used in many remote sensing applications. Inferring geophysical phenomena from this data depends upon the accuracy of the given measurements. Verifying the proper calibration of scatterometer instruments is required to ensure that scatterometer measurements are valid for such applications. The so-called tandem mission, consisting of the SeaWinds on QuikSCAT and SeaWinds on ADEOS-2 instruments, yields high spatial- and temporal-resolution measurements that facilitate observation of the diurnal cycle. Cross-calibration of these instruments is essential in order to maximize the utility of the data. This chapter presents a study to ensure cross-calibration of SeaWinds and QuikSCAT and is organized as follows: Section 1 provides additional background for the problem, Section 2 discusses the sensor specifications, Section 3 describes the calibration method, and Sections 4 and 5 contain calibration verification results for two land target areas followed by a summary of the results.

4.1 Background

The normalized radar backscatter for a given target varies with location, time, azimuth, incidence angle, and polarization. Suitable targets for calibration must have an isotropic radar response (i.e., independent of azimuth and temporally stable) [20]. Backscatter from such targets exhibits only incidence angle dependence.

Long and Skouson [20] showed that tropical rainforests can effectively be used for scatterometer calibration to within a limit of ± 0.15 dB for a relative calibration method designed to ensure intra-sensor antenna consistency. They calculated σ^o bias corrections for the Seasat scatterometer (SASS) and the ERS-1 Active Microwave Instrument in scatterometer

mode (Escat) and found that the Escat (C-band) data is very well calibrated while SASS (Ku-band) data requires significant correction.

Tropical rainforests have traditionally been used to calibrate scatterometers [7, 20, 21, 22]. The Amazon forest covers a large spatially homogenous area and exhibits little seasonal or azimuthal variation. However, some concern has been noted over possible time-of-day effects relating to the diurnal cycle. Similar methods using open-ocean and distributed land targets were applied to data from the NASA scatterometer (NSCAT) mission [23] and the Tropical Rain Measuring Mission (TRMM) [22].

Following Long and Skouson [20], locations in the Amazon and the Sahara with a radar response within ±0.5 dB of a typical σ^o value from the respective region are used in the calibration. For the Amazon, the area considered is the circular region of radius ∼1200km centered at 3°S, 61°W. Appendix B contains analysis of four subregions of the Amazon. The Sahara region is centered at 20°N, 14°E with a radius of ∼700km. These land targets lie in the same latitudinal band and offer different insights into the diurnal cycle. No diurnal variation is expected in the Sahara desert as opposed to the Amazon.

In this chapter a relative cross-calibration analysis is performed on QuikSCAT and SeaWinds scatterometer data. The data from 2003 Julian Day 169 to Julian Day 224 is used and measurements collected by each antenna are corrected for σ^o bias. This correction is made for the Amazon region spatially masked as described by Zec et al. [7], and for a spatially masked region of the Sahara desert in northern Africa. A 3-week window of data starting at 2003 JD 169 is used for the mask. Figure 4.1 shows the masked areas for the Amazon rainforest and the Sahara desert used for calibration. Correction results are presented for each antenna and sensor for each given region. Evidence of the variation in the Amazon's radar response due to polarization and the diurnal cycle is presented.
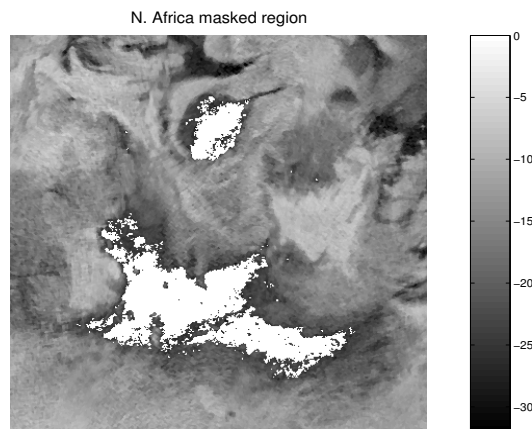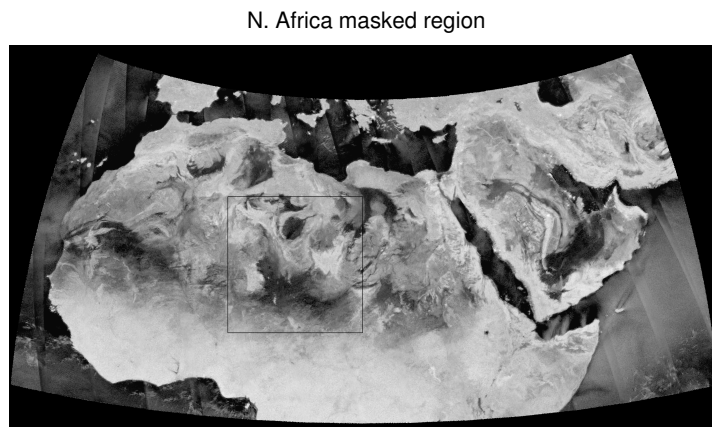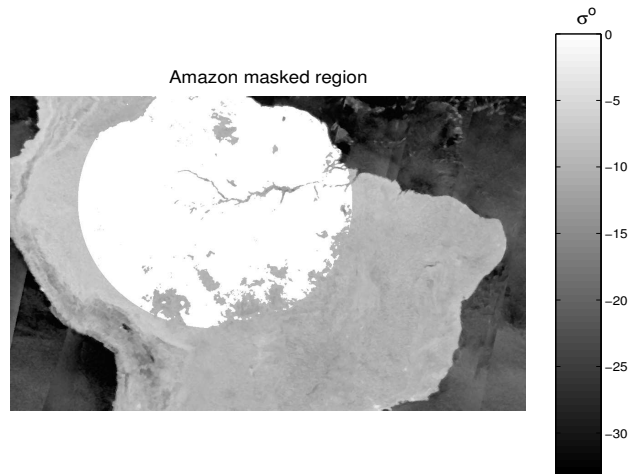
Figure 4.1: Selected calibration regions from the Amazon (top) and the Sahara (bottom). The bottom image is the Sahara masked region and is a close-up of the boxed area in the center image. The white pixels indicate the spatially masked data sets.

4.2 QuikSCAT and SeaWinds Scatterometers

The QuikSCAT and SeaWinds sensors have identical specifications but their respective platforms are in different orbits (see Chapter 2). The SeaWinds instrument trails QuikSCAT along its orbital path and crosses the equator on ascending and descending passes approximately 6 hours after QuikSCAT. The QuikSCAT spacecraft is geodetic pointing while ADEOS-2 is geocentric. This results in a larger standard deviation in incidence angle for SeaWinds than QuikSCAT (Figure 4.2).
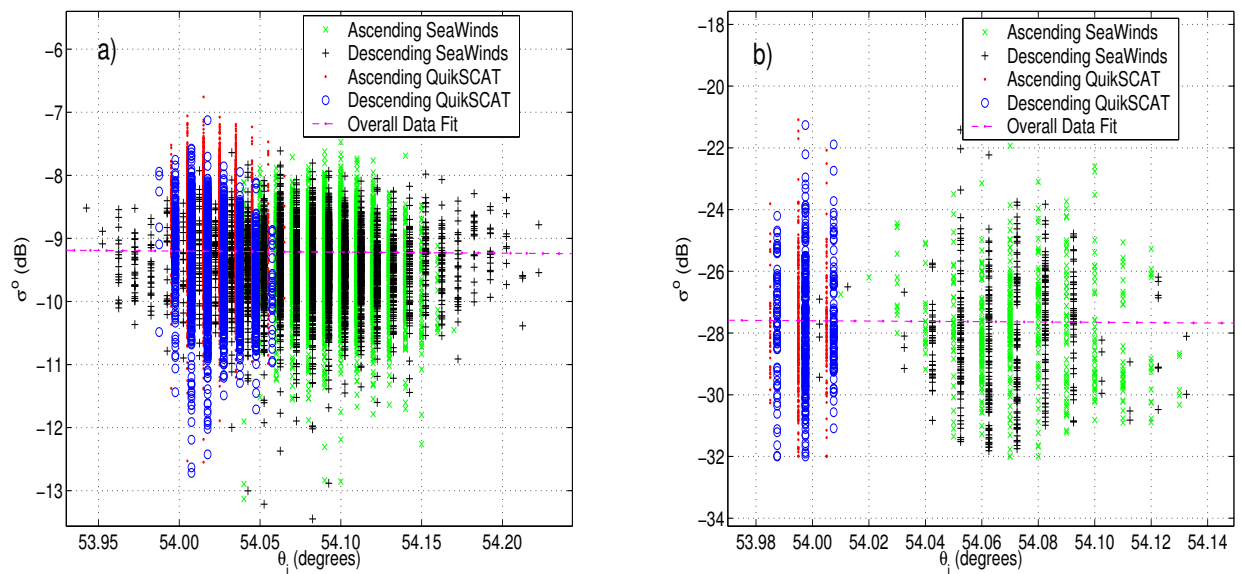
Figure 4.2: Plots of θ_i vs. A for uncorrected 'v'-pol "egg" SIR-image data from the Amazon (a) and the Sahara (b) masked regions. Note the larger variation in incidence angle for SeaWinds than for QuikSCAT. Over the Amazon the standard deviations of θ_i are 0.0129, 0.0130, 0.0213, and 0.0341 degrees for the ascending and descending passes of QuikSCAT and SeaWinds, respectively.

Figure 4.3 shows a histogram of the time-of-day associated with each backscatter measurement made by both sensors during ascending and descending passes over a 4-day period from 2003 JD 139 to 142. The orbit paths for the two satellites repeat every four days. The ascending passes of QuikSCAT typically observe the Amazon region from 6-7 am local time while its descending passes occur from 6-7 pm. The ascending and descending passes of

SeaWinds cross over the Amazon from 10-11 am and 10-11 pm local time, respectively. This temporal sampling over the rainforest is key in observing diurnal variation of the backscatter.
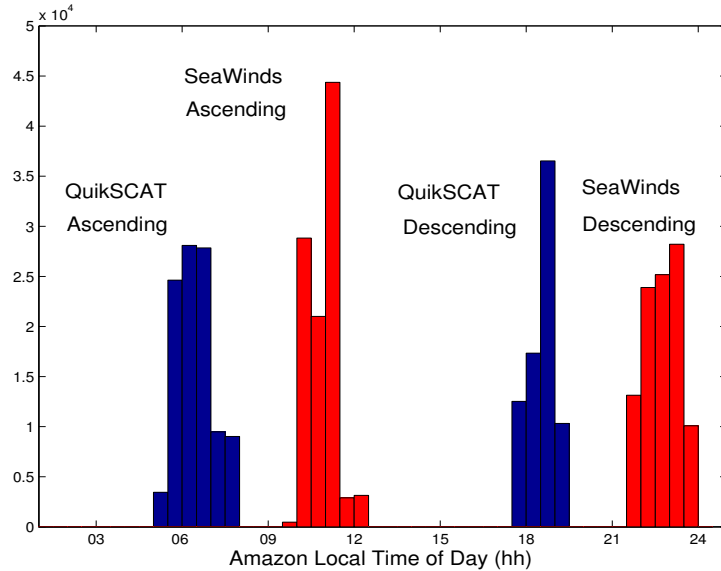

Figure 4.3: Histogram of local times of day for backscatter measurements from all passes of both sensors during a 4-day orbit cycle over the Amazon rainforest.

Previous calibration and verification methods been based on raw σ^o measurements. However, we use measurements processed via the Scatterometer Image Reconstruction (SIR) algorithm [15]. Using the algorithm we combine measurements from respective ascending and descending passes for each sensor during a 4-day span to create data images for the Amazon and northern Africa. These 4-day composite images offer complete coverage of these regions and increased spatial resolution. Some temporal resolution is sacrificed since overlapping measurements contained in sequential images are averaged; however, distinct differences are still present in the backscatter collected by QuikSCAT and SeaWinds from different times of day.

35

The calibration method presented in this paper is applied to SIR-format images of the respective ascending and descending passes of QuikSCAT and SeaWinds. SIR image products have a resolution of 2.25 km/pixel for "slice" images and 8.9 km/pixel for "egg" images. Slice and egg images are used separately in the calibration verification but only results from the slice corrections are shown since there is no significant difference in the results from the egg analysis.

4.3 Calibration Method Description

The p-order polynomial incidence angle response model developed in [20] was used by Zec, Long, and Jones [7] for the calibration of the NASA Scatterometer (NSCAT), which also operated in Ku-band. The results from the NSCAT calibration yielded negligible higher-order polynomial coefficients; therefore, a simple first-order polynomial model is used for calibration of QuikSCAT and SeaWinds, since they have only narrow incidence angle ranges.

The standard model for the incidence angle dependence of σ^o is

$$\sigma^o_{bi} = A + B(\bar{\Theta}_b - \theta_{bi}) \tag{4.1}$$

where i is the pixel index in the SIR image for antenna beam b, A is the uncorrected backscatter value, B is the linear dependence on incidence angle, $\bar{\Theta}_b$ is the nominal incidence angle for each beam (54° for 'v'-pol and 46° for 'h'-pol), θ_{bi} is the measurement incidence angle, and σ^o_{bi} is the incidence-angle corrected backscatter value.

The incidence angle dependence coefficient B is calculated as the slope of the linear least-squares fit to the combined data from all passes from both instruments over the reference region. Figure 4.2 illustrates the incidence angle dependence of the backscatter measurements and Table 4.1 provides the calculated B values. These values show that the Sahara desert has a much stronger incidence-angle dependence than the Amazon.

The backscatter in the Amazon rainforest consists of volume scattering, rough-surface scattering, and specular scattering. Since QuikSCAT and SeaWinds measure backscatter at a large incidence angle, the data recorded by these scatterometers exhibits some incidence-angle dependence due mostly to volume scattering. The Sahara desert is characterized by specular scattering and some rough-surface scattering. At large incidence angles the

Table 4.1: The incidence angle dependence coefficients (B in dB/degree) for each region's respective polarization and resolution calculated from all passes of both sensors. 'h'-pol measurements are normalized to an incidence angle of 46° and 'v'-pol to 54°.

Polarization	Resolution	Amazon	Sahara
horizontal	slice	0.1688	0.5842
	egg	0.1678	0.5726
vertical	slice	0.1725	0.5208
	egg	0.1704	0.5111

backscatter dependence on incidence angle is very strong since volume scattering is not present to lessen the effect of specular scattering.

Satake and Hanado [22] also observed this difference in incidence-angle dependence between rainforests and deserts. They used backscatter measurements from the Tropical Rainfall Measuring Mission (TRMM) scatterometer to analyze the incidence-angle dependence of σ^o over small regions in the Amazon rainforest and the Libyan desert. These regions fall within the Amazon and Sahara regions described in the background section of this chapter. TRMM operates in Ku-band and scans incidence angles between 0° and 17°. Satake and Hanado show that dry sand areas exhibit strong incidence-angle dependence due to specular scattering, while the Amazon shows less dependence except at near-nadir incidence angles. Table 4.1 indicates that the difference in the incidence-angle dependence between polarizations for QuikSCAT and SeaWinds is also more pronounced over the desert.

4.4 Cross-calibration Analysis Results for Amazon

The incidence angle correction calculated using the selected regions yield results strongly dependent upon the radar response of the given subregion. For the Amazon, the ascending passes of QuikSCAT observe significantly higher backscatter values than the descending passes and both passes of SeaWinds. The ascending passes of QuikSCAT measure the Amazon's radar response in the early morning hours (see Figure 4.3) when dew is present on the rainforest foliage.

This is consistent with observations of the Amazon made by Satake and Hanado [22]. They observed a difference in σ^o of $\sim$0.5 dB between the maximum backscatter from 6-7 am local time and the minimum backscatter from 6-7 pm local time. The ascending passes of QuikSCAT occur during the morning period of maximum backscatter and we observe a difference of $\sim$0.6 dB between this time and the other observations throughout the day. The increased temporal resolution provided by the combined data from QuikSCAT and SeaWinds allows the conclusion to be draw that this bias is due to the diurnal cycle.

The σ^o incidence angle correction calculated for the masked Amazon region reduces this bias due to diurnal variation from $\sim$0.6 dB to $\sim$0.2 dB (see Figure 4.4). The daily standard deviation of the corrected σ^o values is also reduced considerably. A bias also exists between polarizations with the 'h'-pol values roughly 1.5 dB higher than the 'v'-pol measurements. The daily standard deviation for the ascending passes of QuikSCAT is also noticeably higher than for the other passes of QuikSCAT and SeaWinds (see Table 4.2).
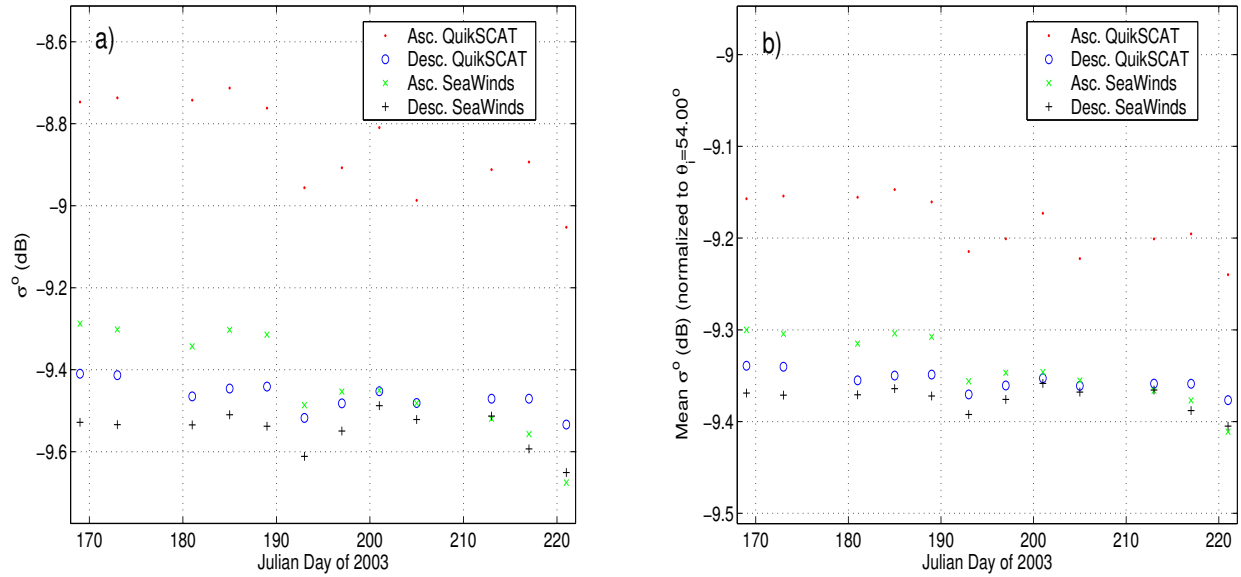
Figure 4.4: Mean daily uncorrected (a) and corrected (b) 'v'-pol slice backscatter time-series for 2003 JD 169-221 in the masked Amazon region. Note the bias due to the diurnal cycle between the ascending QuikSCAT values and the other measurements in both plots. The bias decreases for the corrected values.
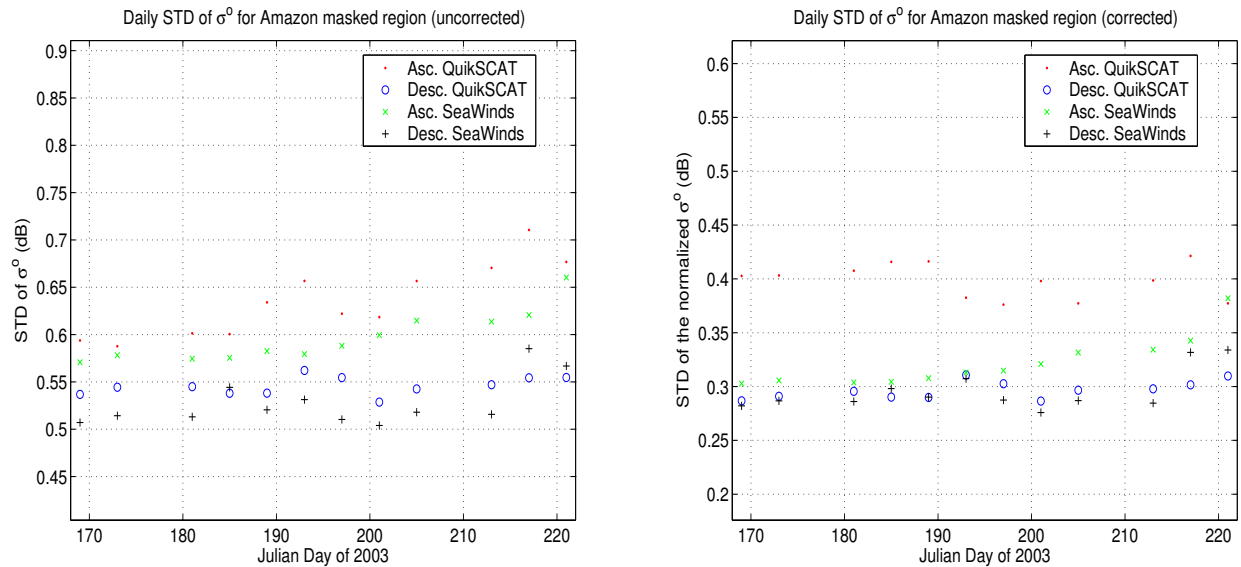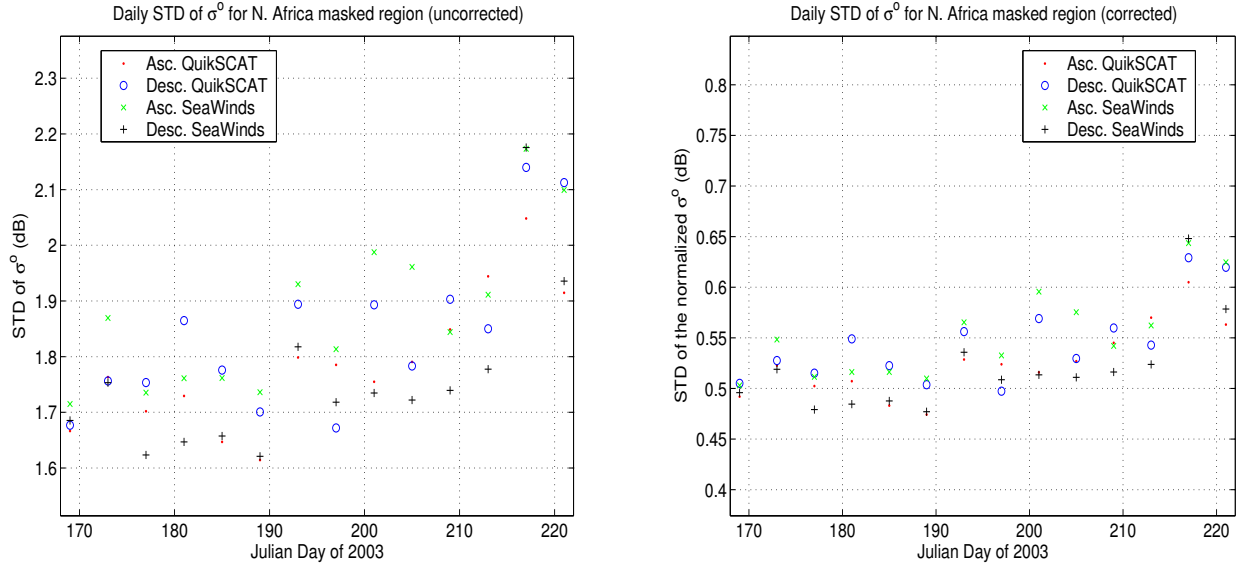

Figure 4.5: Time-series of standard deviation of uncorrected (left) and corrected (right) 'v'-pol slice backscatter for 2003 JD 169-221 in the masked Amazon region.

4.5 Cross-calibration Analysis Results for Sahara

The masked Sahara region is expected to be temporally stable over the study period. No daily moisture variation is observed in the QuikSCAT/SeaWinds measurements. Figure 4.6a reveals that σ^o measurements for this region are much noisier than for the Amazon. This is expected since the power of the desert surface backscatter is roughly two orders of magnitude lower than for the vegetation of the rainforest so the signal-to-noise ratio (SNR) is lower. The daily standard deviation of the incidence-angle corrected σ^o values is reduced considerably (see Table 4.2) and there is no bias due to the diurnal cycle (see Figure 4.6).
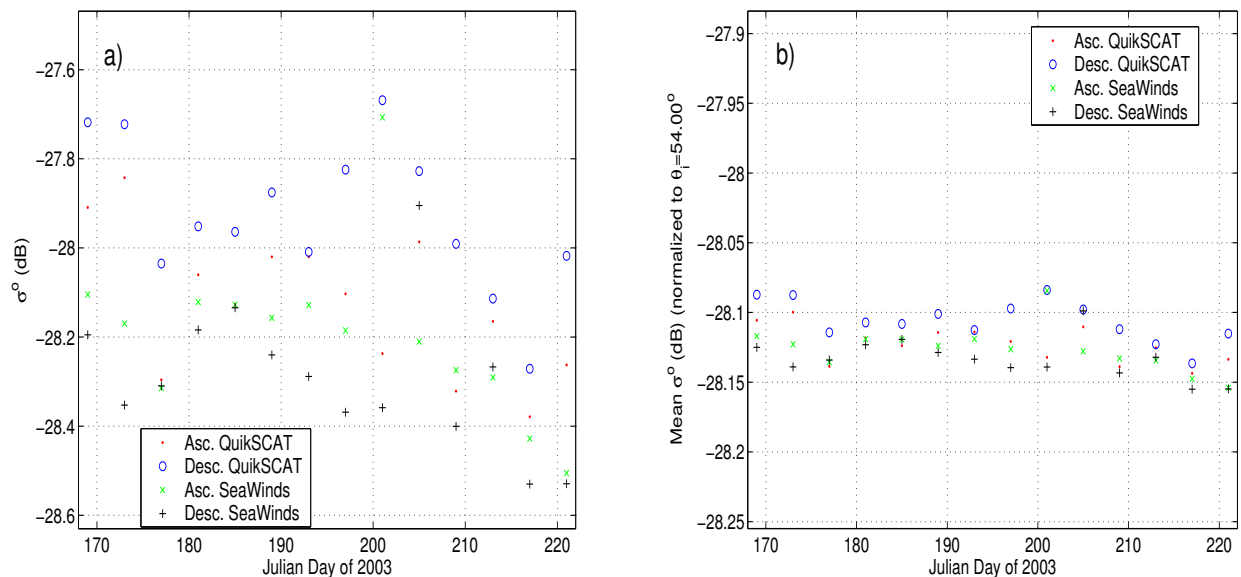
Figure 4.6: Mean daily uncorrected (a) and corrected (b) 'v'-pol slice backscatter time-series for 2003 JD 169-221 in the masked Sahara region. Note the absence of diurnal variation in the measurements in both (a) and (b), though both QuikSCAT passes are generally higher than the SeaWinds values.

The incidence-angle corrected 'v'-pol slice backscatter values for the Sahara region illustrate that the two sensors are in fact very well calibrated. The measurements for all passes of both sensors are within 0.05 dB agreement. This is quite remarkable considering the extremely low return power received by the scatterometers. The corrected 'v'-pol slice backscatter values for the Amazon region do not agree as precisely as for the Sahara

Figure 4.7: Time-series of standard deviation of uncorrected (left) and corrected (right) 'v'-pol slice backscatter for 2003 JD 169-221 in the masked Sahara region.

since moisture in the vegetation of the rainforest is more variable throughout each day and maximum during the morning passes of QuikSCAT.

According to the correction results provided in Table 4.2, the incidence-angle correction method applied to the QuikSCAT and SeaWinds data decreases the standard deviation of the daily mean σ^o values for all passes of both sensors by roughly 70% for the Amazon rainforest and 90% for the Sahara desert. The nominal daily standard deviation of the backscatter for all observations is reduced by about 40% for the Amazon and 70% for the Sahara. The corrected values for both regions indicate that for these spatially homogenous areas the standard deviation of the measurements for each sensor is ~ 0.3 dB for the Amazon and ~ 0.5 dB for the Sahara. For the time-series analyzed it is also shown that these regions are temporally stable since the daily mean backscatter value has a standard deviation of less than 0.05 dB for both regions.

Table 4.2: The correction results for each region. For brevity only the 'v'-pol slice values are presented. Results from 'h'-pol and egg resolution images are similar. The standard deviation of the daily mean σ^o ($SD\{\mu\}$) and the mean of the daily standard deviation of σ^o (μ_{SD}) are given for both uncorrected and incidence-angle corrected values. These values are computed in log space. QuikScat is denoted as QS and SeaWinds as SW.

Sensor	Pass	corrected / uncorrected	Amazon $SD\{\mu\}$	Amazon μ_{SD}	Sahara $SD\{\mu\}$	Sahara μ_{SD}
QS	ascending	uncorrected	0.114	0.636	0.161	1.786
		corrected	0.031	0.398	0.013	0.526
	descending	uncorrected	0.037	0.546	0.167	1.841
		corrected	0.011	0.297	0.015	0.545
SW	ascending	uncorrected	0.122	0.596	0.185	1.878
		corrected	0.035	0.322	0.016	0.553
	descending	uncorrected	0.047	0.528	0.161	1.758
		corrected	0.013	0.296	0.015	0.520

Chapter 5

Conclusions

Observing the inter-annual variation of melt seasons for Antarctic ice-shelves is important for long term global climate studies. Microwave scatterometers provide high temporal and spatial resolution measurements of this region and are less susceptible to atmospheric interference than their passive microwave counterparts. This is a great advantage in determining the surface characteristics of Antarctic ice-shelves since much of this region is storm-ridden for most of the year.

The new maximum likelihood (ML) melt-detection algorithm using QuikScat dual-polarization measurements is a promising method for detecting surface melt. The melt-onset date estimates correspond to the beginning of periods with greatly reduced backscatter. Melt classifications using this method are spatially consistent. Maps of the melt-onset progression and melt season duration are created for each Austral summer from 1999 to 2003. The maps for the Larsen Ice-shelf indicate increased melt for recently disintegrated portions of the shelf.

Validation of the ML method is performed using passive microwave methods previously used to detect melt on Arctic sea-ice and the Greenland ice-sheet. Comparing these methods reveals that using QuikScat measurements is very effective in determining the presence of surface melt on Antarctic ice-shelves and that the ML method melt-onset dates and melt season duration estimates are reliable and consistent. Additionally, the backscatter observed by QuikScat is at a much finer spatial resolution than the radiometer T_b measurements. This allows for more precise observation of spatially-varying surface melt. The study points analyzed for melt detection are of particular interest to scientists monitoring the

43

health of the ice-shelves and were suggested through personal correspondence by Ted Scambos of the National Snow and Ice Data Center at the University of Colorado in Boulder.

A simple calibration method is also applied to verify the relative accuracy of the radar backscatter measurements from the QuikScat and SeaWinds scatterometers. A first-order polynomial model of σ^o is used to adjust the measurement biases due to incidence-angle dependence of the backscatter. This method is applied to spatially masked regions of the Amazon rain forest and the Sahara desert. The backscatter measurements from the ascending and descending passes of the scatterometers show that the Amazon rain forest exhibits diurnal variation in the radar response. Results from the σ^o incidence-angle corrections for the Sahara desert reveal that the QuikSCAT and SeaWinds instruments are calibrated to within $\sim$0.05 dB.

5.1   Contributions

This thesis extends the application of scatterometers to detection of surface melt on Antarctic ice-shelves and shows that these instruments provide insight into spatially varying characteristics of the shelf-ice.

- I observed melt signatures of snow-covered ice in the time-series of QuikSCAT σ^o data.

- I experimented with several melt detection algorithms using backscatter from the ERS-1/2 and QuikSCAT missions and developed the maximum likelihood method used in this thesis. This method can be further developed, but the results show that the method is useful in detecting surface melt.

- I mapped the progression of melt-onset for the Antarctic peninsula and provided a record of the melt classifications for important study regions for the QuikSCAT scatterometer mission. This record will aid researchers monitoring the conditions of the ice-shelves and is important in understanding the behavior of the ice-shelves preceding iceberg calving and shelf breakup.

- I compared these ML melt detection results with melt classifications using passive microwave SSM/I data.

This work also verifies the proper cross-calibration of the QuikSCAT and SeaWinds scatterometers. The calibration analysis demonstrates the use of this tandem mission data to observe temporal variations in the radar response of a given area.

- I investigated the presumed diurnal variation in the Amazon rainforest by observing data from QuikSCAT and SeaWinds over the Amazon and the Sahara desert. I presented evidence of the diurnal cycle in the Amazon.

- I applied a standard incidence-angle correction to backscatter recorded by QuikSCAT and SeaWinds and showed that the two scatterometers are well-calibrated (within ~0.05 dB) and their measurements need no calibration corrections.

5.2   Future Research

Additional work with the ML melt detection method includes determining the proper spatial sampling of ice-shelf study points in order to obtain valid melt classifications for all ice-shelves. Applying the ML method to determine melt events on the Greenland ice-sheet is also possible. This facilitates the comparison of melt detection results from other active and passive microwave methods, since research in this area is more developed for the Greenland region. The principles of the ML method may also be applied to data from other scatterometers, such as ERS-1/2, NSCAT, and SASS.

Daily SIR images of the Antarctic ice-shelves are currently used in the ML method. Adjusting the method to detect melting and freezing within one day is possible by using raw data values from individual satellite passes. This may provide added insight into the stability of the ice-shelves. Scientific interpretation of the ML melt classification results is also necessary in order to ascertain the health and stability of the Antarctic ice-shelves.

APPENDIX

Appendix A

Additional Melt Detection Results

For completeness, this appendix documents the results obtained for all 25 study points in the melt detection analysis from Chapter 3. Each study point is considered with two pages of figures accompanying every point. The format for the figures is described first. The figure on the first page for each point contains four different plots. Most of these figures contain numerical matrices below the caption.

The upper left quadrant provides the data time-series for both PR and σ_H^o from 1999 Julian Day 250 to 2003 Julian Day 272. As discussed in Chapter 3, these plots denote alternating periods of melt and non-melt seasons for which the mean PR and σ_H^o values are found as well as the covariance. The covariance matrices and mean vectors for each season are given below the figure for study points located on the Antarctic peninsula (points 1-10). R_0 and R_1 are the covariance matrices empirically computed for the non-melt and melt seasons, respectively, and m_0 and m_1 are the mean vectors during the same periods. Some locations elsewhere experience very little melt and the respective melt-season covariance from a nearby point is used in the daily ice-state estimations. This is noted in the discussion of results associated with such study points.

The upper right quadrant contains four scatterplots of σ_H^o vs. PR, one for each year of the study. The ML method results are shown in these plots as red x's for melt classifications and blue dots for non-melt values. The decision boundaries are also shown. For most points this boundary is an ellipse; however, for some points where very few melt events occur the boundary is a hyperbola. The decision boundary is computed from the likelihood ratio function discussed in Chapter 3.

The first page for each point also contains plots that illustrate the distributions for all backscatter values within neighborhoods of radii 1 and 15 pixels (2.25 km and 34 km) from each study point. The melt-season distributions are represented by x's for the mean backscatter values with ellipses at 1 standard deviation from the mean. The non-melt distributions are similarly shown with dots for the mean values and ellipses at the 1-σ contour. Most study points exhibit very little variation between the distributions for the different neighborhood sizes. Points 3, 4, and 24 vary more than the other points since these locations are on ice/ocean boundaries and points 3 and 4 are on the northern portion of the Larsen Ice-shelf which undergoes considerable melting each year.

The second page for each study point contains one figure with two plots. The upper plot shows the σ_H^o time-series with the ML ice-state estimation results. Melt events are shown as black circles while non-melt values are yellow dots. Along the bottom of the time-series are results from melt detection methods using SSM/I data. The lower plot contains the T_b time-series for each of the seven channels for the SSM/I instruments.

QuikSCAT time–series for study point 1: –70.25°S –73.50°E
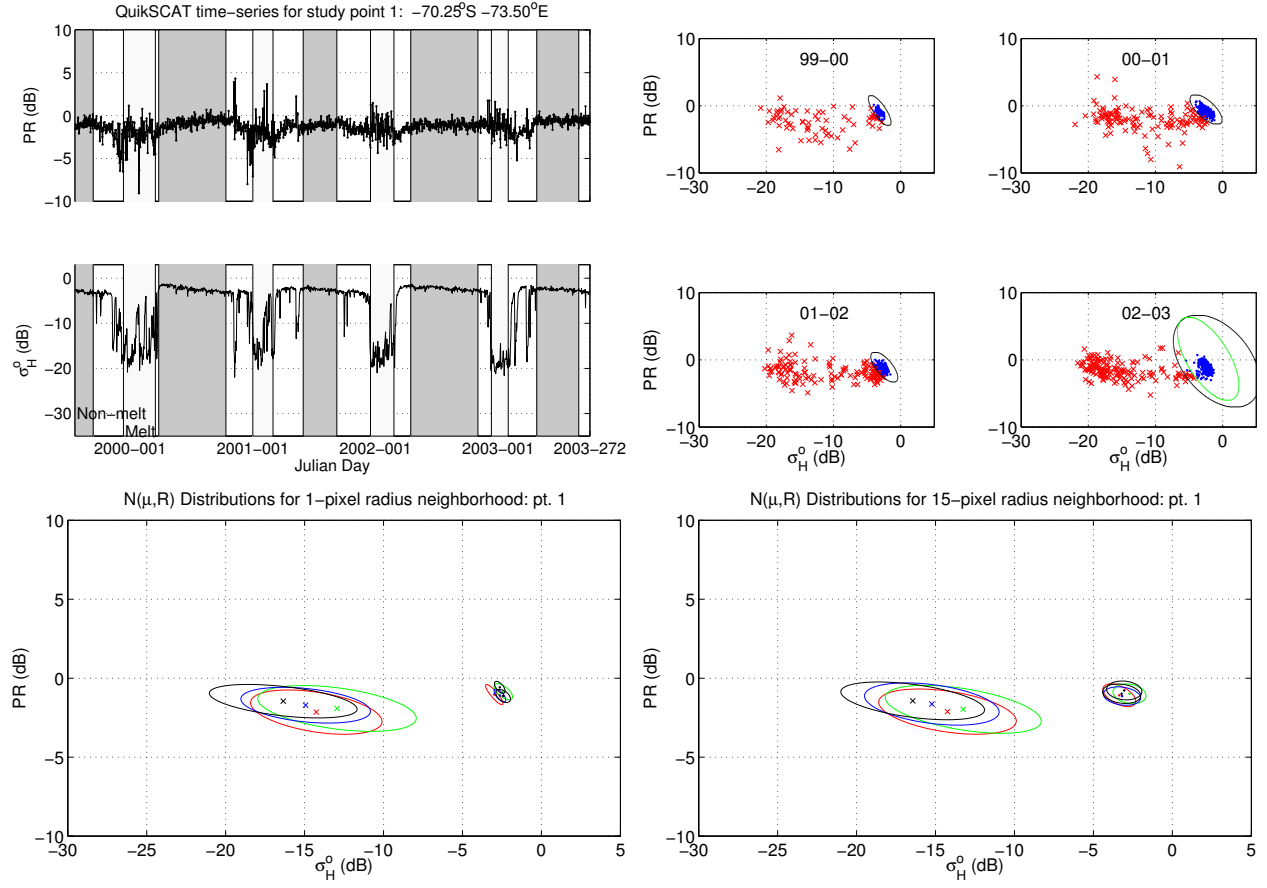
Figure A.1: ML melt detection results for study point 1.

	1999	2000	2001	2002

$$\mathbf{R_0} = \begin{bmatrix} 0.12 & -0.13 \\ -0.13 & 0.22 \end{bmatrix} \quad \begin{bmatrix} 0.38 & -0.23 \\ -0.23 & 0.31 \end{bmatrix} \quad \begin{bmatrix} 0.12 & -0.08 \\ -0.08 & 0.14 \end{bmatrix} \quad \begin{bmatrix} 0.16 & -0.07 \\ -0.07 & 0.17 \end{bmatrix}$$

$$\mathbf{R_1} = \begin{bmatrix} 17.02 & -2.63 \\ -2.63 & 2.15 \end{bmatrix} \quad \begin{bmatrix} 25.46 & -3.32 \\ -3.32 & 2.63 \end{bmatrix} \quad \begin{bmatrix} 8.87 & -1.21 \\ -1.21 & 1.59 \end{bmatrix} \quad \begin{bmatrix} 2.12 & -1.03 \\ -1.03 & 1.32 \end{bmatrix}$$

$$\mathbf{m_0} = \begin{bmatrix} -3.00 \\ -0.98 \end{bmatrix} \quad \begin{bmatrix} -2.39 \\ -0.80 \end{bmatrix} \quad \begin{bmatrix} -2.50 \\ -1.14 \end{bmatrix} \quad \begin{bmatrix} -2.30 \\ -1.13 \end{bmatrix}$$

$$\mathbf{m_1} = \begin{bmatrix} -14.40 \\ -2.13 \end{bmatrix} \quad \begin{bmatrix} -12.77 \\ -1.95 \end{bmatrix} \quad \begin{bmatrix} -16.15 \\ -1.49 \end{bmatrix} \quad \begin{bmatrix} -18.71 \\ -1.14 \end{bmatrix}$$
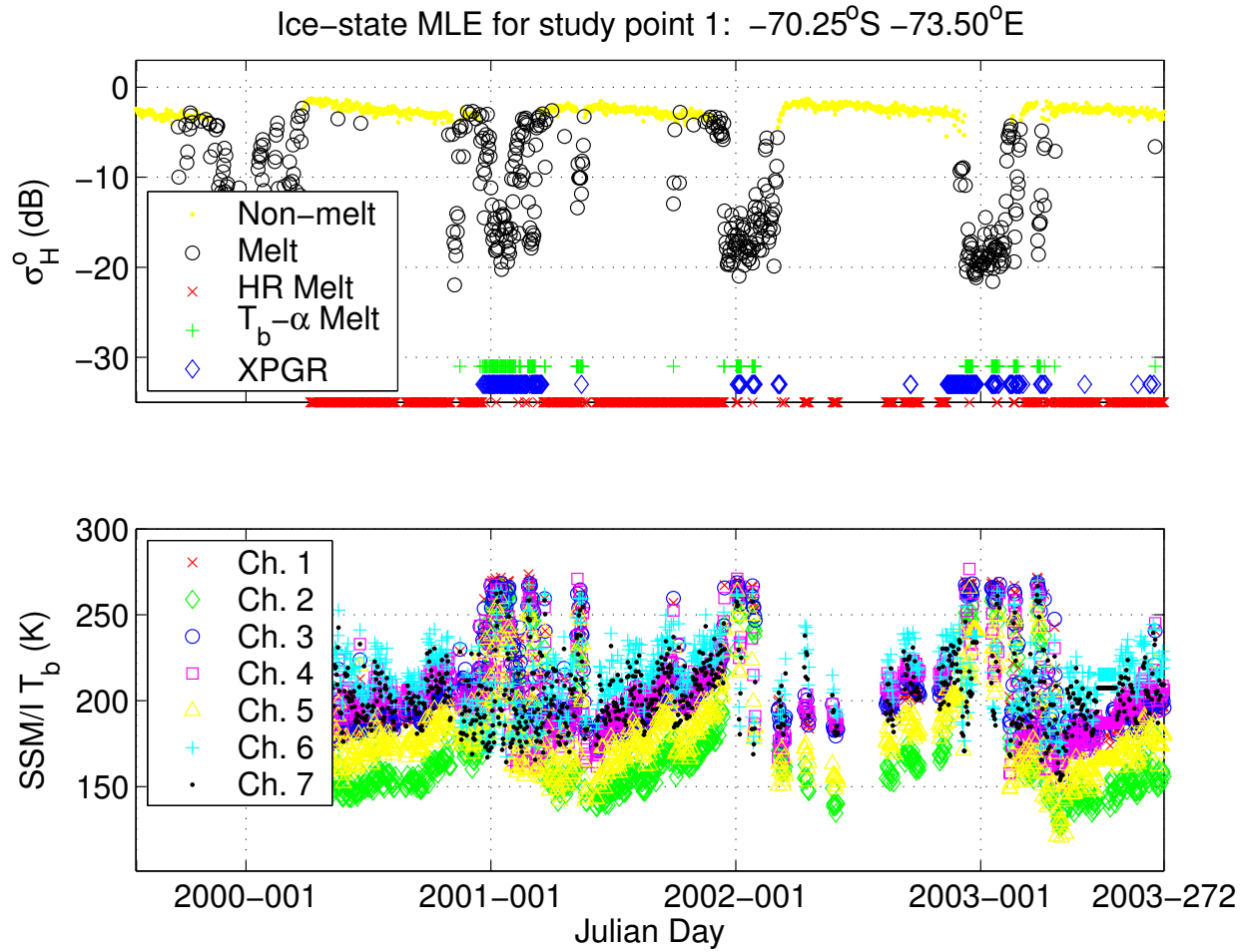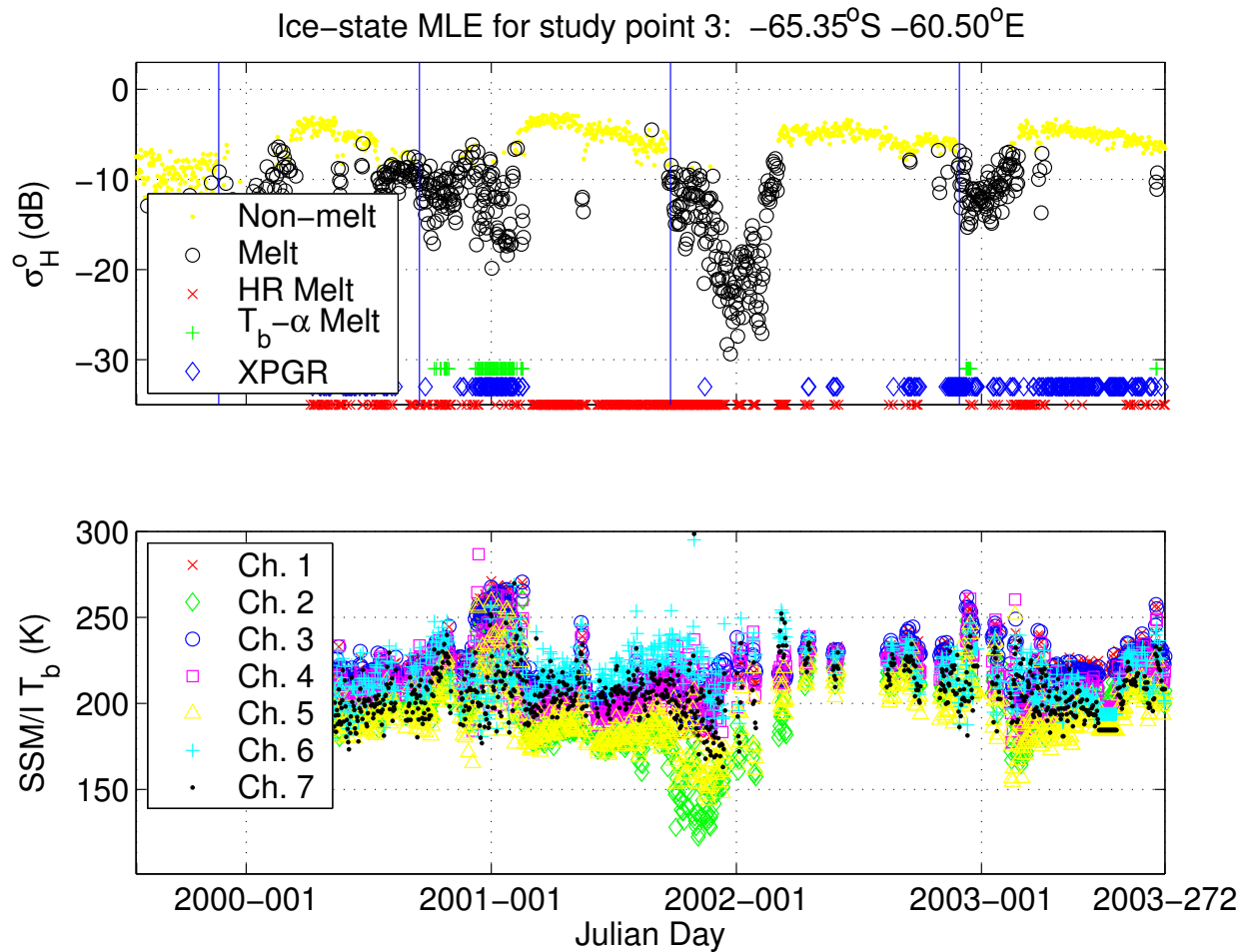
Figure A.2: Melt detection results for study point 1 from the ML method using QuikSCAT and the HR, T_b-α, and XPGR methods using SSM/I.

The ML method results for study point 1 are very intuitive. Periods of reduced backscatter are counted as melt events and these values coincide with peaks in the brightness temperatures observed by SSM/I. Note that melt events are classified for short periods of lower backscatter after the 2000-01 Austral summer and before the 2001-02 Austral summer. The T_b-α method also distinguishes these melt events while the XPGR method only detects the first of the two melt periods.
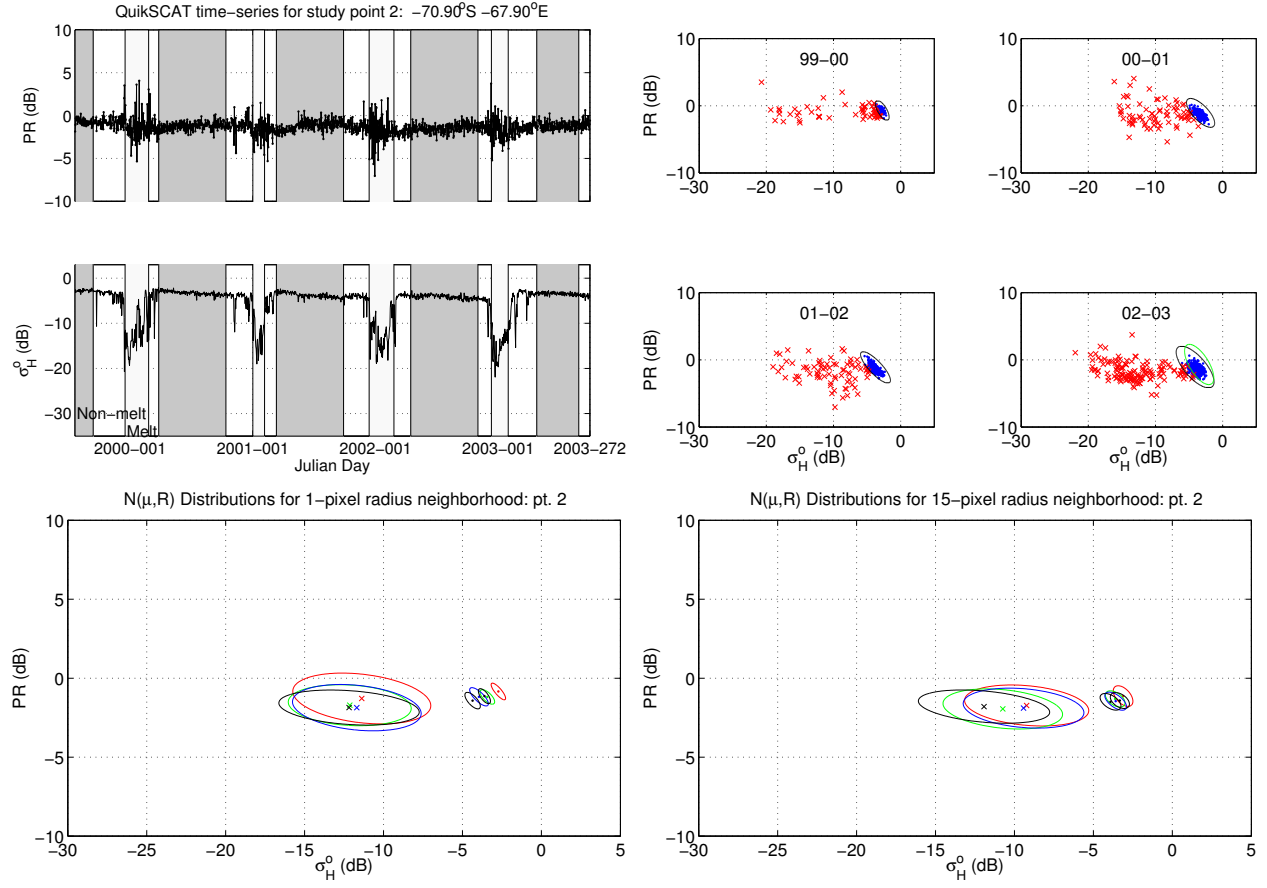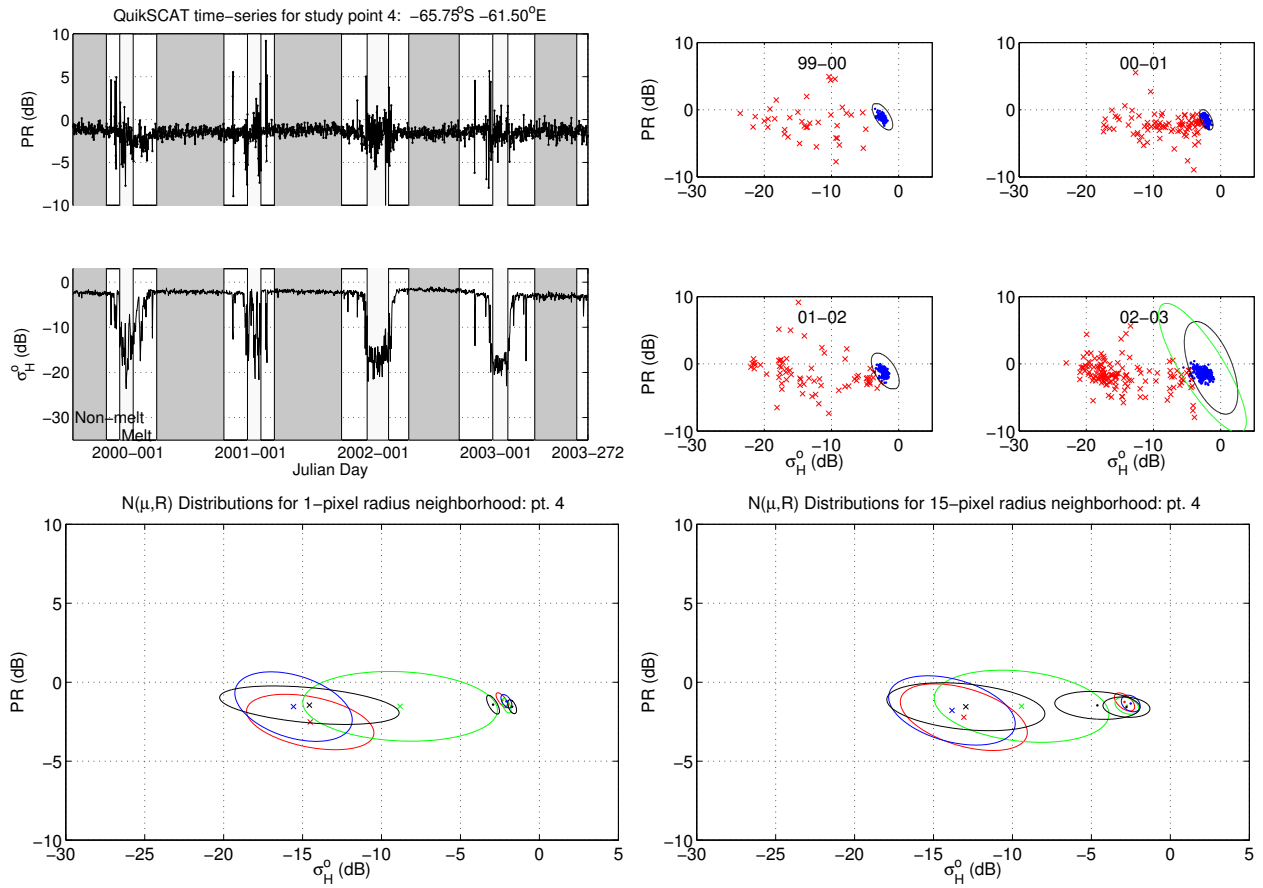
Figure A.3: ML melt detection results for study point 2.

$$\mathbf{R_0} = \begin{array}{cccc} 1999 & 2000 & 2001 & 2002 \\ \begin{bmatrix} 0.07 & -0.06 \\ -0.06 & 0.14 \end{bmatrix} & \begin{bmatrix} 0.21 & -0.14 \\ -0.14 & 0.21 \end{bmatrix} & \begin{bmatrix} 0.33 & -0.27 \\ -0.27 & 0.35 \end{bmatrix} & \begin{bmatrix} 0.22 & -0.16 \\ -0.16 & 0.24 \end{bmatrix} \end{array}$$

$$\mathbf{R_1} = \begin{array}{cccc} \begin{bmatrix} 18.03 & -1.66 \\ -1.66 & 2.58 \end{bmatrix} & \begin{bmatrix} 9.97 & -1.55 \\ -1.55 & 1.65 \end{bmatrix} & \begin{bmatrix} 13.48 & -2.16 \\ -2.16 & 2.88 \end{bmatrix} & \begin{bmatrix} 7.49 & -2.13 \\ -2.13 & 1.82 \end{bmatrix} \end{array}$$

$$\mathbf{m_0} = \begin{array}{cccc} \begin{bmatrix} -2.73 \\ -0.74 \end{bmatrix} & \begin{bmatrix} -3.29 \\ -1.22 \end{bmatrix} & \begin{bmatrix} -3.77 \\ -1.18 \end{bmatrix} & \begin{bmatrix} -4.11 \\ -1.46 \end{bmatrix} \end{array}$$

$$\mathbf{m_1} = \begin{array}{cccc} \begin{bmatrix} -11.55 \\ -1.28 \end{bmatrix} & \begin{bmatrix} -12.87 \\ -1.90 \end{bmatrix} & \begin{bmatrix} -12.18 \\ -1.77 \end{bmatrix} & \begin{bmatrix} -15.18 \\ -1.74 \end{bmatrix} \end{array}$$
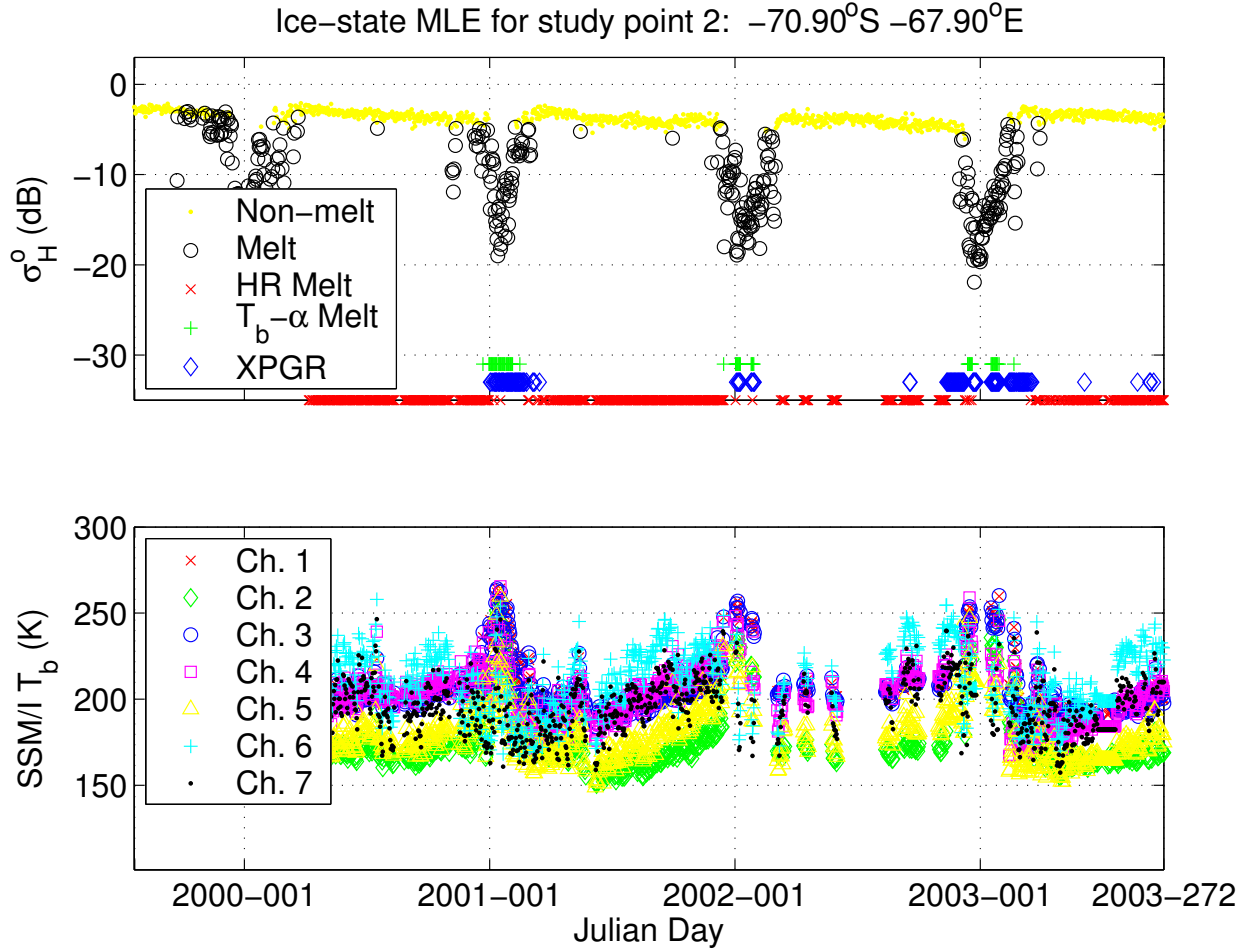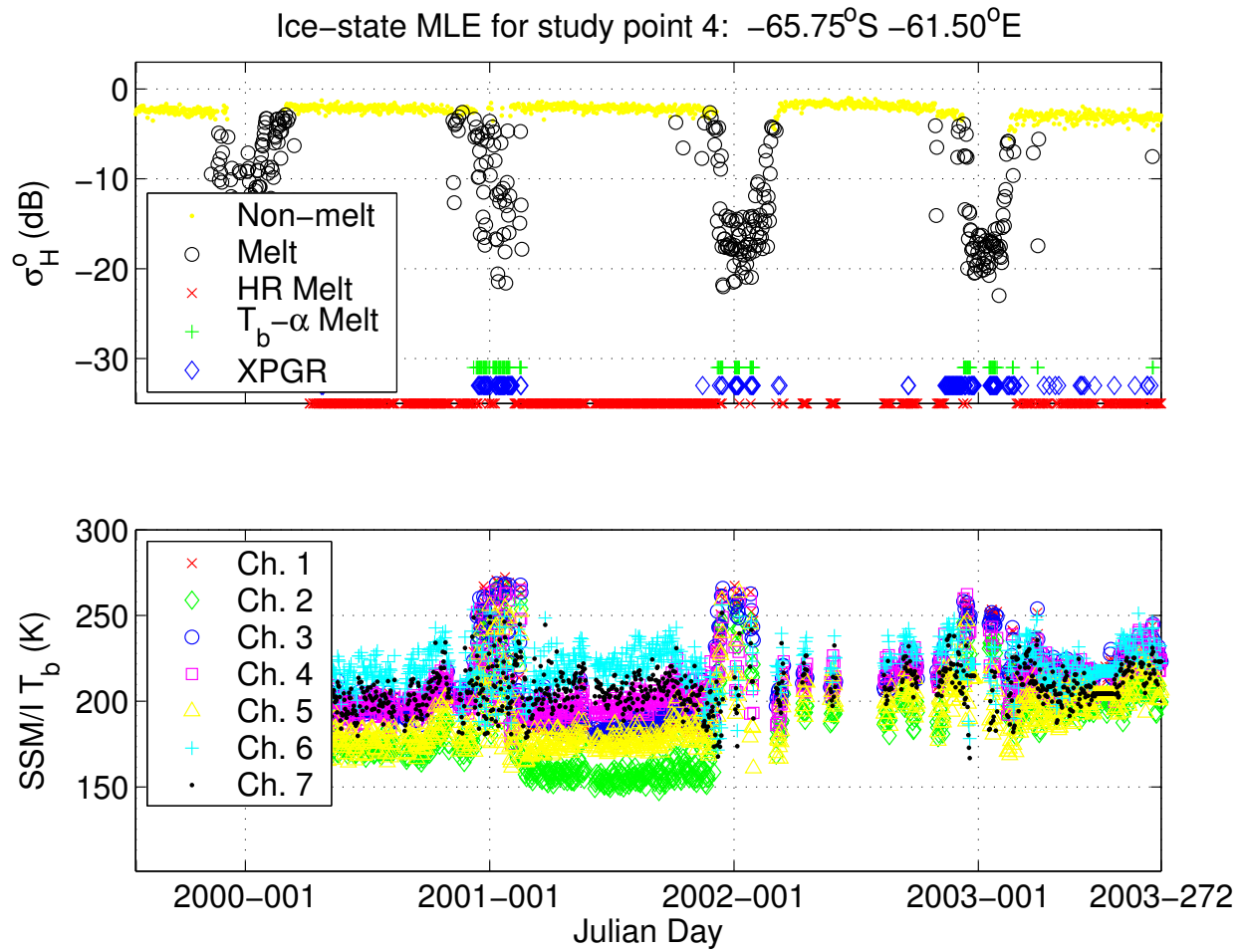
Figure A.4: Melt detection results for study point 2 from the ML method using QuikSCAT and the HR, T_b-α, and XPGR methods using SSM/I.

For study point 2 there is good correlation between the results from the ML, T_b-α, and XPGR methods. XPGR struggles in 2002-03 and the ML method detects single melt events in 2000 and 2001 that are questionable. However, these ML classifications do correspond with peaks in the Channel 6 SSM/I time-series. Again, the HR method appears to be invalid for the Antarctic ice-shelves. It consistently detects melt for nearly every day of the time-series for most of the 25 study points.
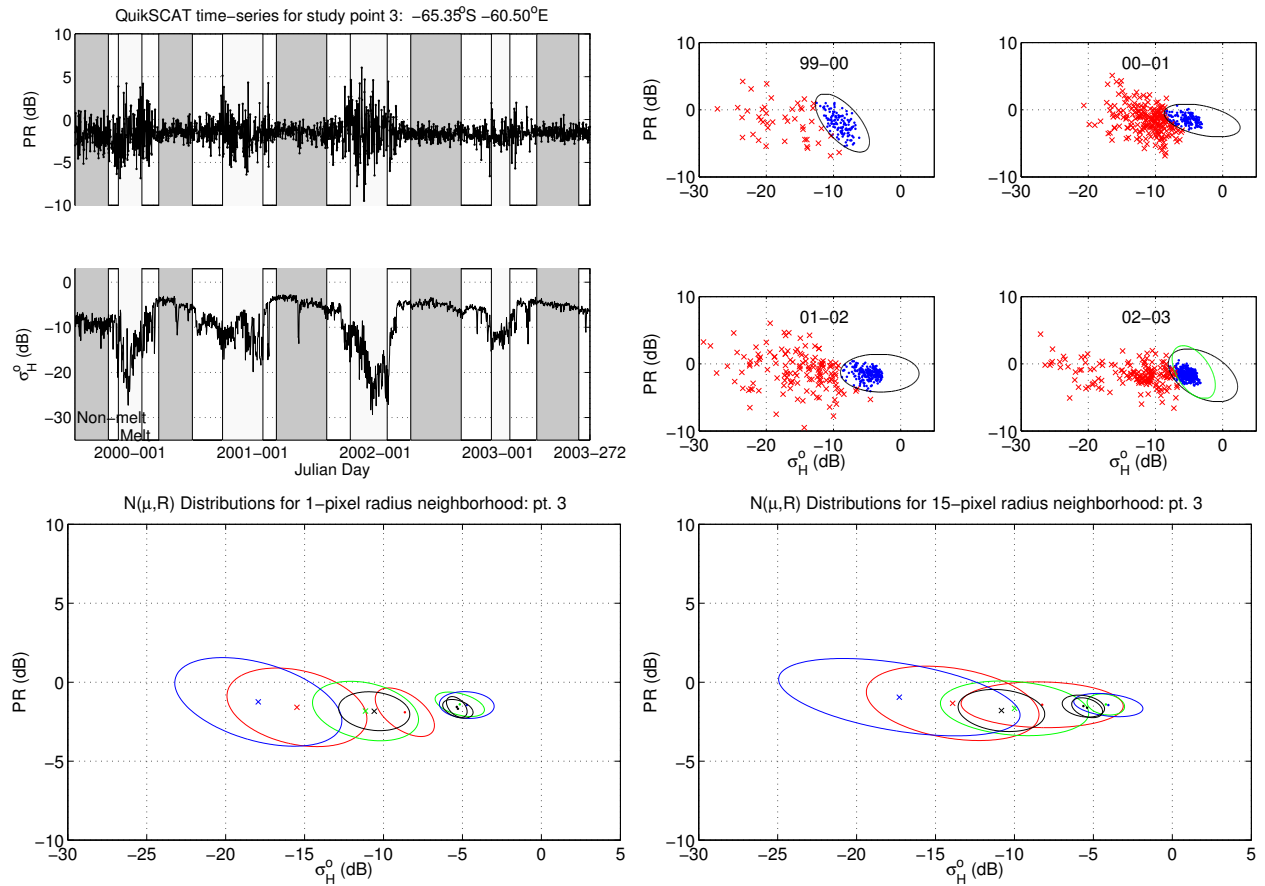
Figure A.5: ML melt detection results for study point 3.

|	1999	2000	2001	2002
$\mathbf{R_0} =$	$\begin{bmatrix} 2.13 & -1.23 \\ -1.23 & 2.06 \end{bmatrix}$	$\begin{bmatrix} 2.51 & -0.47 \\ -0.47 & 0.53 \end{bmatrix}$	$\begin{bmatrix} 2.40 & -0.05 \\ -0.05 & 0.57 \end{bmatrix}$	$\begin{bmatrix} 0.66 & -0.20 \\ -0.20 & 0.36 \end{bmatrix}$
$\mathbf{R_1} =$	$\begin{bmatrix} 20.11 & -3.86 \\ -3.86 & 6.41 \end{bmatrix}$	$\begin{bmatrix} 10.48 & -2.06 \\ -2.06 & 4.06 \end{bmatrix}$	$\begin{bmatrix} 26.35 & -3.60 \\ -3.60 & 7.94 \end{bmatrix}$	$\begin{bmatrix} 2.57 & -0.61 \\ -0.61 & 1.19 \end{bmatrix}$
$\mathbf{m_0} =$	$\begin{bmatrix} -9.28 \\ -1.85 \end{bmatrix}$	$\begin{bmatrix} -5.12 \\ -1.41 \end{bmatrix}$	$\begin{bmatrix} -4.52 \\ -1.46 \end{bmatrix}$	$\begin{bmatrix} -5.14 \\ -1.67 \end{bmatrix}$
$\mathbf{m_1} =$	$\begin{bmatrix} -15.87 \\ -1.61 \end{bmatrix}$	$\begin{bmatrix} -11.65 \\ -1.73 \end{bmatrix}$	$\begin{bmatrix} -18.00 \\ -1.02 \end{bmatrix}$	$\begin{bmatrix} -11.85 \\ -1.78 \end{bmatrix}$

Figure A.6: Melt detection results for study point 3 from the ML method using QuikSCAT and the HR, T_b-α, and XPGR methods using SSM/I.

The analysis for study point 3 is detailed in Chapter 3. To reiterate a key observation, the SSM/I observations are not as sensitive to the melt conditions during the 2001-02 melt season. The ML method clearly outperforms the other methods during the Austral summers of 2001-02 and 2002-03.

Figure A.7: ML melt detection results for study point 4.

$$
\begin{array}{ccccc}
& 1999 & 2000 & 2001 & 2002 \\[4pt]
\mathbf{R_0} = & \begin{bmatrix} 0.10 & -0.08 \\ -0.08 & 0.17 \end{bmatrix} & \begin{bmatrix} 0.08 & -0.06 \\ -0.06 & 0.19 \end{bmatrix} & \begin{bmatrix} 0.09 & -0.07 \\ -0.07 & 0.16 \end{bmatrix} & \begin{bmatrix} 0.07 & -0.06 \\ -0.06 & 0.20 \end{bmatrix} \\[12pt]
\mathbf{R_1} = & \begin{bmatrix} 16.54 & -2.89 \\ -2.89 & 3.35 \end{bmatrix} & \begin{bmatrix} 35.48 & -1.52 \\ -1.52 & 4.92 \end{bmatrix} & \begin{bmatrix} 8.14 & -2.75 \\ -2.75 & 3.95 \end{bmatrix} & \begin{bmatrix} 2.31 & -1.21 \\ -1.21 & 1.73 \end{bmatrix} \\[12pt]
\mathbf{m_0} = & \begin{bmatrix} -2.39 \\ -1.14 \end{bmatrix} & \begin{bmatrix} -2.15 \\ -1.47 \end{bmatrix} & \begin{bmatrix} -2.09 \\ -1.20 \end{bmatrix} & \begin{bmatrix} -1.73 \\ -1.59 \end{bmatrix} \\[12pt]
\mathbf{m_1} = & \begin{bmatrix} -14.47 \\ -2.33 \end{bmatrix} & \begin{bmatrix} -10.35 \\ -1.65 \end{bmatrix} & \begin{bmatrix} -16.59 \\ -1.68 \end{bmatrix} & \begin{bmatrix} -18.22 \\ -1.40 \end{bmatrix}
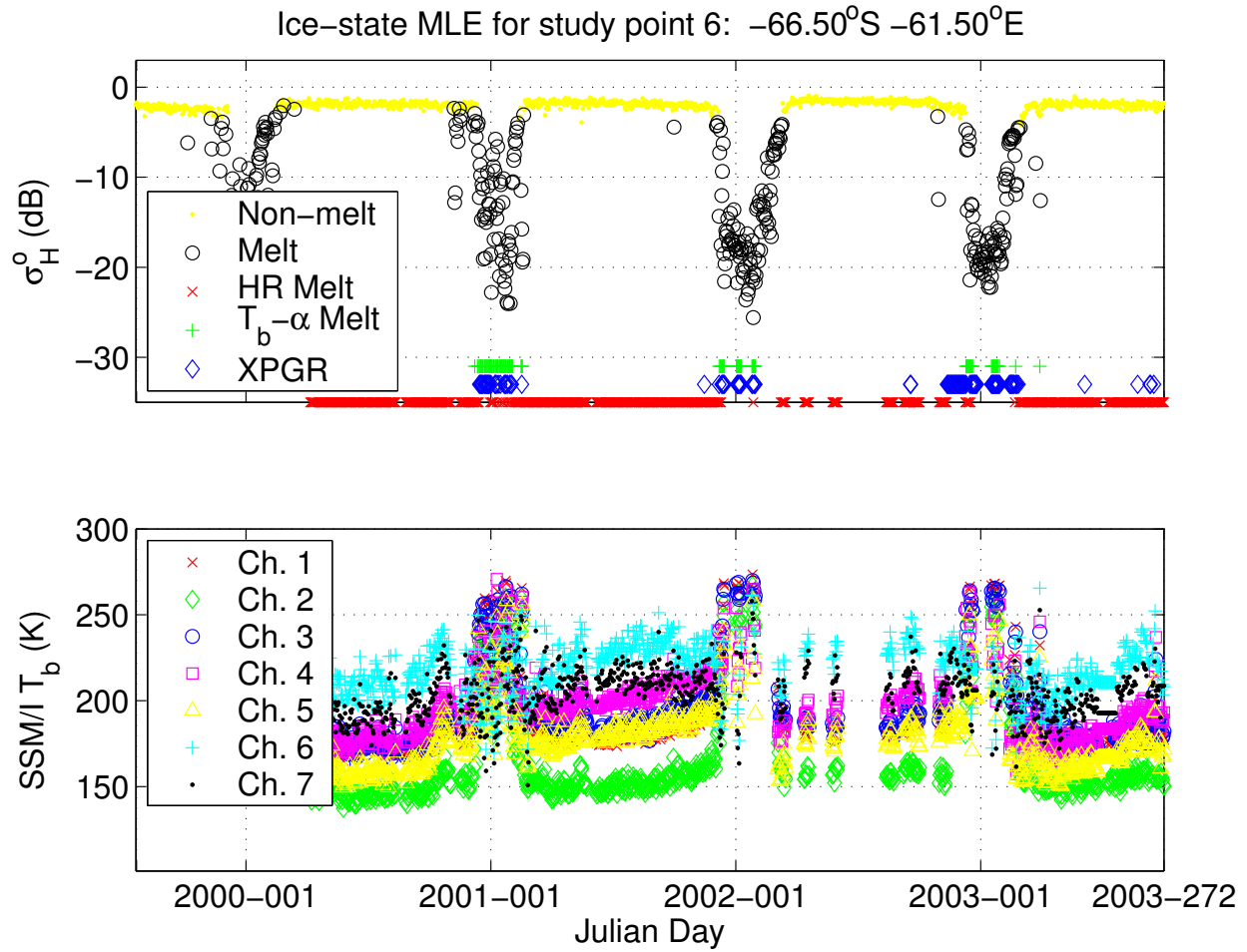\end{array}
$$

Figure A.8: Melt detection results for study point 4 from the ML method using QuikSCAT and the HR, T_b-α, and XPGR methods using SSM/I.

The QuikSCAT and SSM/I time-series for study point 4 yield very well defined melt events. Each method, except HR, performs well excluding the XPGR results for 2003.
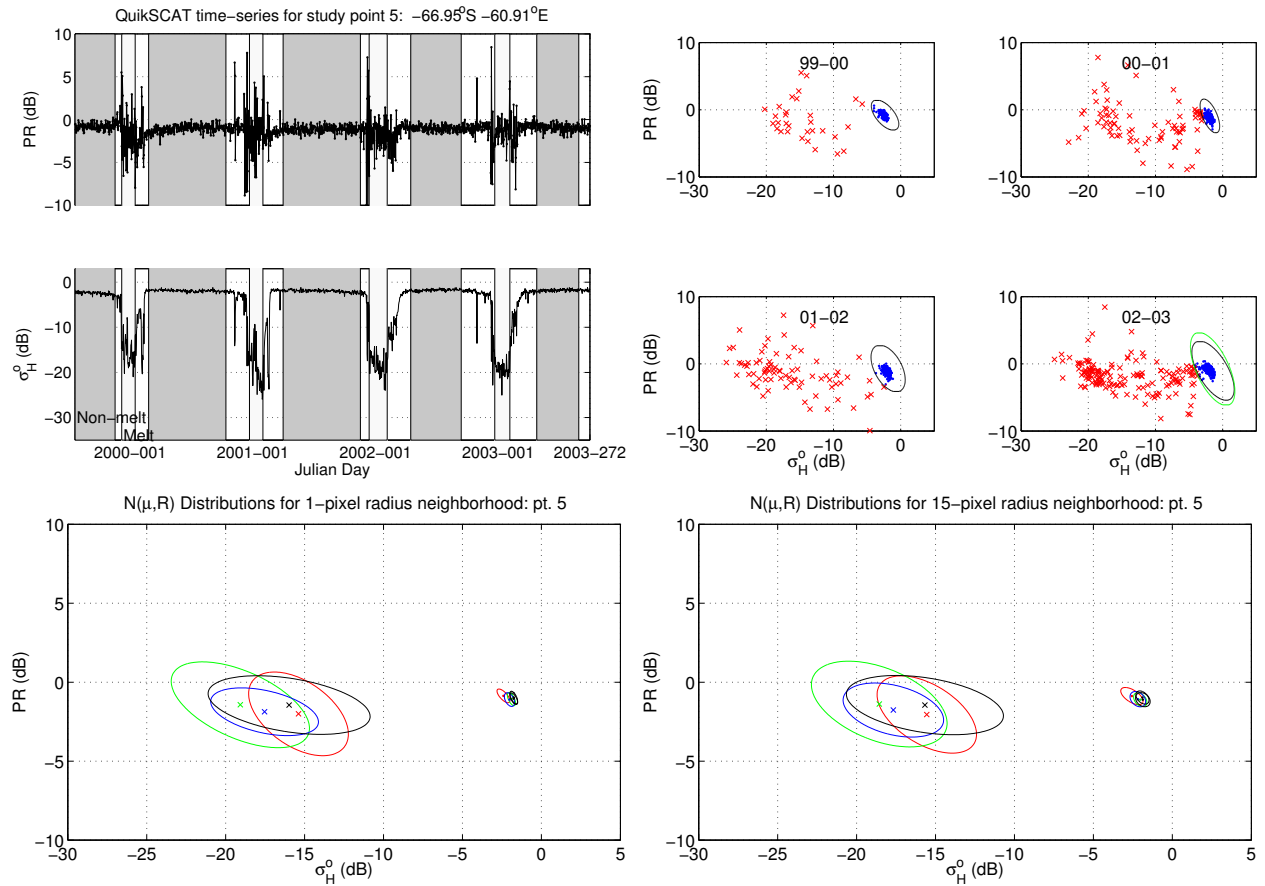
Figure A.9: ML melt detection results for study point 5.

$$\mathbf{R_0} = \begin{array}{cccc} 1999 & 2000 & 2001 & 2002 \\ \begin{bmatrix} 0.12 & -0.07 \\ -0.07 & 0.14 \end{bmatrix} & \begin{bmatrix} 0.06 & -0.06 \\ -0.06 & 0.18 \end{bmatrix} & \begin{bmatrix} 0.09 & -0.05 \\ -0.05 & 0.16 \end{bmatrix} & \begin{bmatrix} 0.06 & -0.05 \\ -0.05 & 0.11 \end{bmatrix} \end{array}$$

$$\mathbf{R_1} = \begin{bmatrix} 9.73 & -4.15 \\ -4.15 & 7.27 \end{bmatrix} \quad \begin{bmatrix} 17.83 & -5.83 \\ -5.83 & 6.73 \end{bmatrix} \quad \begin{bmatrix} 7.84 & -3.04 \\ -3.04 & 3.02 \end{bmatrix} \quad \begin{bmatrix} 2.59 & -1.11 \\ -1.11 & 2.36 \end{bmatrix}$$

$$\mathbf{m_0} = \begin{bmatrix} -2.45 \\ -0.81 \end{bmatrix} \quad \begin{bmatrix} -1.89 \\ -1.06 \end{bmatrix} \quad \begin{bmatrix} -1.96 \\ -1.13 \end{bmatrix} \quad \begin{bmatrix} -1.74 \\ -1.04 \end{bmatrix}$$

$$\mathbf{m_1} = \begin{bmatrix} -15.36 \\ -2.00 \end{bmatrix} \quad \begin{bmatrix} -18.93 \\ -1.55 \end{bmatrix} \quad \begin{bmatrix} -18.34 \\ -1.82 \end{bmatrix} \quad \begin{bmatrix} -19.18 \\ -1.19 \end{bmatrix}$$
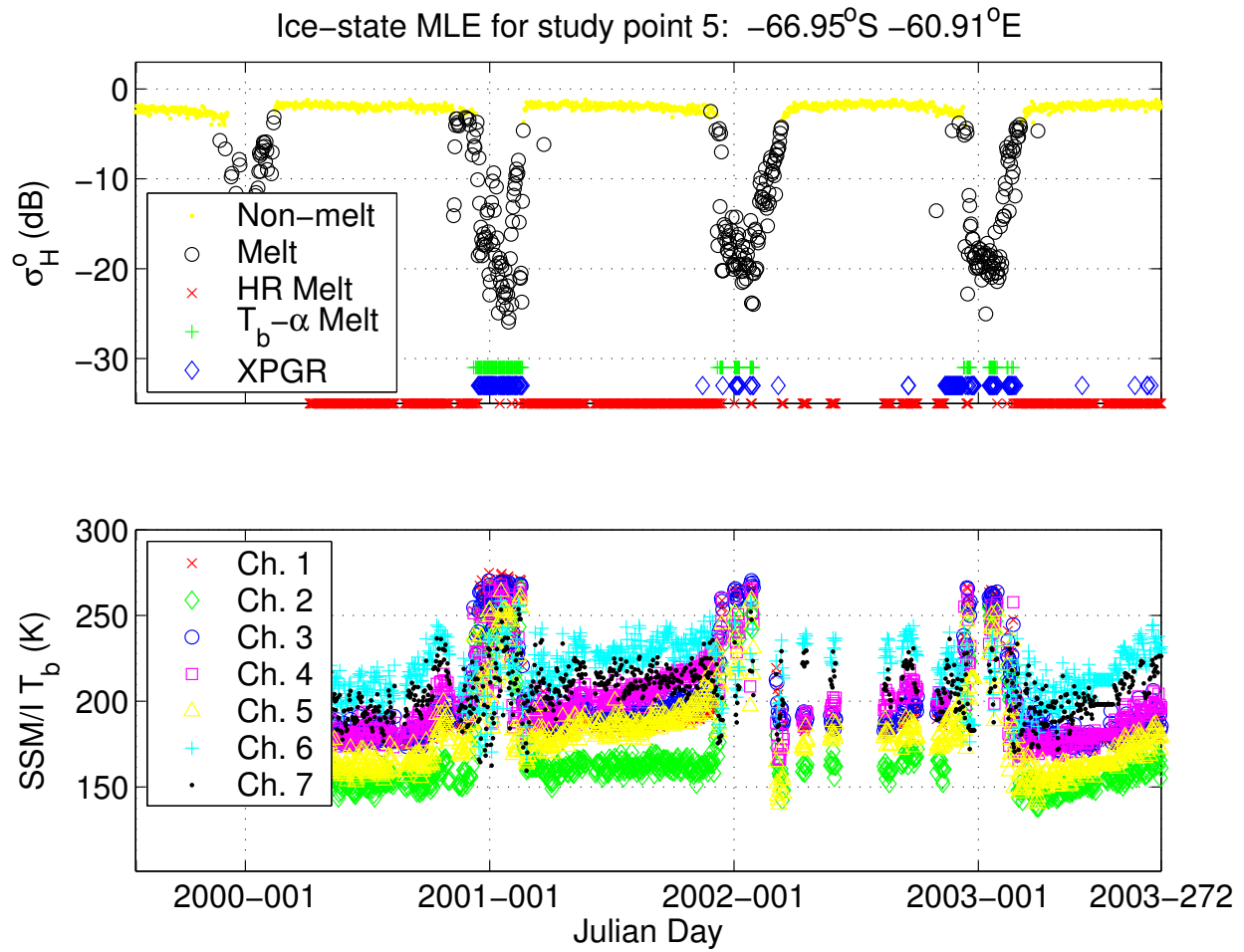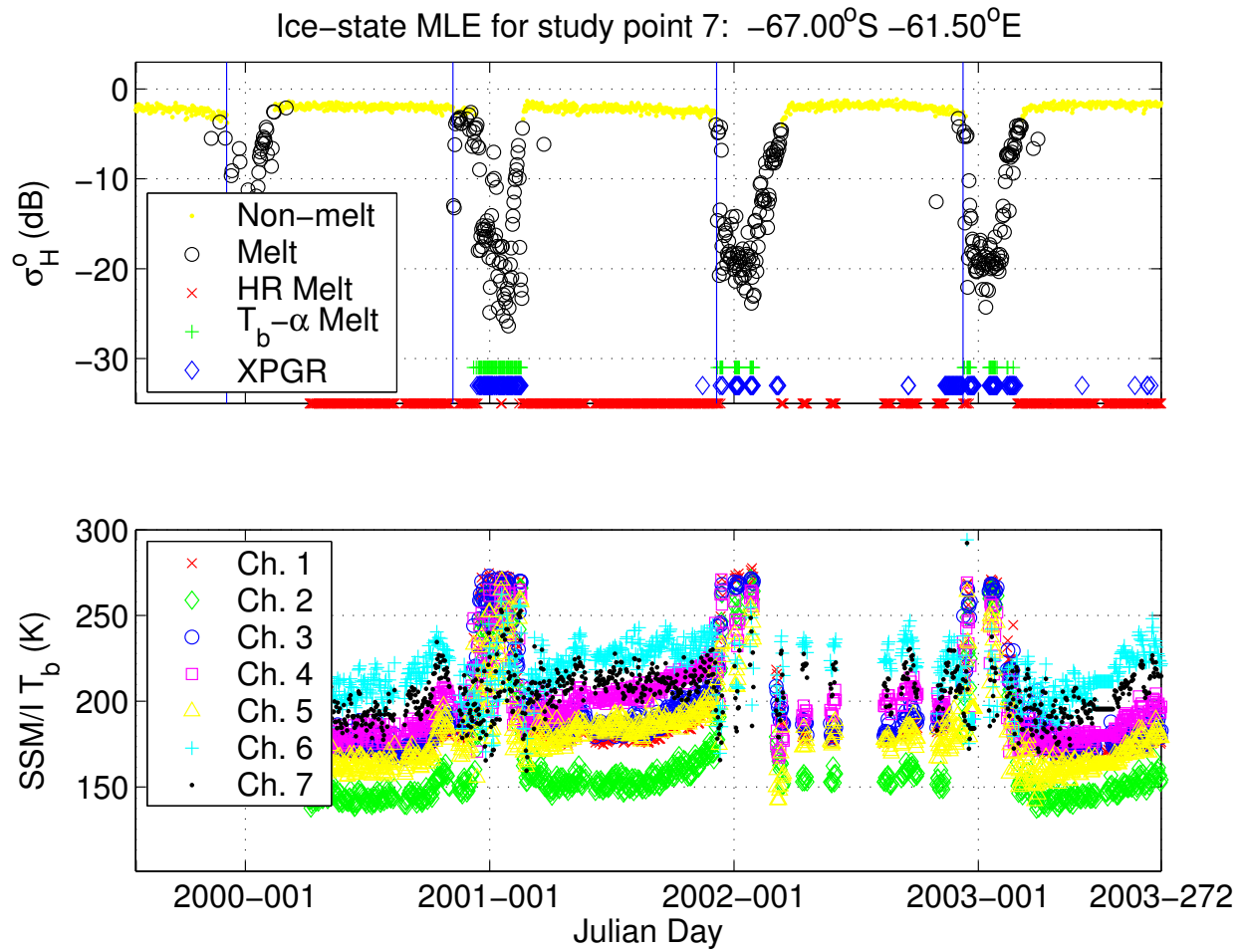
Figure A.10: Melt detection results for study point 5 from the ML method using QuikSCAT and the HR, T_b-α, and XPGR methods using SSM/I.

The analysis for study point 5 is the same as for point 4. QuikSCAT and SSM/I both exhibit high sensitivity to melting during the summer months.
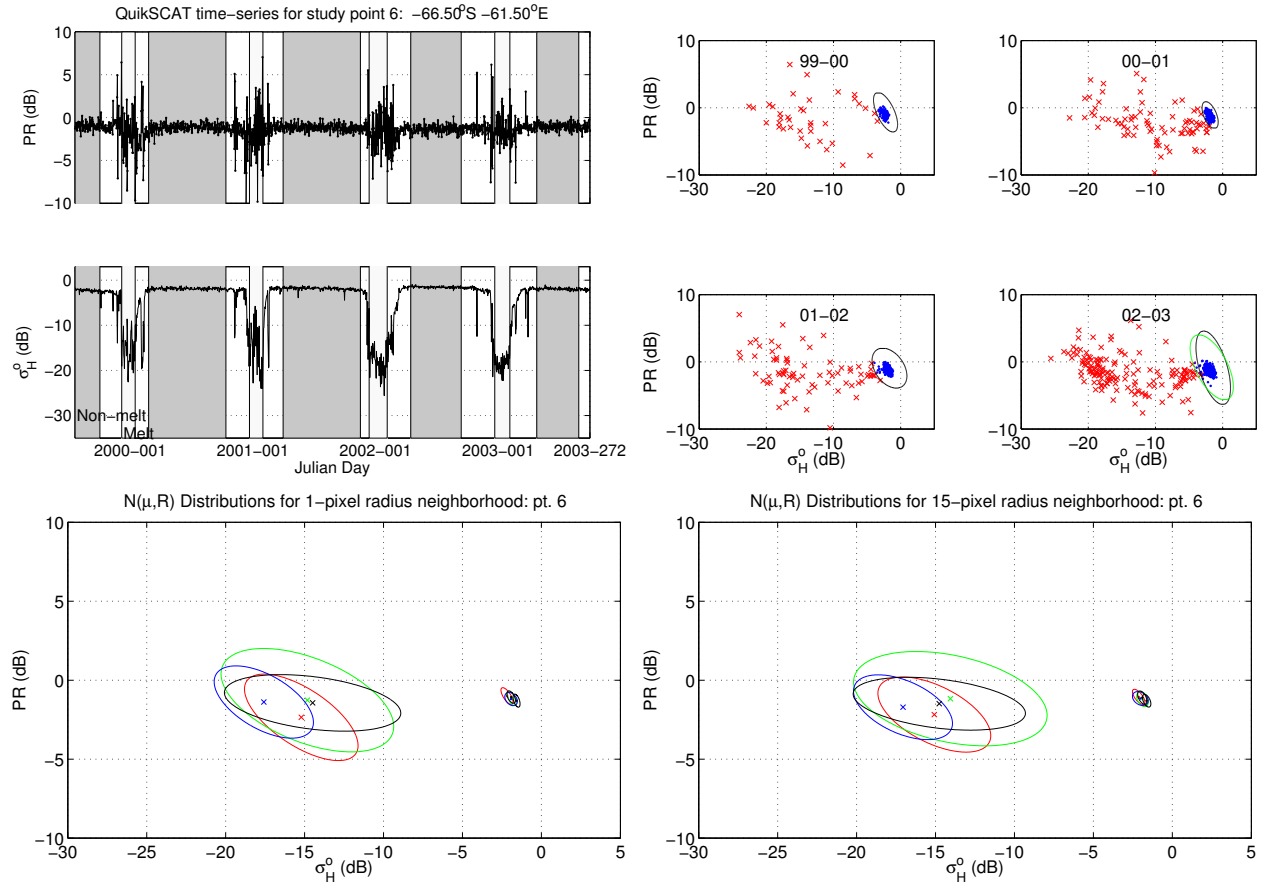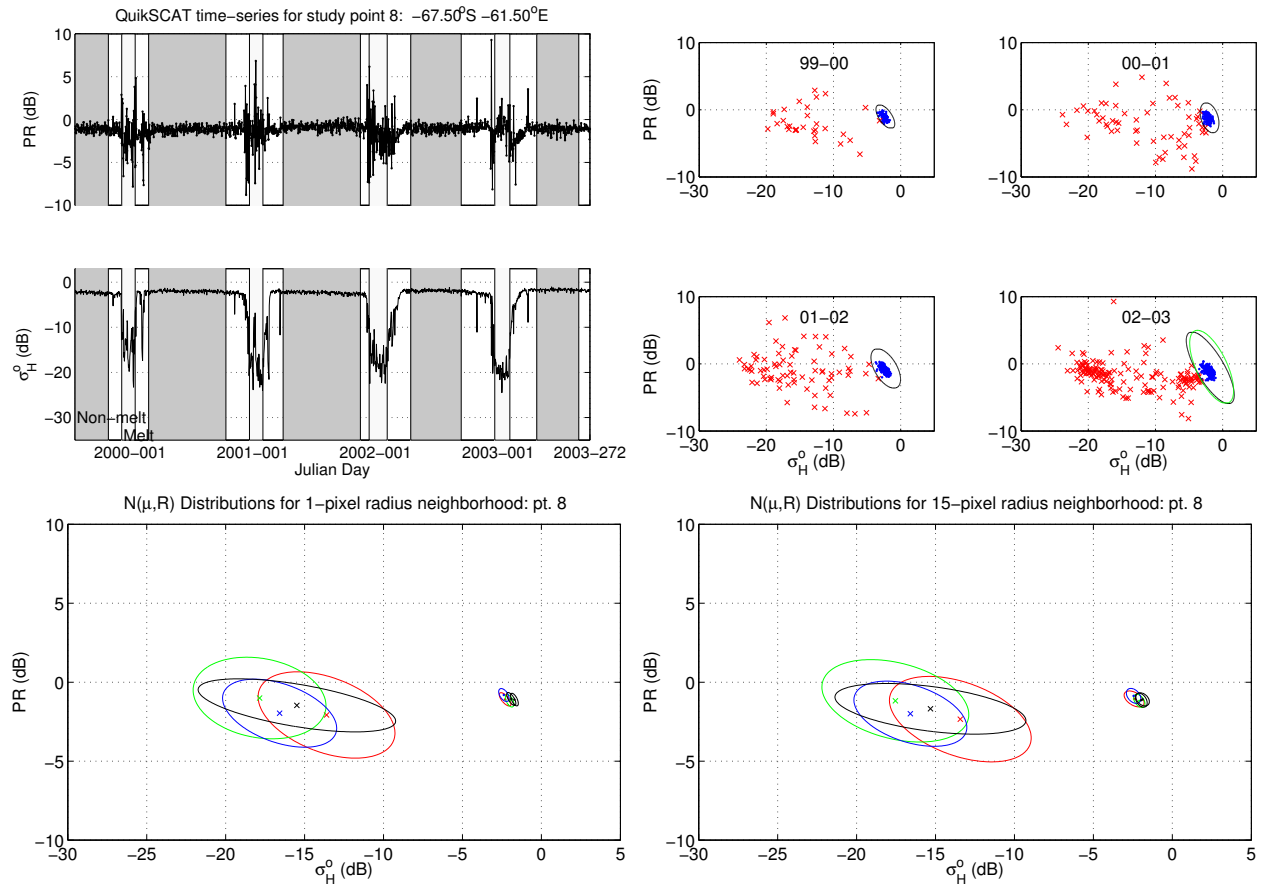
Figure A.11: ML melt detection results for study point 6.

$$
\begin{array}{ccccc}
 & 1999 & 2000 & 2001 & 2002 \\
\mathbf{R_0} = & \begin{bmatrix} 0.08 & -0.08 \\ -0.08 & 0.22 \end{bmatrix} & \begin{bmatrix} 0.06 & -0.06 \\ -0.06 & 0.19 \end{bmatrix} & \begin{bmatrix} 0.12 & -0.05 \\ -0.05 & 0.16 \end{bmatrix} & \begin{bmatrix} 0.04 & -0.05 \\ -0.05 & 0.19 \end{bmatrix} \\[20pt]
\mathbf{R_1} = & \begin{bmatrix} 13.07 & -6.29 \\ -6.29 & 6.88 \end{bmatrix} & \begin{bmatrix} 25.27 & -8.88 \\ -8.88 & 10.54 \end{bmatrix} & \begin{bmatrix} 9.87 & -4.37 \\ -4.37 & 5.07 \end{bmatrix} & \begin{bmatrix} 2.99 & -1.43 \\ -1.43 & 2.60 \end{bmatrix} \\[20pt]
\mathbf{m_0} = & \begin{bmatrix} -2.24 \\ -0.94 \end{bmatrix} & \begin{bmatrix} -1.87 \\ -1.16 \end{bmatrix} & \begin{bmatrix} -1.86 \\ -1.17 \end{bmatrix} & \begin{bmatrix} -1.52 \\ -1.34 \end{bmatrix} \\[20pt]
\mathbf{m_1} = & \begin{bmatrix} -15.43 \\ -2.26 \end{bmatrix} & \begin{bmatrix} -15.43 \\ -1.46 \end{bmatrix} & \begin{bmatrix} -18.12 \\ -1.42 \end{bmatrix} & \begin{bmatrix} -18.60 \\ -1.15 \end{bmatrix}
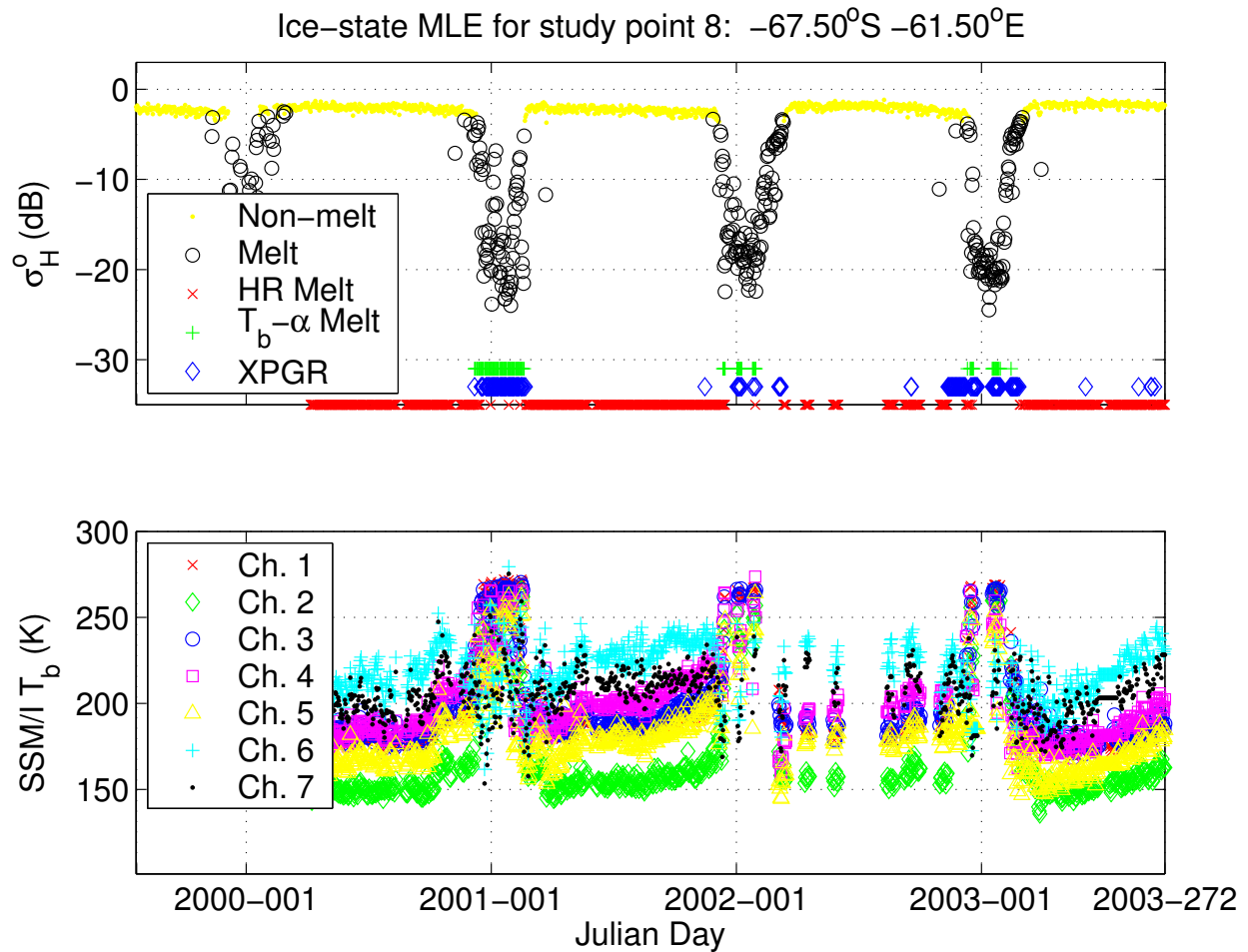\end{array}
$$

Figure A.12: Melt detection results for study point 6 from the ML method using QuikSCAT and the HR, T_b-α, and XPGR methods using SSM/I.

As with study points 4 and 5, the melt events for point 6 are also well defined; however, the SSM/I methods miss the initial melt onset of the 2000-01 melt season while the ML method is sensitive to the backscatter change during this minor melt period.
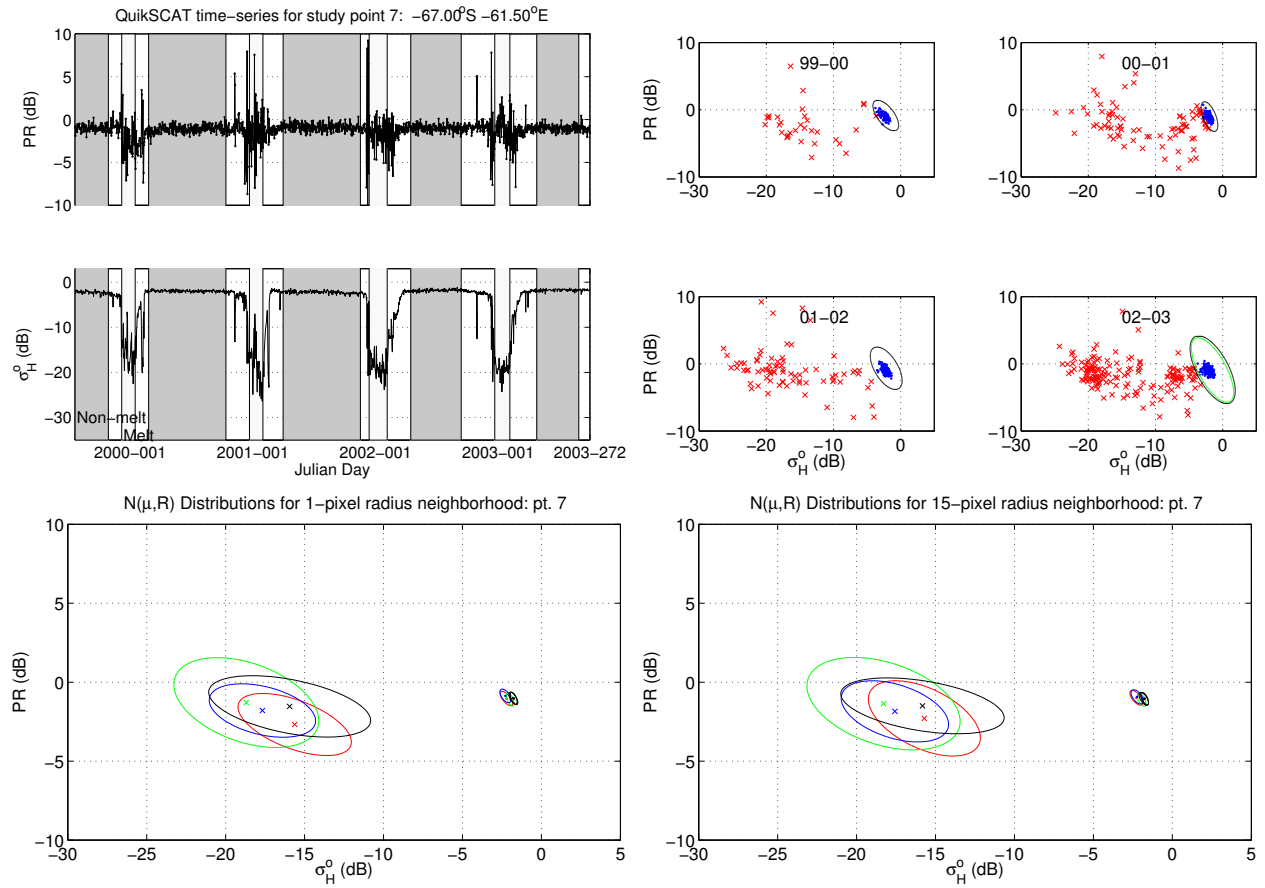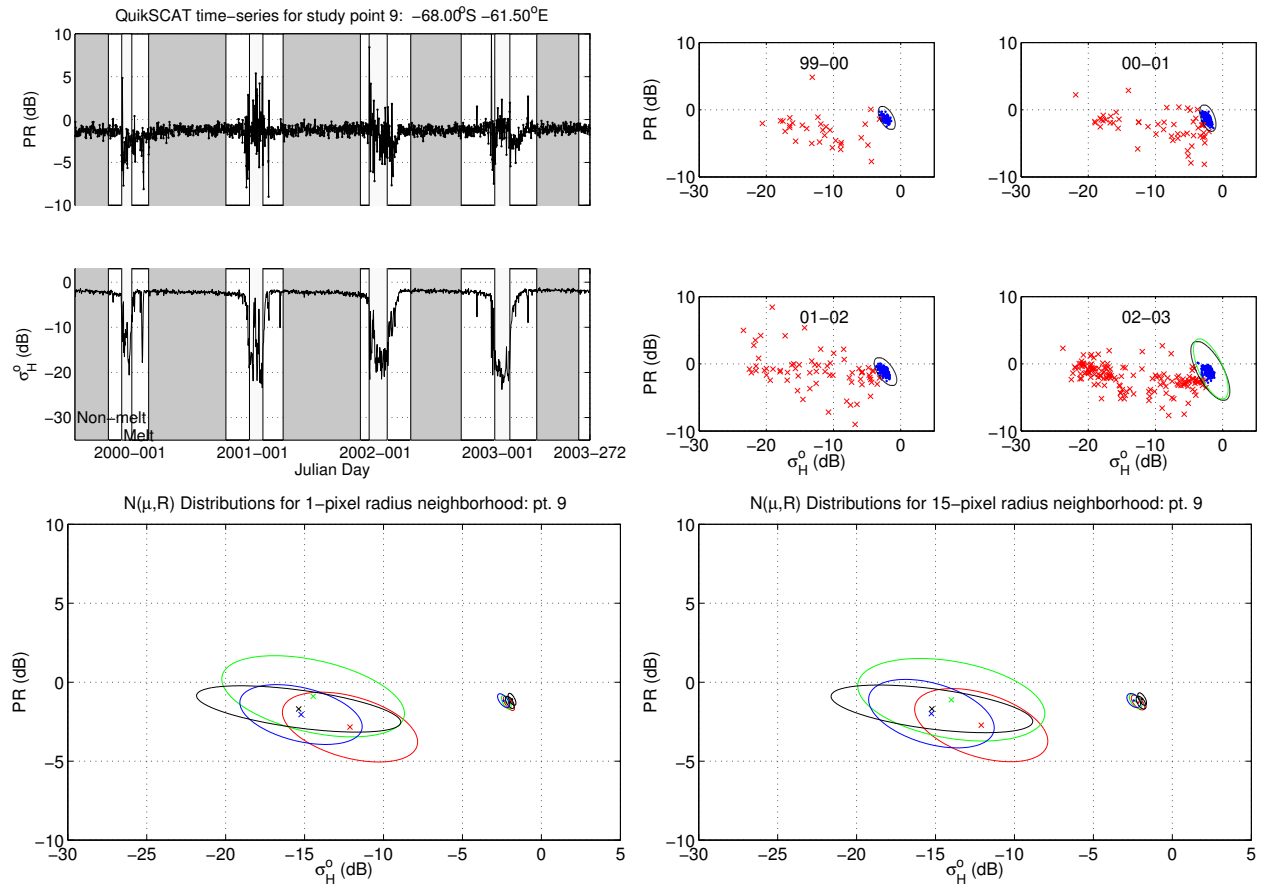
Figure A.13: ML melt detection results for study point 7.

$$
\begin{array}{cccc}
 & 1999 & 2000 & 2001 & 2002 \\
\mathbf{R_0} = \begin{bmatrix} 0.10 & -0.07 \\ -0.07 & 0.14 \end{bmatrix} & \begin{bmatrix} 0.05 & -0.06 \\ -0.06 & 0.18 \end{bmatrix} & \begin{bmatrix} 0.10 & -0.07 \\ -0.07 & 0.17 \end{bmatrix} & \begin{bmatrix} 0.06 & -0.06 \\ -0.06 & 0.15 \end{bmatrix} \\[2em]
\mathbf{R_1} = \begin{bmatrix} 12.16 & -3.56 \\ -3.56 & 3.85 \end{bmatrix} & \begin{bmatrix} 21.14 & -5.48 \\ -5.48 & 7.40 \end{bmatrix} & \begin{bmatrix} 7.79 & -1.67 \\ -1.67 & 2.20 \end{bmatrix} & \begin{bmatrix} 2.64 & -1.27 \\ -1.27 & 2.54 \end{bmatrix} \\[2em]
\mathbf{m_0} = \begin{bmatrix} -2.22 \\ -1.01 \end{bmatrix} & \begin{bmatrix} -1.97 \\ -1.08 \end{bmatrix} & \begin{bmatrix} -2.24 \\ -0.88 \end{bmatrix} & \begin{bmatrix} -1.80 \\ -0.99 \end{bmatrix} \\[2em]
\mathbf{m_1} = \begin{bmatrix} -15.55 \\ -2.67 \end{bmatrix} & \begin{bmatrix} -18.57 \\ -1.26 \end{bmatrix} & \begin{bmatrix} -18.55 \\ -1.59 \end{bmatrix} & \begin{bmatrix} -19.16 \\ -1.01 \end{bmatrix}
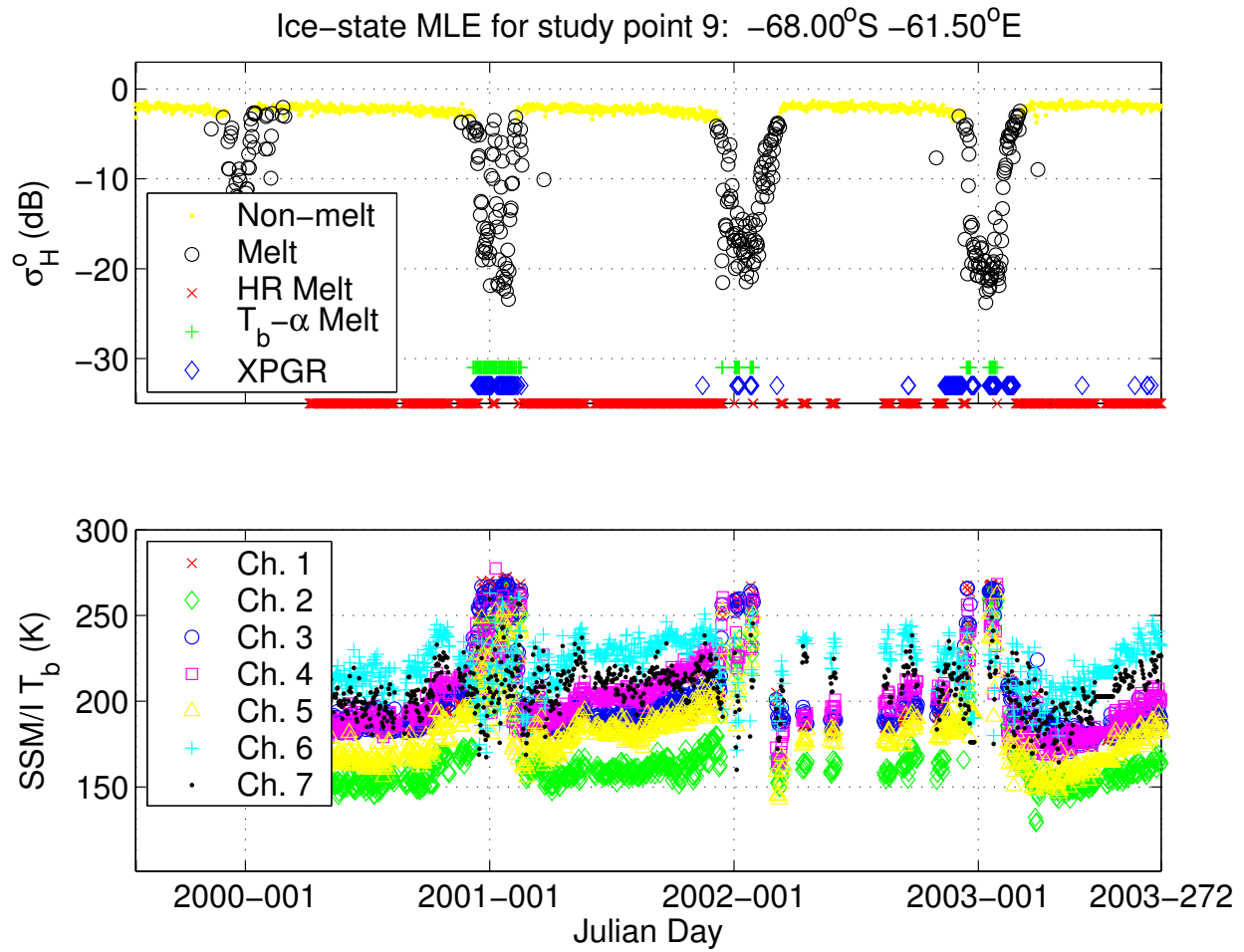\end{array}
$$

Figure A.14: Melt detection results for study point 7 from the ML method using QuikSCAT and the HR, T_b-α, and XPGR methods using SSM/I.

Chapter 3 discusses the results for this study point in great detail so no analysis is presented here.

Figure A.15: ML melt detection results for study point 8.

	1999	2000	2001	2002
$\mathbf{R_0} =$	$\begin{bmatrix} 0.08 & -0.06 \\ -0.06 & 0.13 \end{bmatrix}$	$\begin{bmatrix} 0.07 & -0.0441 \\ -0.04 & 0.19 \end{bmatrix}$	$\begin{bmatrix} 0.09 & -0.0704 \\ -0.07 & 0.16 \end{bmatrix}$	$\begin{bmatrix} 0.07 & -0.0855 \\ -0.08 & 0.16 \end{bmatrix}$
$\mathbf{R_1} =$	$\begin{bmatrix} 15.52 & -4.25 \\ -4.25 & 6.05 \end{bmatrix}$	$\begin{bmatrix} 17.00 & -1.43 \\ -1.43 & 6.28 \end{bmatrix}$	$\begin{bmatrix} 8.50 & -3.94 \\ -3.941 & 6.20 \end{bmatrix}$	$\begin{bmatrix} 3.39 & -1.54 \\ -1.54 & 1.86 \end{bmatrix}$
$\mathbf{m_0} =$	$\begin{bmatrix} -2.30 \\ -1.07 \end{bmatrix}$	$\begin{bmatrix} -2.01 \\ -1.18 \end{bmatrix}$	$\begin{bmatrix} -2.34 \\ -0.81 \end{bmatrix}$	$\begin{bmatrix} -1.88 \\ -1.05 \end{bmatrix}$
$\mathbf{m_1} =$	$\begin{bmatrix} -14.04 \\ -2.17 \end{bmatrix}$	$\begin{bmatrix} -18.17 \\ -0.94 \end{bmatrix}$	$\begin{bmatrix} -17.37 \\ -1.85 \end{bmatrix}$	$\begin{bmatrix} -19.55 \\ -0.90 \end{bmatrix}$

Figure A.16: Melt detection results for study point 8 from the ML method using QuikSCAT and the HR, T_b-α, and XPGR methods using SSM/I.

Study point 8 yields consistent results with other points on the Larsen shelf. XPGR is the only method, other than HR, that appears to make false melt classifications. Due to the lack of realistic results from the HR algorithm for Antarctic ice-shelves, no analysis of this method is presented for the remaining study points.

Figure A.17: ML melt detection results for study point 9.

$$
\mathbf{R_0} =
\begin{matrix}
& 1999 & 2000 & 2001 & 2002 \\
\end{matrix}
$$

$$
\mathbf{R_0} =
\begin{bmatrix} 0.08 & -0.06 \\ -0.06 & 0.15 \end{bmatrix}
\begin{bmatrix} 0.08 & -0.06 \\ -0.06 & 0.23 \end{bmatrix}
\begin{bmatrix} 0.11 & -0.08 \\ -0.08 & 0.18 \end{bmatrix}
\begin{bmatrix} 0.07 & -0.07 \\ -0.07 & 0.15 \end{bmatrix}
$$

$$
\mathbf{R_1} =
\begin{bmatrix} 16.66 & -3.71 \\ -3.71 & 4.77 \end{bmatrix}
\begin{bmatrix} 30.91 & -5.86 \\ -5.86 & 6.00 \end{bmatrix}
\begin{bmatrix} 14.23 & -3.00 \\ -3.00 & 6.02 \end{bmatrix}
\begin{bmatrix} 3.91 & -1.52 \\ -1.52 & 2.14 \end{bmatrix}
$$

$$
\mathbf{m_0} =
\begin{bmatrix} -2.07 \\ -1.32 \end{bmatrix}
\begin{bmatrix} -2.20 \\ -1.29 \end{bmatrix}
\begin{bmatrix} -2.32 \\ -1.15 \end{bmatrix}
\begin{bmatrix} -1.95 \\ -1.29 \end{bmatrix}
$$

$$
\mathbf{m_1} =
\begin{bmatrix} -12.20 \\ -3.05 \end{bmatrix}
\begin{bmatrix} -15.64 \\ -0.87 \end{bmatrix}
\begin{bmatrix} -15.81 \\ -1.46 \end{bmatrix}
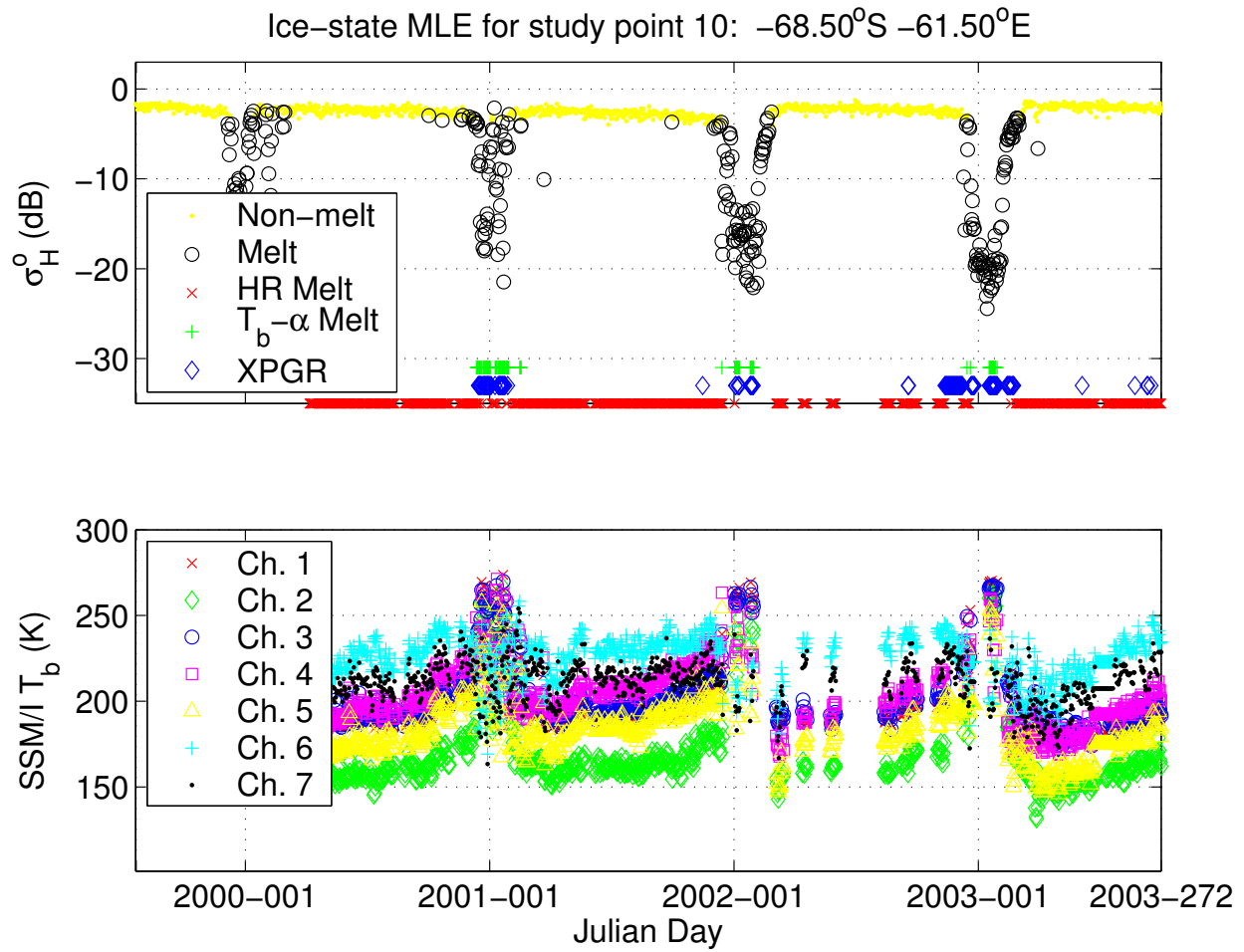\begin{bmatrix} -19.48 \\ -1.07 \end{bmatrix}
$$

Figure A.18: Melt detection results for study point 9 from the ML method using QuikSCAT and the HR, T_b-α, and XPGR methods using SSM/I.

The results for study point 9 are similar to study point 8.
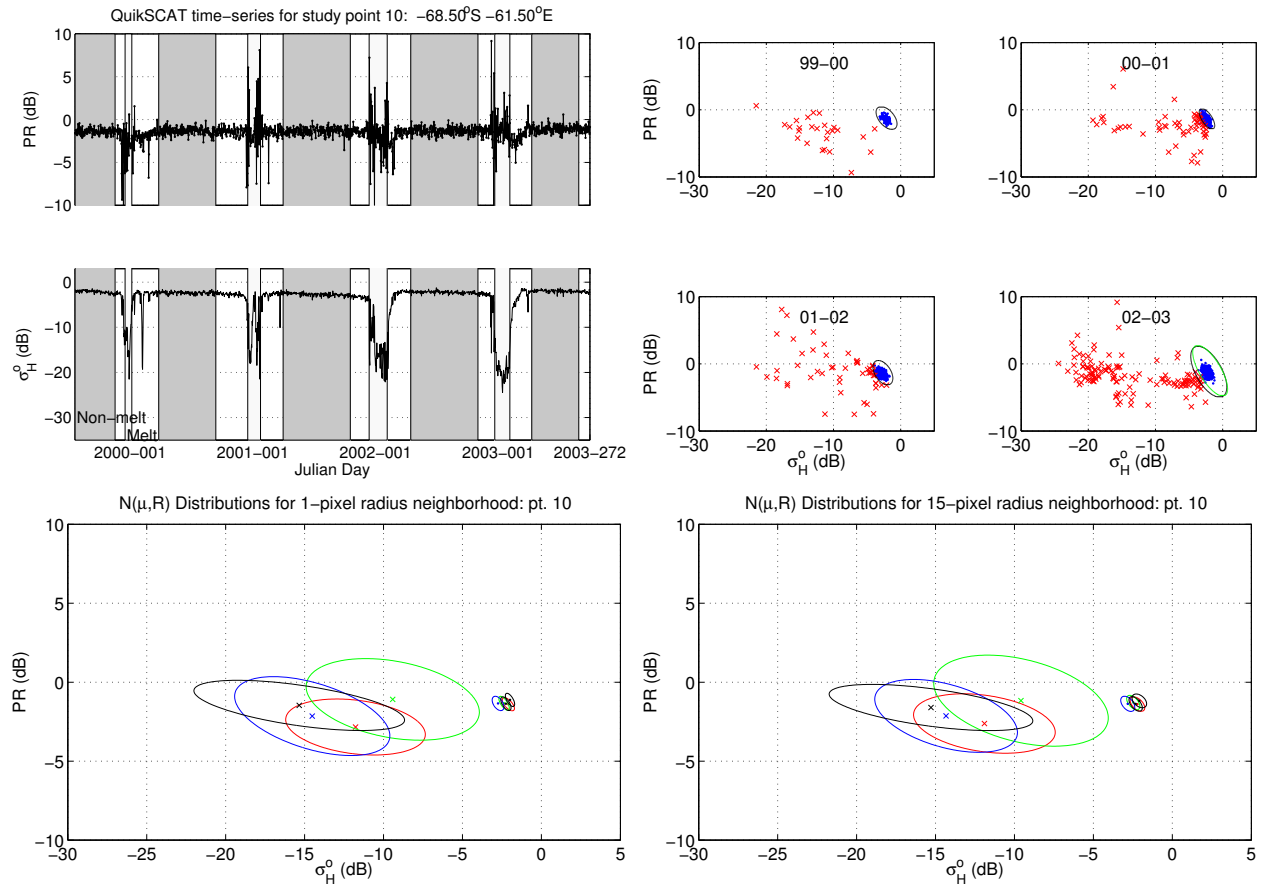
Figure A.19: ML melt detection results for study point 10.

$$
\begin{array}{ccccc}
& 1999 & 2000 & 2001 & 2002 \\[4pt]
\mathbf{R_0} = & \begin{bmatrix} 0.11 & -0.06 \\ -0.06 & 0.13 \end{bmatrix} & \begin{bmatrix} 0.10 & -0.09 \\ -0.09 & 0.18 \end{bmatrix} & \begin{bmatrix} 0.13 & -0.07 \\ -0.07 & 0.19 \end{bmatrix} & \begin{bmatrix} 0.09 & -0.08 \\ -0.08 & 0.18 \end{bmatrix} \\[12pt]
\mathbf{R_1} = & \begin{bmatrix} 14.14 & -2.30 \\ -2.30 & 2.41 \end{bmatrix} & \begin{bmatrix} 30.64 & -7.25 \\ -7.25 & 10.02 \end{bmatrix} & \begin{bmatrix} 22.70 & -4.69 \\ -4.69 & 8.53 \end{bmatrix} & \begin{bmatrix} 5.71 & -2.02 \\ -2.02 & 3.30 \end{bmatrix} \\[12pt]
\mathbf{m_0} = & \begin{bmatrix} -2.11 \\ -1.37 \end{bmatrix} & \begin{bmatrix} -2.34 \\ -1.34 \end{bmatrix} & \begin{bmatrix} -2.69 \\ -1.34 \end{bmatrix} & \begin{bmatrix} -2.24 \\ -1.30 \end{bmatrix} \\[12pt]
\mathbf{m_1} = & \begin{bmatrix} -12.57 \\ -2.81 \end{bmatrix} & \begin{bmatrix} -10.44 \\ -1.11 \end{bmatrix} & \begin{bmatrix} -14.67 \\ -1.77 \end{bmatrix} & \begin{bmatrix} -19.20 \\ -1.17 \end{bmatrix}
\end{array}
$$

Figure A.20: Melt detection results for study point 10 from the ML method using QuikSCAT and the HR, T_b-α, and XPGR methods using SSM/I.

Study point 10 melt detection results mirror those from points 8 and 9.
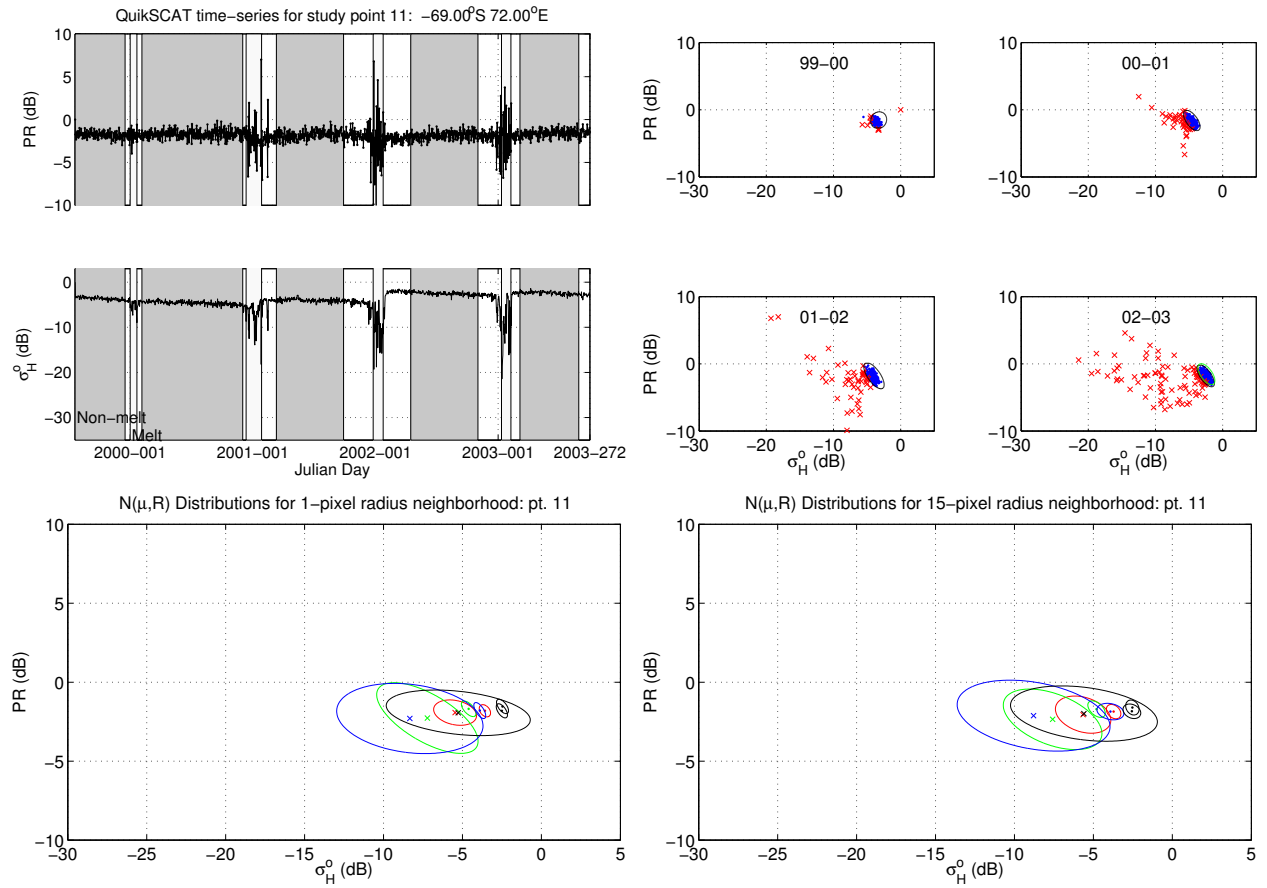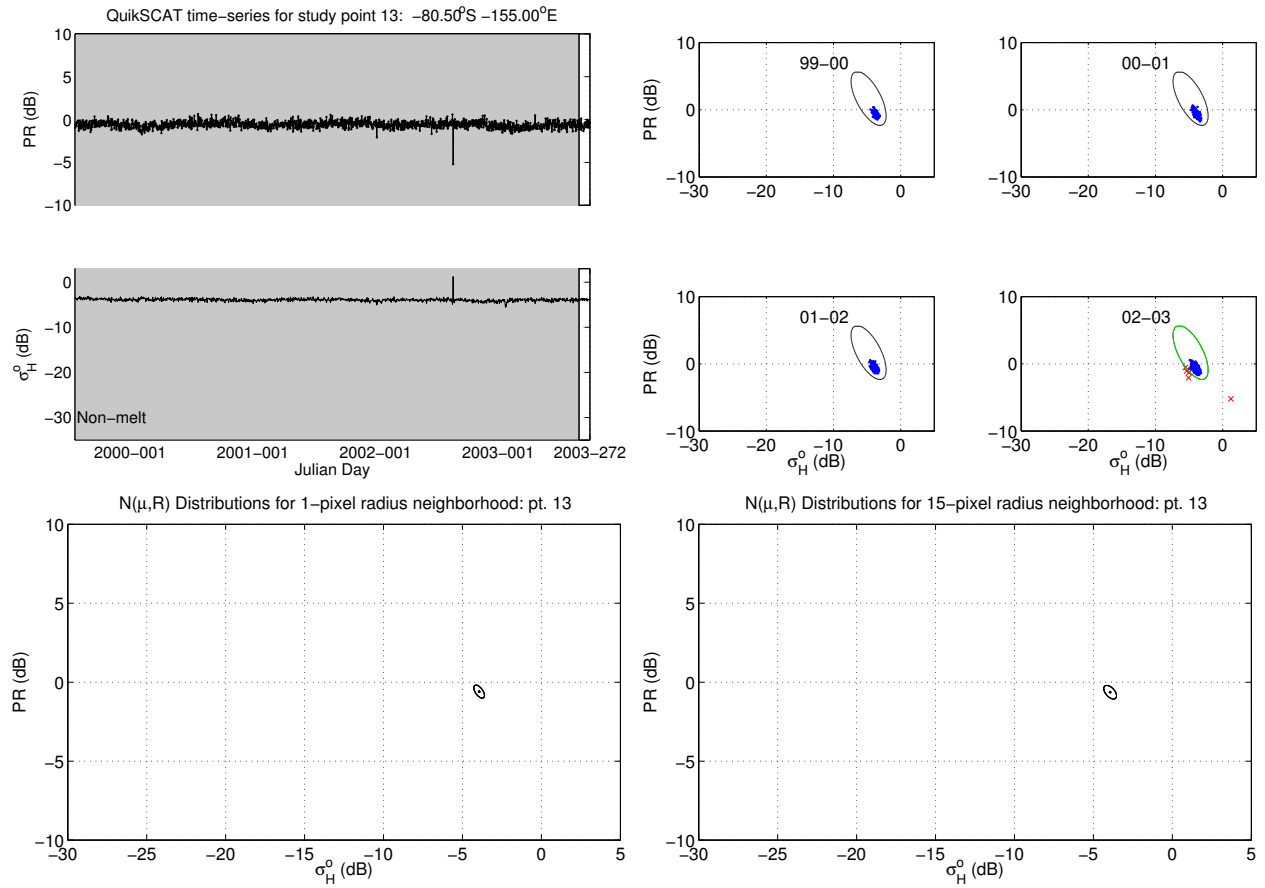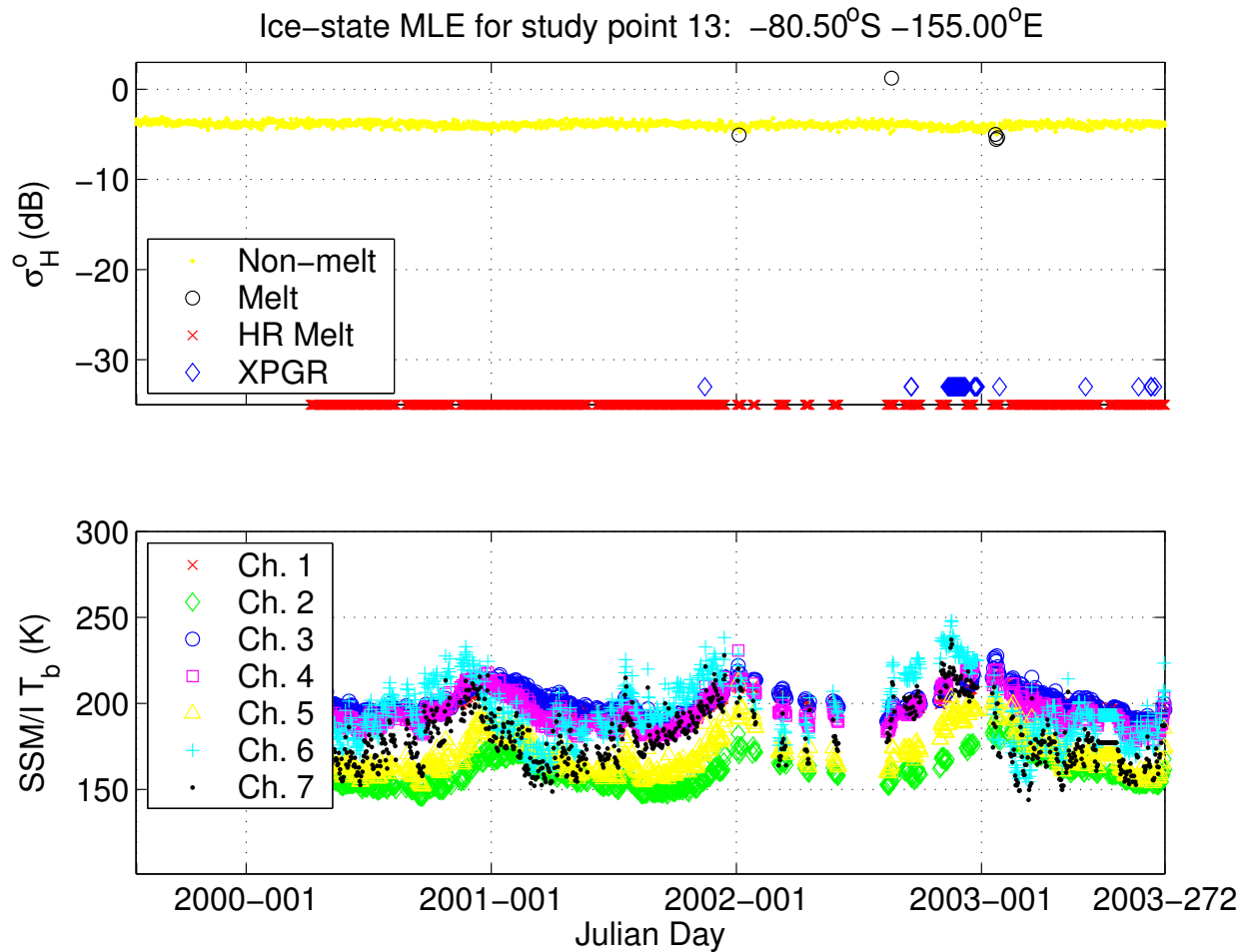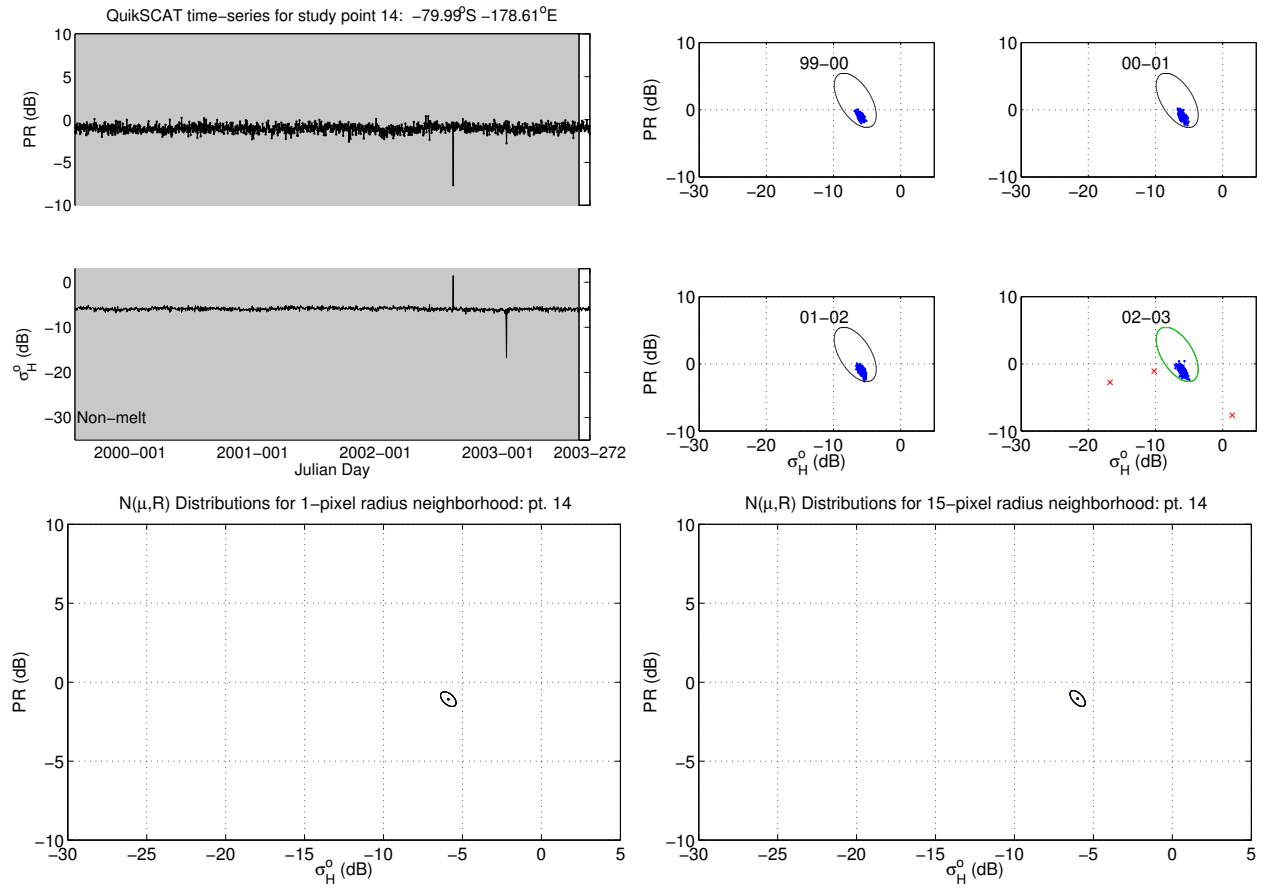
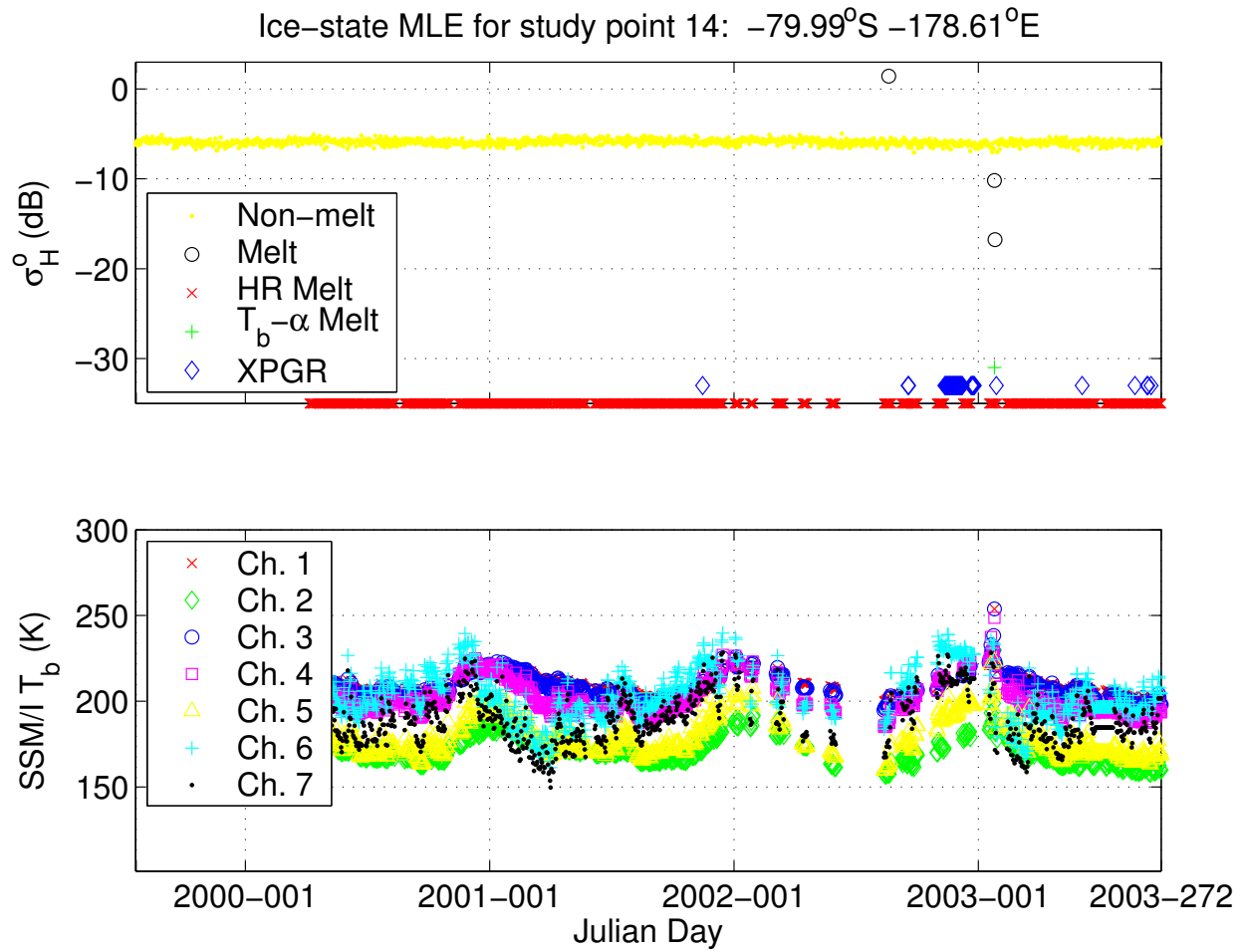Figure A.21: ML melt detection results for study point 11.
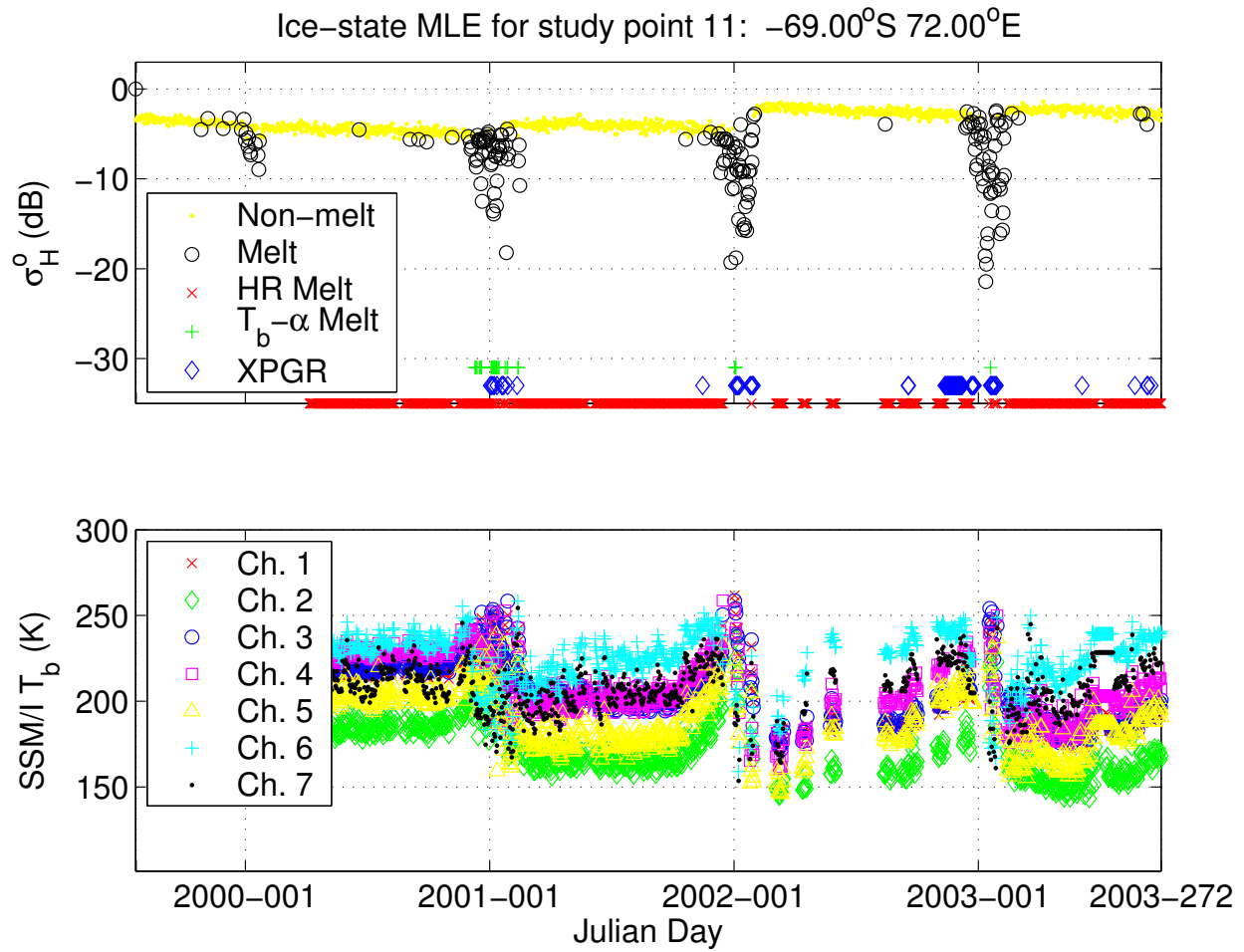
Figure A.22: Melt detection results for study point 11 from the ML method using QuikSCAT and the HR, $T_b\text{-}\alpha$, and XPGR methods using SSM/I.

For study point 11, the melt and non-melt distributions overlap much more than for the 10 points on the Antarctic peninsula (points 1-10). This does not seem to be a problem, however, since each of the methods perform fairly well. The ML method identifies more melt days than the other SSM/I methods, but only a few of these classifications during 1999 and 2000 are questionable.
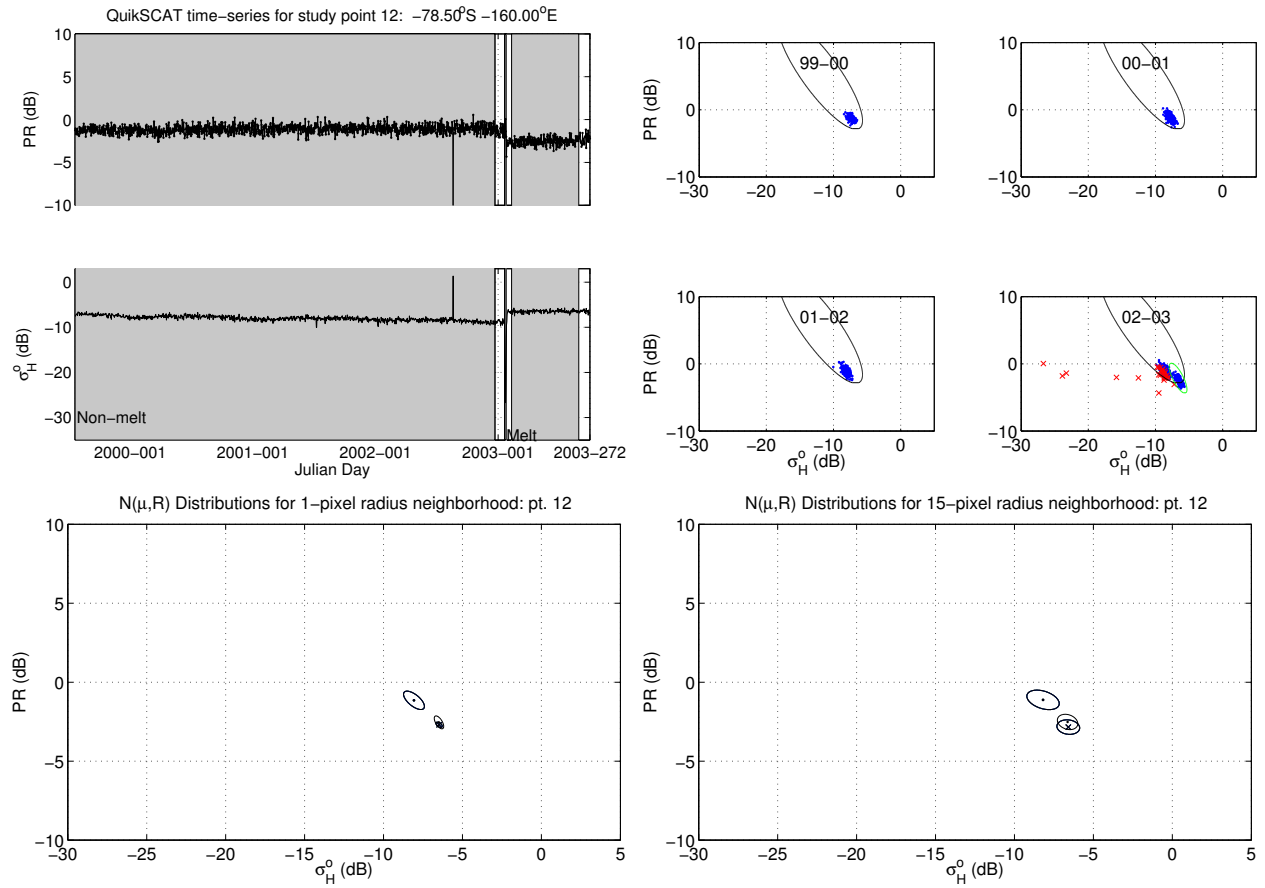
Figure A.23: ML melt detection results for study point 12.
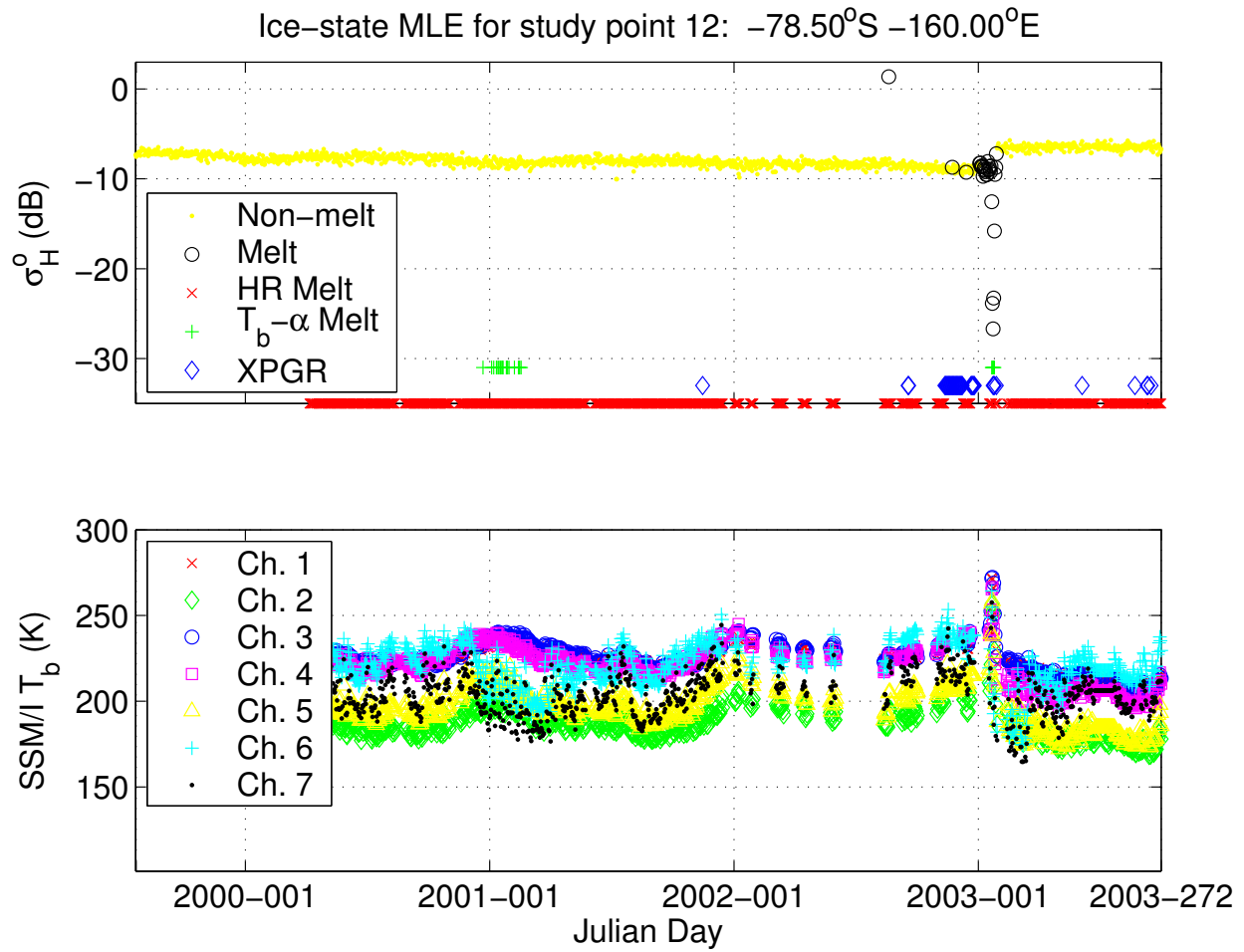
Figure A.24: Melt detection results for study point 12 from the ML method using QuikSCAT and the HR, T_b-α, and XPGR methods using SSM/I.

This study point undergoes only a short melt period from 2002-03, but the ML melt detection results are still good. The T_b-α and XPGR methods do not correlate well.
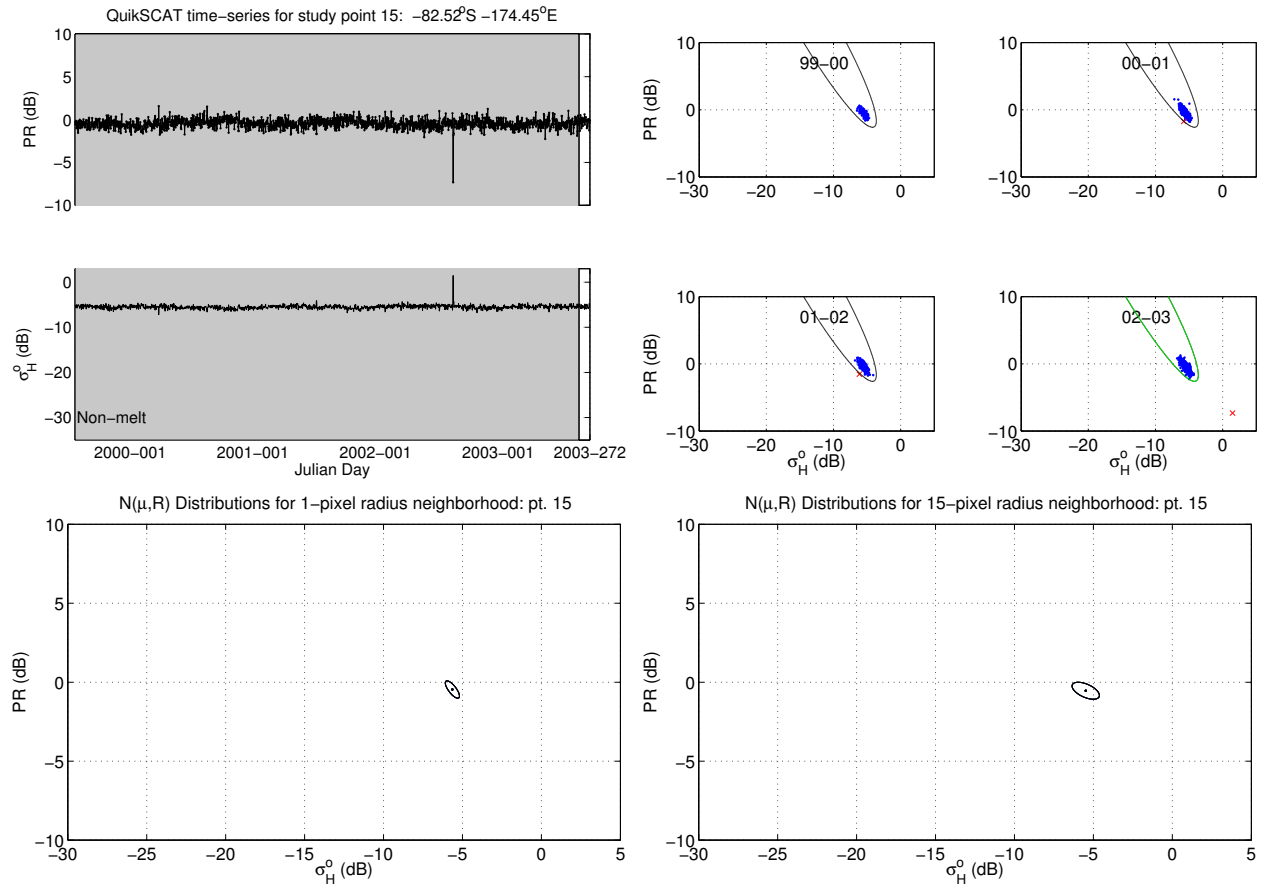
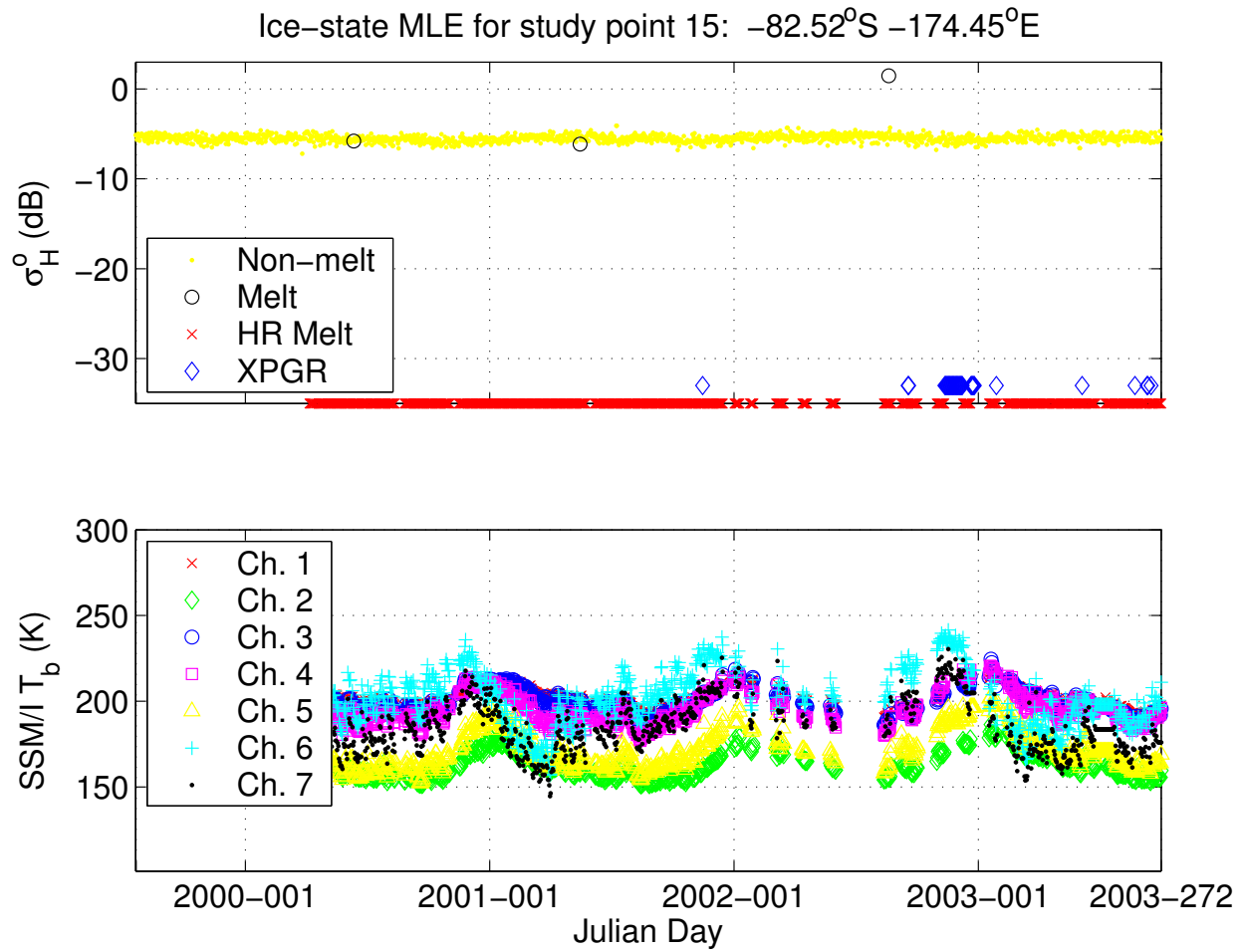Figure A.25: ML melt detection results for study point 13.

Figure A.26: Melt detection results for study point 13 from the ML method using QuikSCAT and the HR, T_b-α, and XPGR methods using SSM/I.

No extended melt periods are observed in the backscatter time-series for study point 13. For the ML method, the covariance and mean values for melt season of study point 12 are used. The ML method identifies some days as melt even though a large drop in backscatter is not observed. These melt events do coincide with increased T_b values though it is not likely that significant melting occurs at these times.
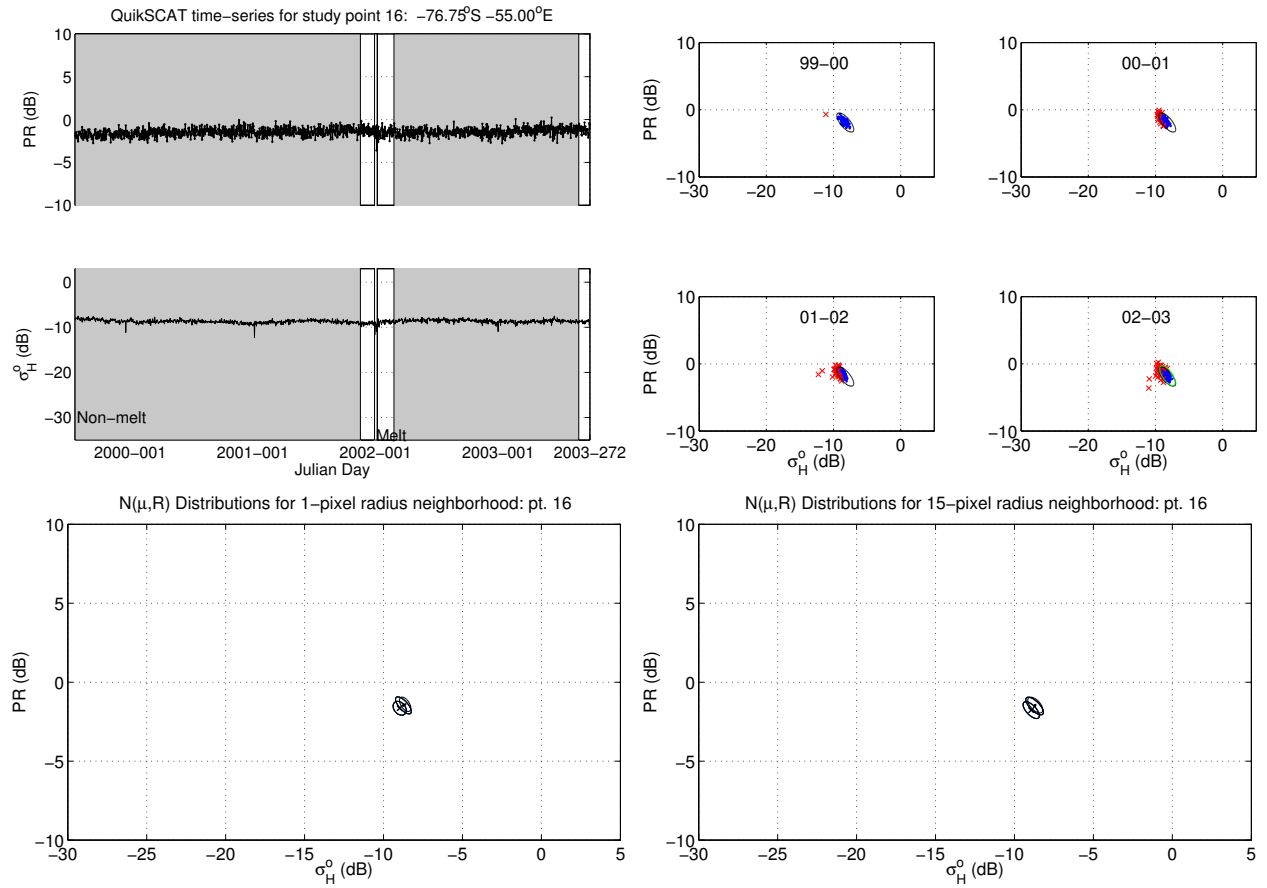
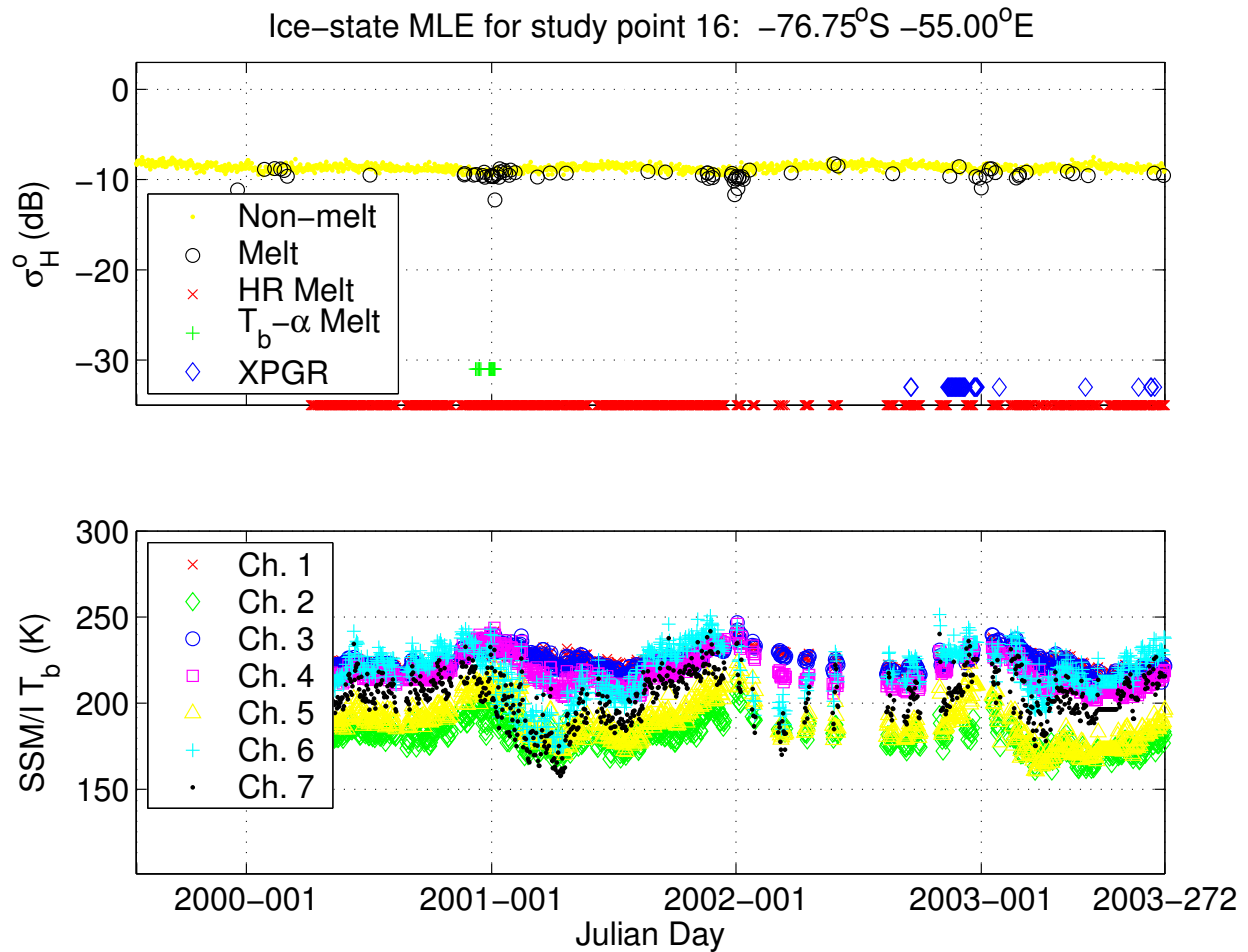Figure A.27: ML melt detection results for study point 14.

Figure A.28: Melt detection results for study point 14 from the ML method using QuikSCAT and the HR, T_b-α, and XPGR methods using SSM/I.

The XPGR method detects several false melt events for study point 14 while the ML method detects some realistic melt. The T_b-α results match the ML method except for a single point during 2002. The covariance and mean values for the melt season of point 12 are used.
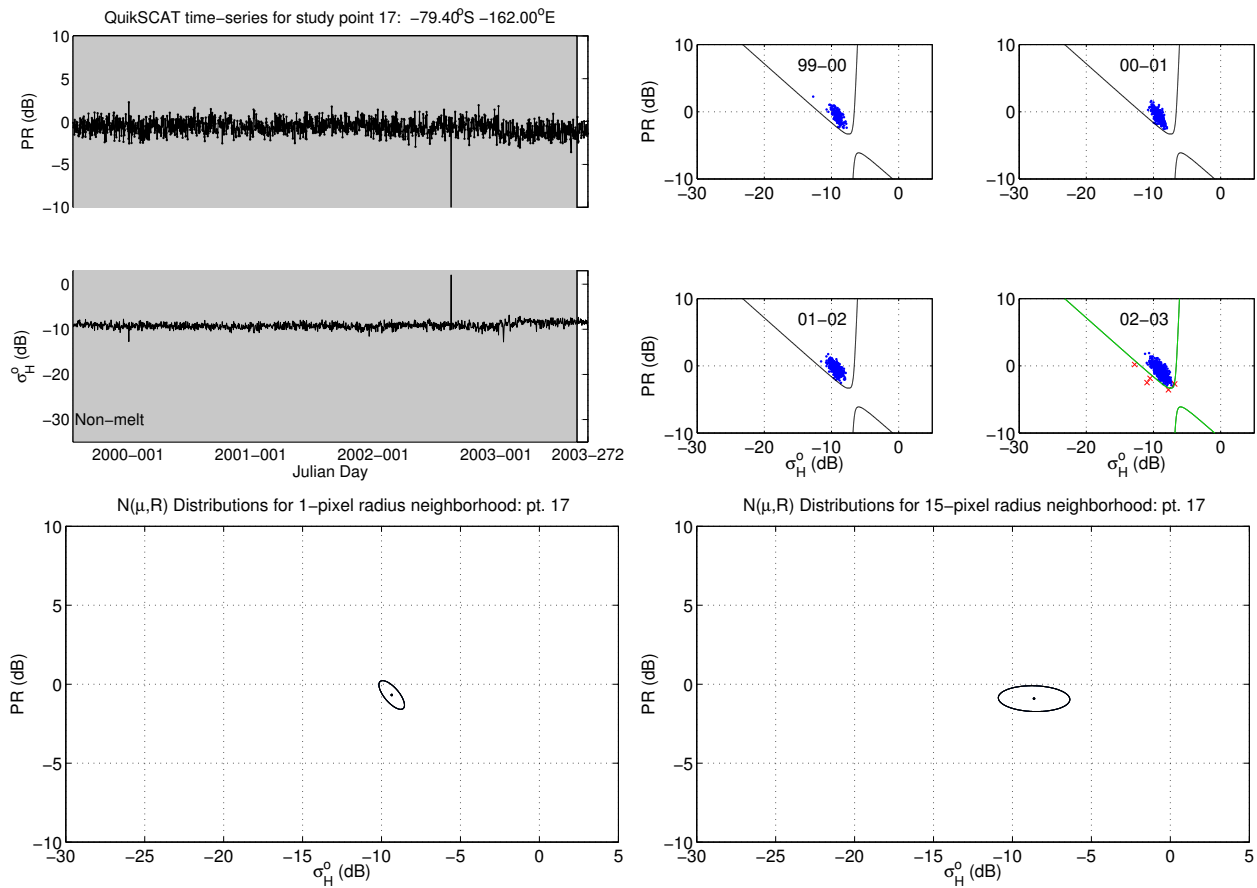
Figure A.29: ML melt detection results for study point 15.

Figure A.30: Melt detection results for study point 15 from the ML method using QuikSCAT and the HR, T_b-α, and XPGR methods using SSM/I.

For study point 15, the ML method identifies some melt days that are unrealistic while T_b-α properly classifies every day as non-melt. XPGR detects some melt in 2001-02 and 2002-03 although the brightness temperature values are well below 273K.

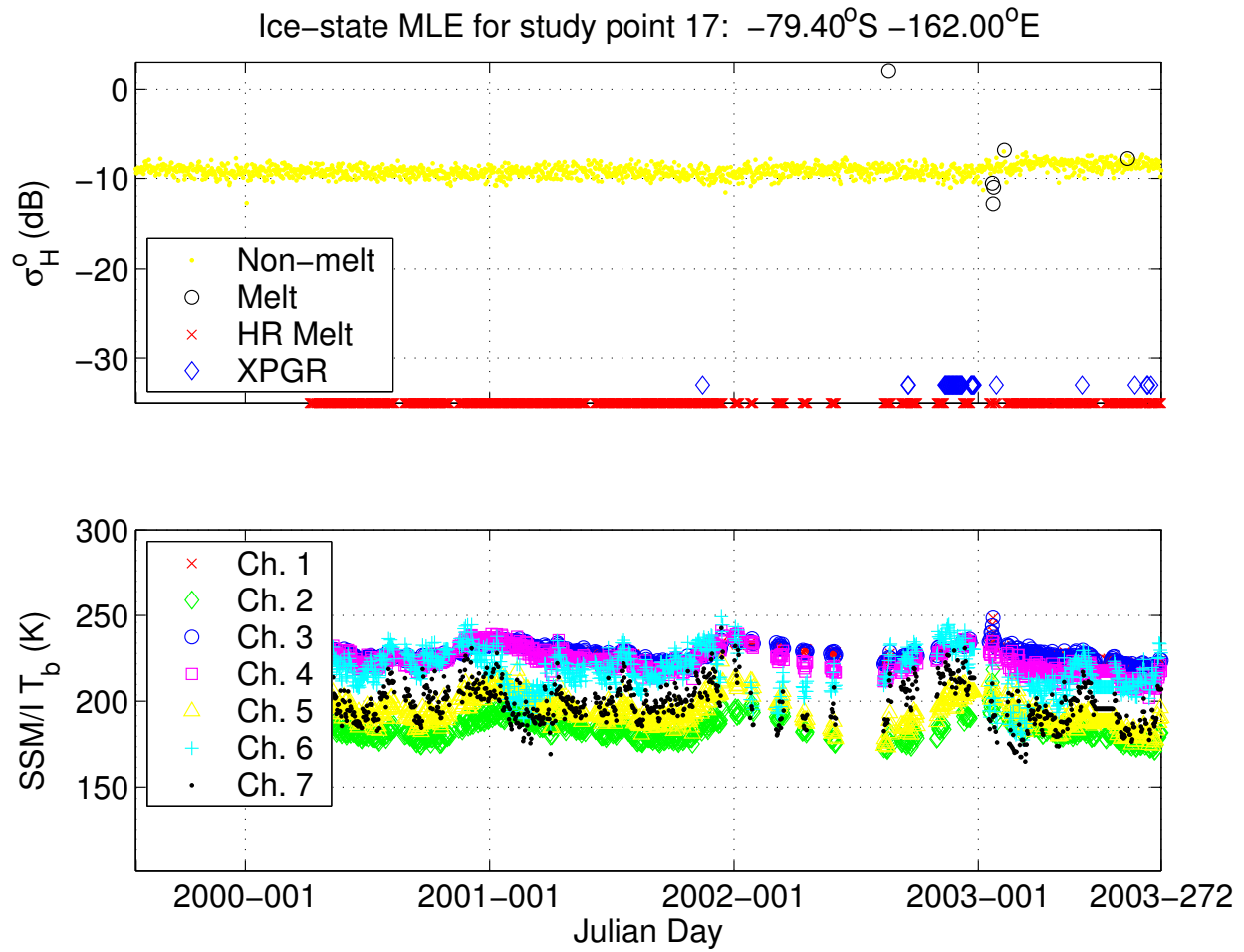Figure A.31: ML melt detection results for study point 16.

Figure A.32: Melt detection results for study point 16 from the ML method using QuikSCAT and the HR, T_b-α, and XPGR methods using SSM/I.

This study point results in poor performance from each of the melt detection methods since no prolonged melting occurs during any given summer. The ML method does detect melt during the summer months that correspond to melt classifications from the other methods; however, the ML method also identifies melt events during the winter months of each year. This is very unlikely to be the case.

Figure A.33: ML melt detection results for study point 17.

Figure A.34: Melt detection results for study point 17 from the ML method using QuikSCAT and the HR, T_b-α, and XPGR methods using SSM/I.

For study point 17, only a few melt events during the summer of 2002-03 are identified by the ML and XPGR algorithms. The ML method decision boundary for this case is a hyperbola, which may indicate when the method is expected to perform poorly.
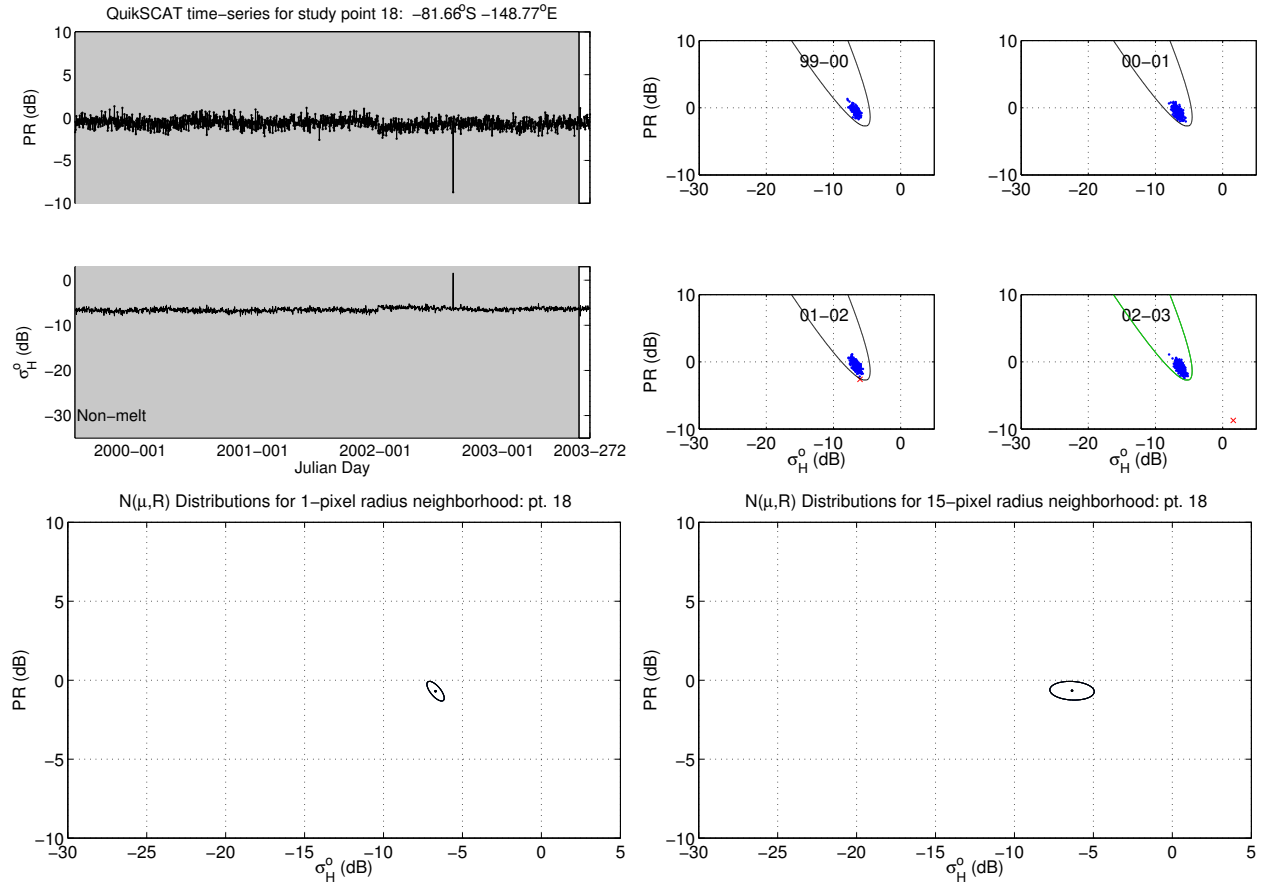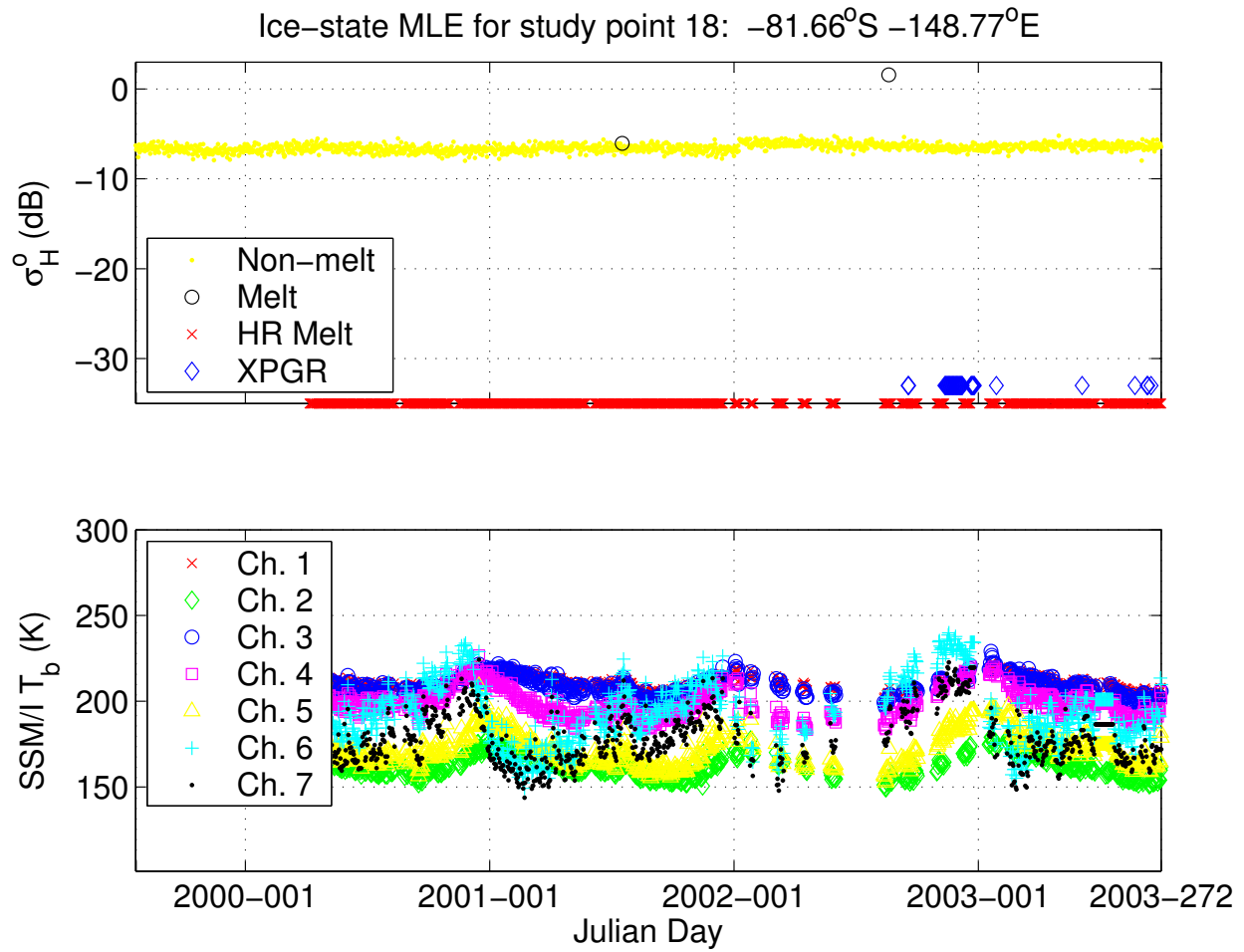
Figure A.35: ML melt detection results for study point 18.

Figure A.36: Melt detection results for study point 18 from the ML method using QuikSCAT and the HR, T_b-α, and XPGR methods using SSM/I.

The ML melt detection in 2001 corresponds to a sharp rise in the Channel 6 SSM/I time-series, but this is an unlikely melt event as it occurs during the winter months. The ML method melt event in 2002 is probably just a bad data value. This is most likely the case for points 12-15 and 17 as well.
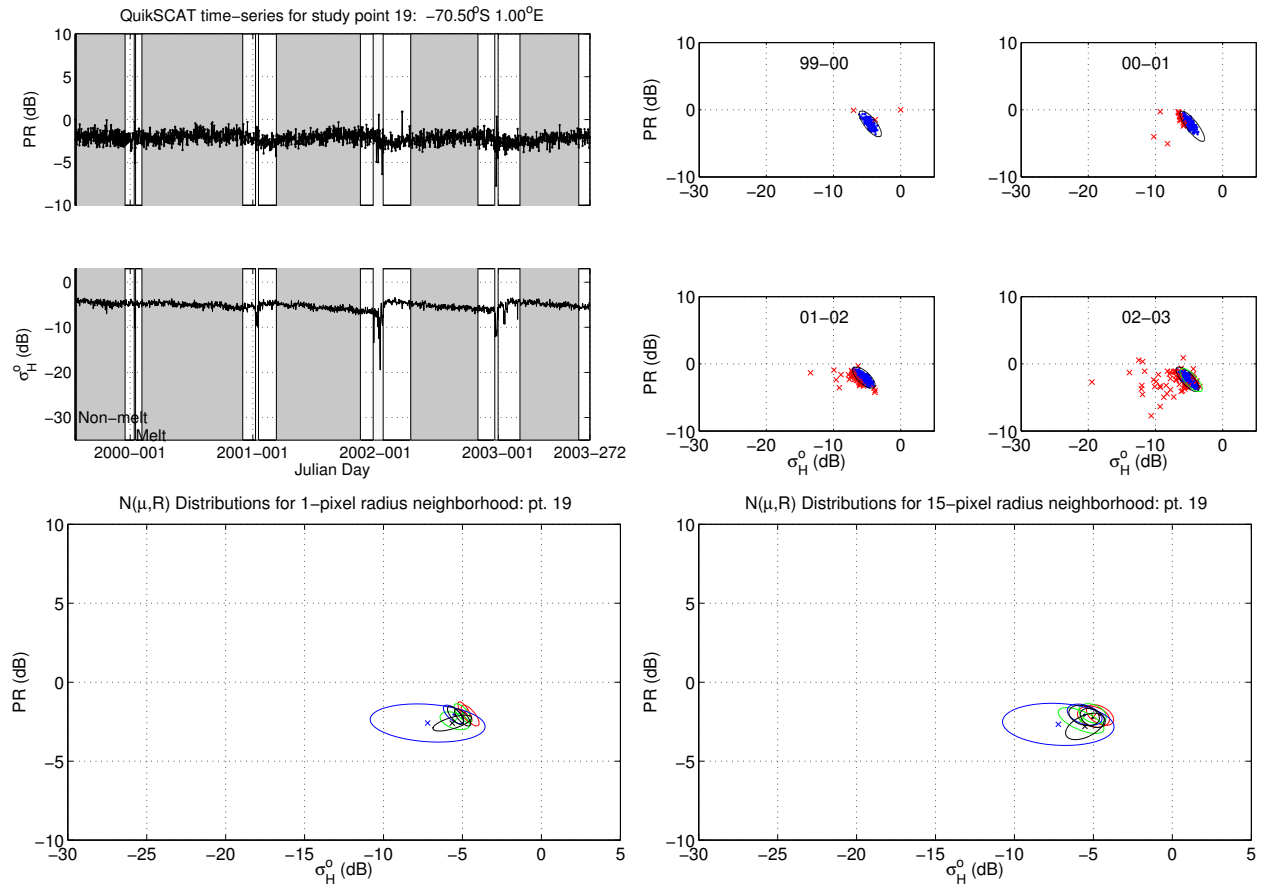
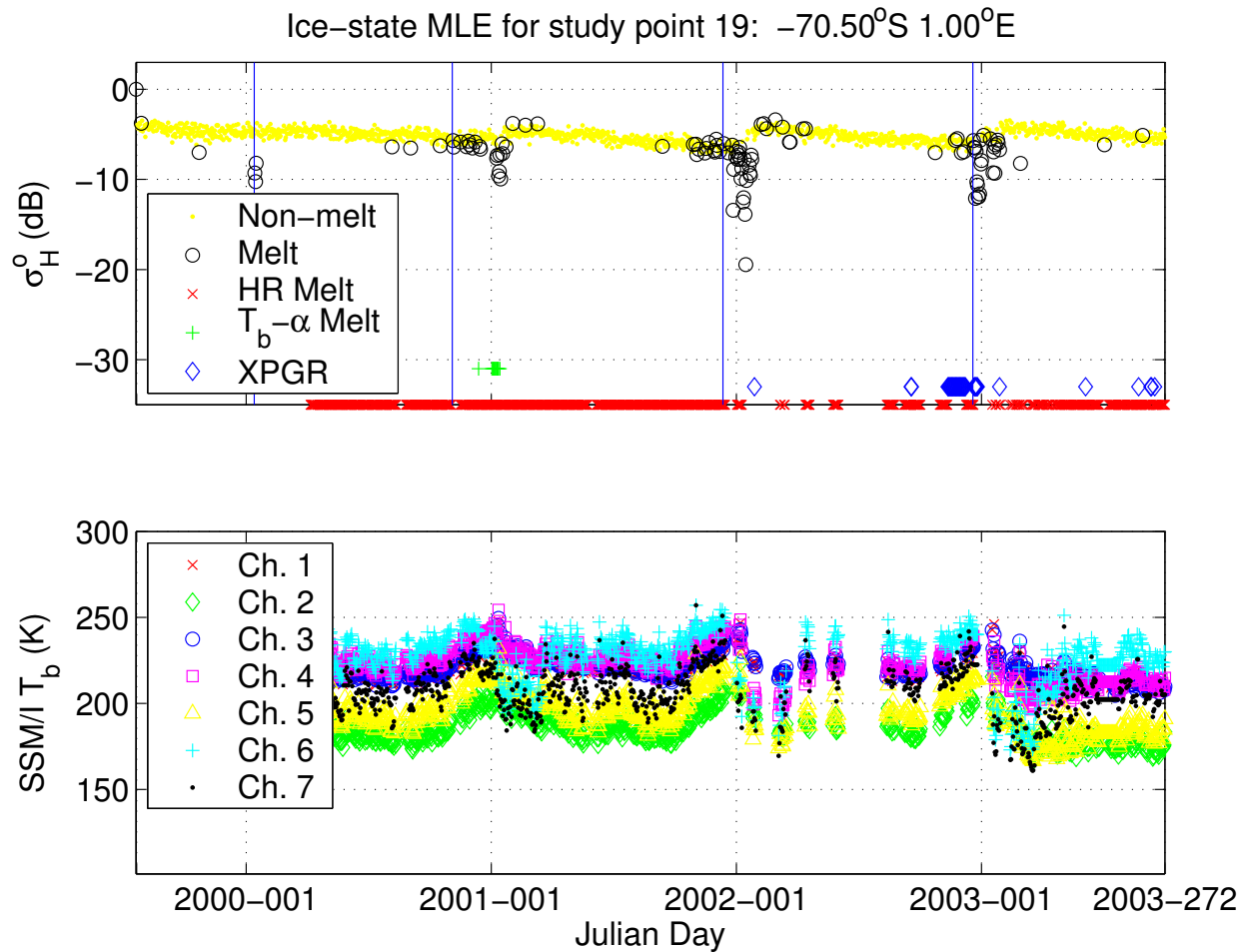Figure A.37: ML melt detection results for study point 19.

Figure A.38: Melt detection results for study point 19 from the ML method using QuikSCAT and the HR, T_b-α, and XPGR methods using SSM/I.

Analysis of study point 19 is presented in study point 19. It is worth noting that short melt periods lead to less reliable melt covariance and mean value estimates. This results in overlapping melt and non-melt backscatter distributions. Many correct melt events are detected; however, some melt is classified for backscatter values higher than the winter mean value. These anomalies are discussed in Chapter 3.
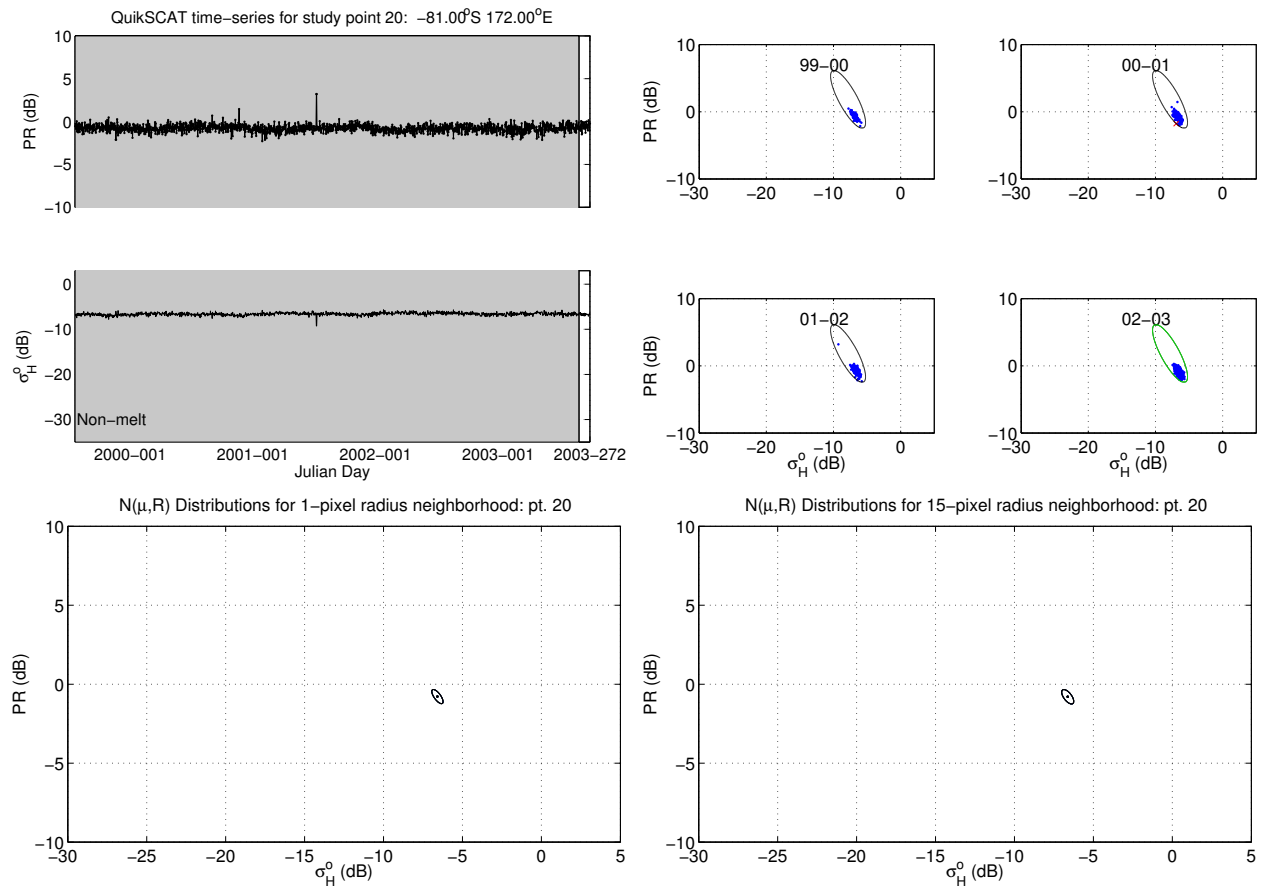
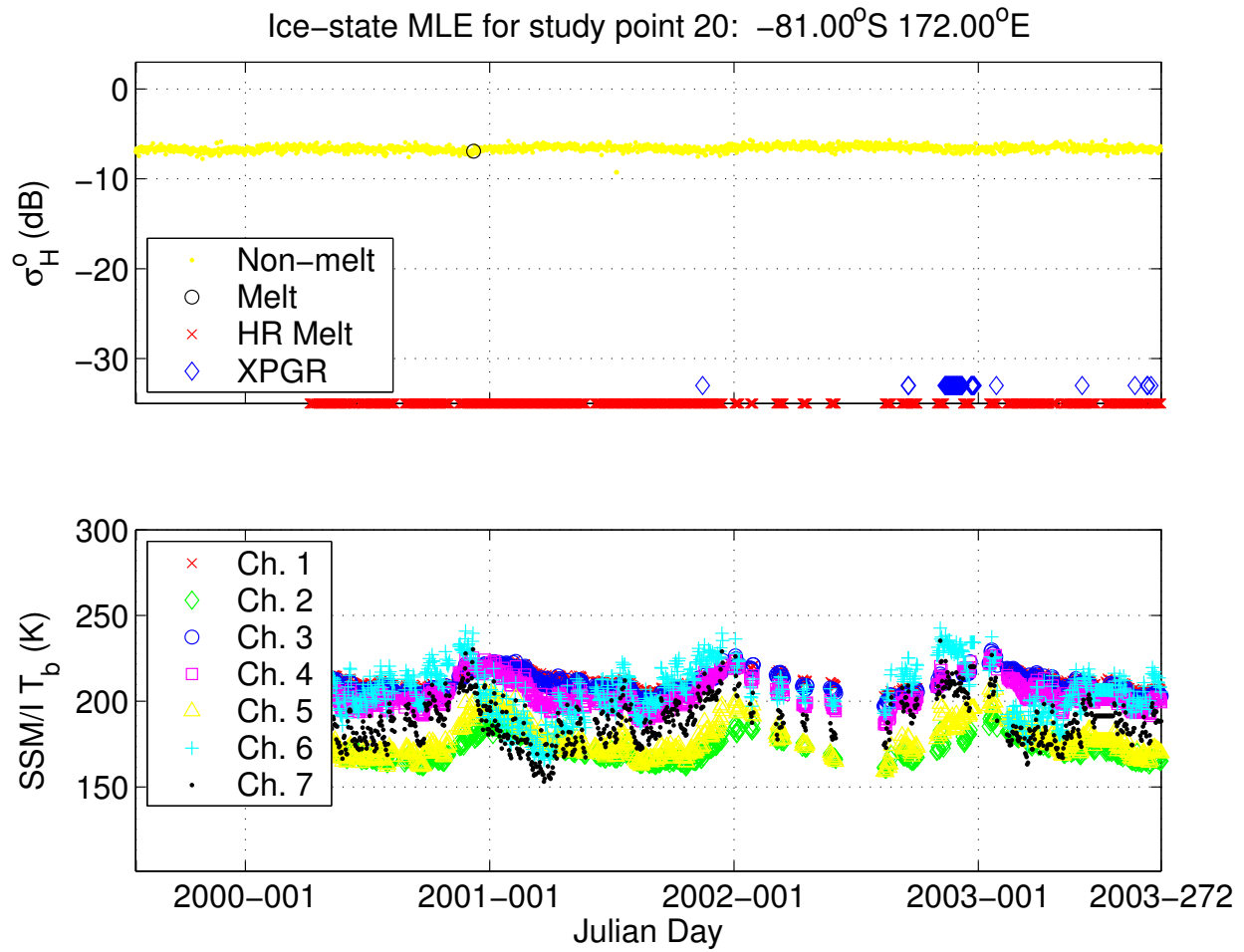Figure A.39: ML melt detection results for study point 20.

Figure A.40: Melt detection results for study point 20 from the ML method using QuikSCAT and the HR, T_b-α, and XPGR methods using SSM/I.

The SSM/I time-series for point 20 is similar to point 18, but the ML method does not mistakenly detect melt when the Channel 6 SSM/I values peak during 2001. The ML method classifies a single melt day in 2000 during the summer.
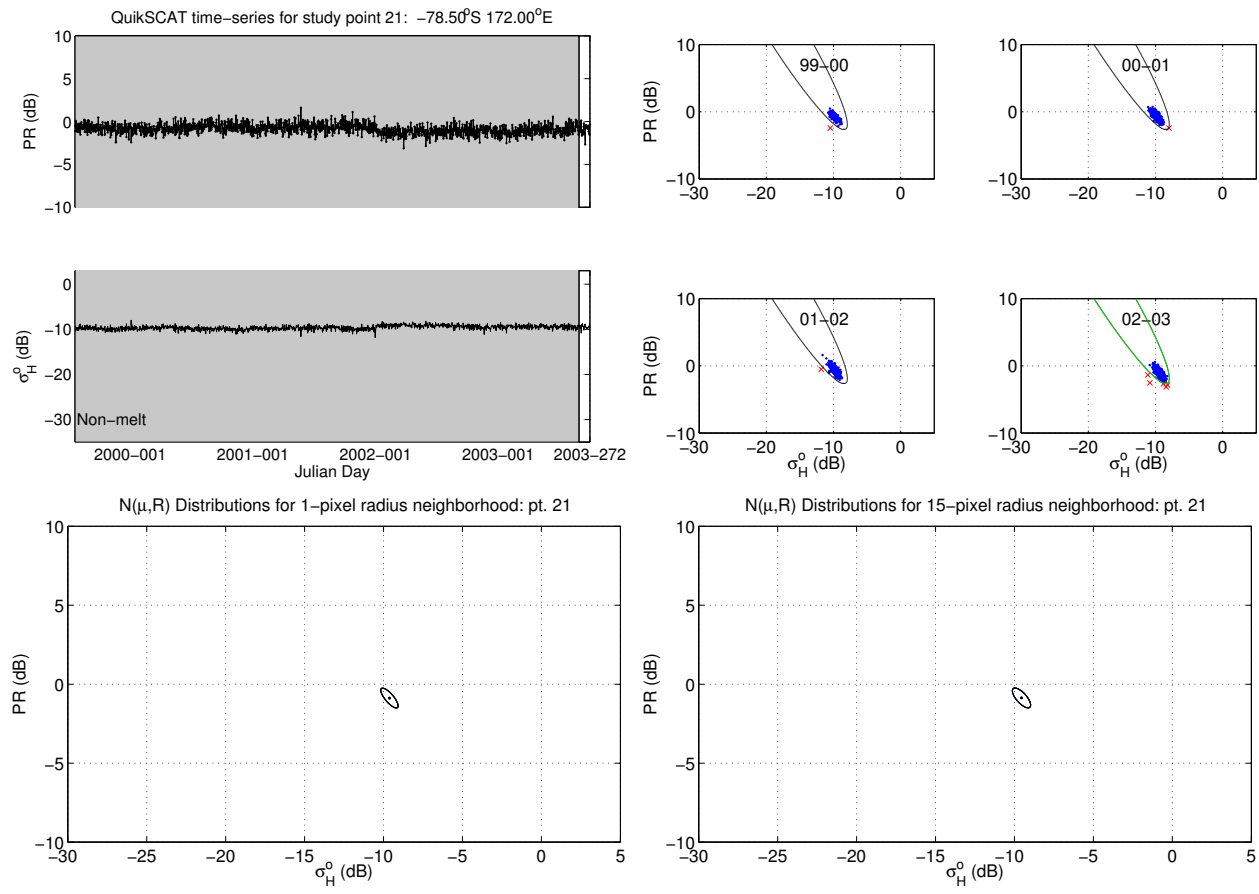
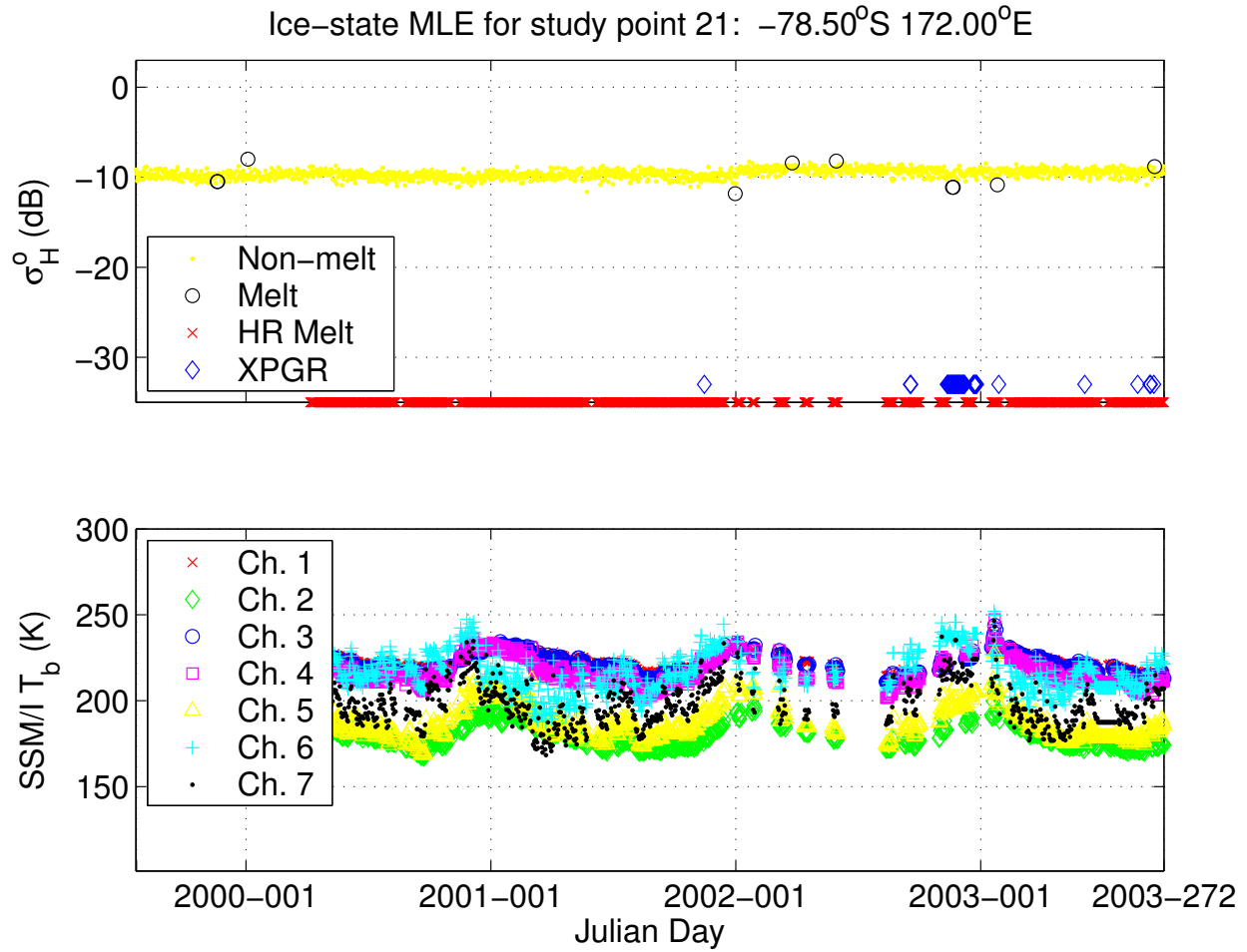Figure A.41: ML melt detection results for study point 21.

Figure A.42: Melt detection results for study point 21 from the ML method using QuikSCAT and the HR, T_b-α, and XPGR methods using SSM/I.

For this study point, the ML method uses the covariance and mean parameters for the melt season of point 12. Some potentially correct classifications are made during the 1999-00, 2001-02, and 2002-03 summers are made. It is like that the two melt classifications in the spring of 2002 are false. XPGR continues to overestimate melting during 2002-03.
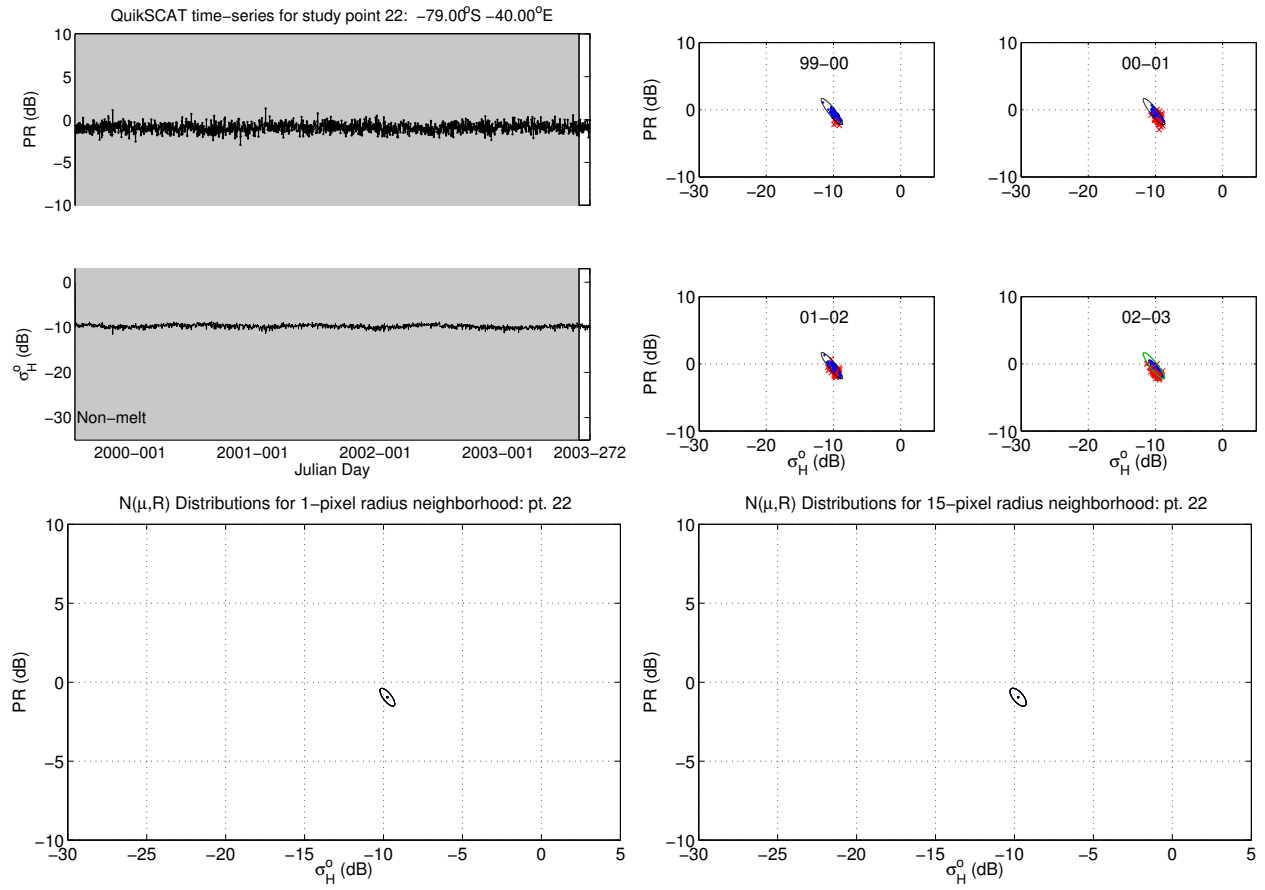
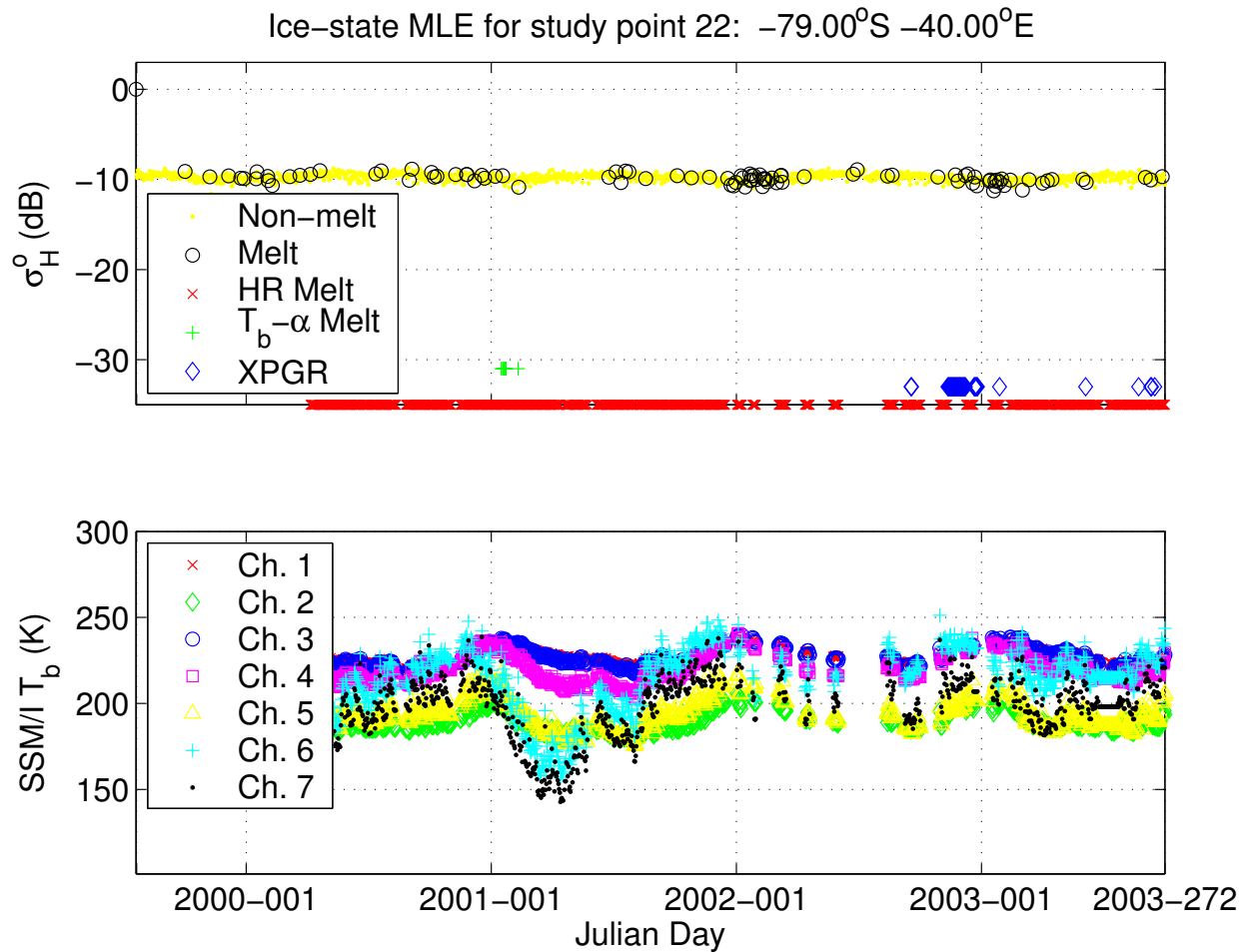Figure A.43: ML melt detection results for study point 22.

Figure A.44: Melt detection results for study point 22 from the ML method using QuikSCAT and the HR, T_b-α, and XPGR methods using SSM/I.

The melt-season covariance and mean parameters from study point 16 are used in the ML melt detection method for study point 22. Most of the ML melt classifications occur during the Austral summers but it is unlikely that actually melting takes place. T_b-α identifies some melt in 2000-01 while XPGR detects melt in 2002-03.

Figure A.45: ML melt detection results for study point 23.

Figure A.46: Melt detection results for study point 23 from the ML method using QuikSCAT and the HR, T_b-α, and XPGR methods using SSM/I.

The higher variance in the backscatter values for study point 23 leads to many false melt classifications by the ML method. The T_b observations by SSM/I are quite high and the T_b-α and XPGR methods observe melt in 2000-01 and 2002-03, respectively. These two SSM/I methods consistently detect melt during these same time periods for many of the study points.
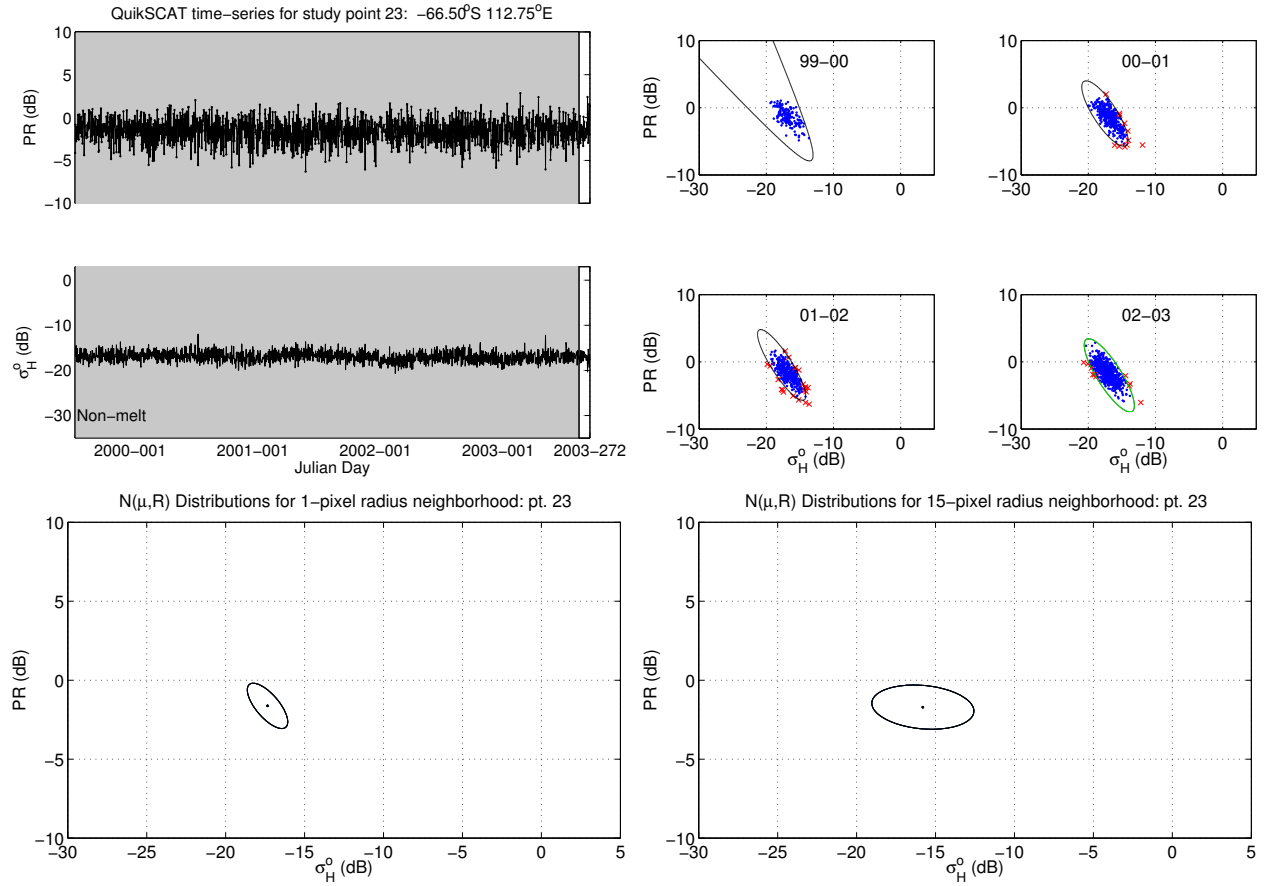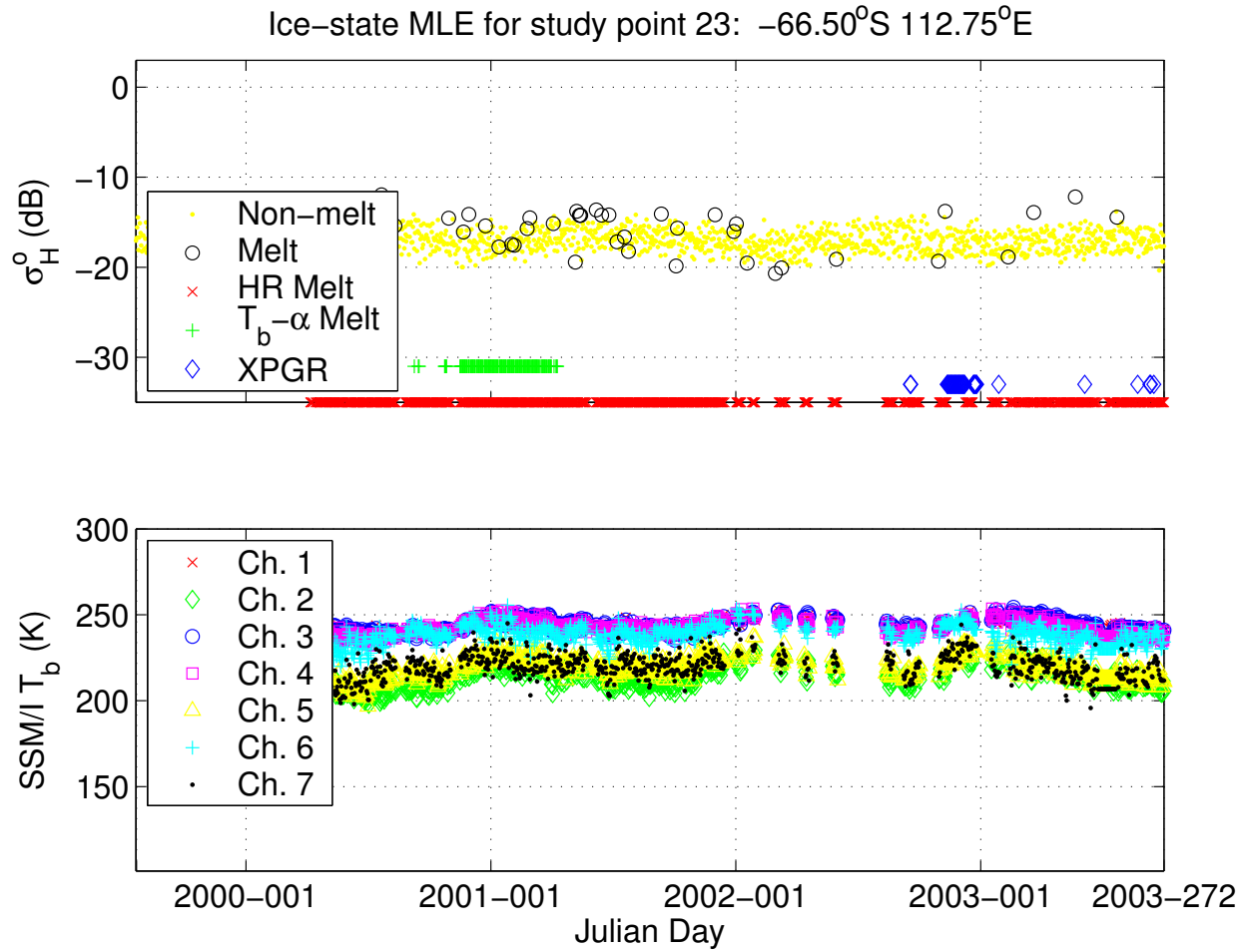
Figure A.47: ML melt detection results for study point 24.

Figure A.48: Melt detection results for study point 24 from the ML method using QuikSCAT and the HR, T_b-α, and XPGR methods using SSM/I.

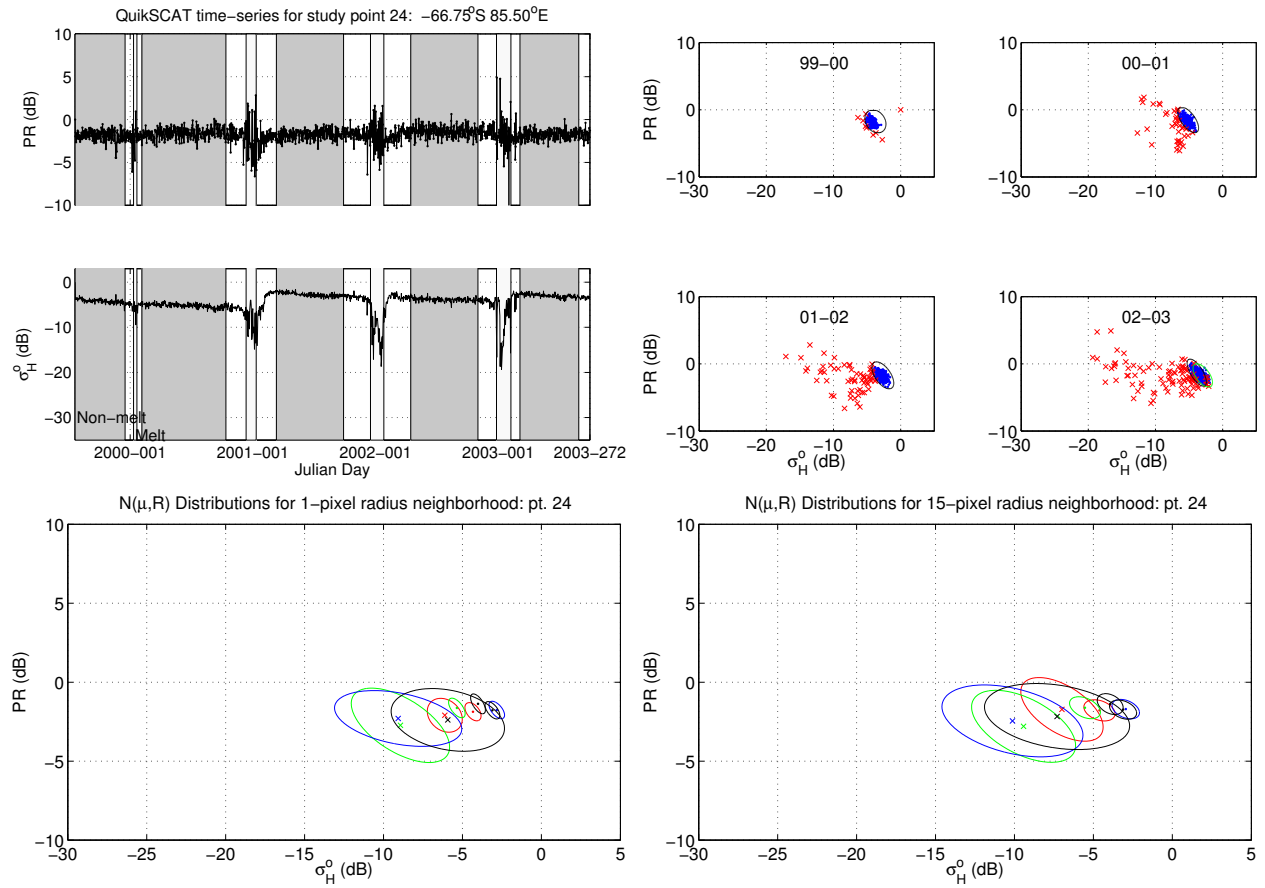The analysis for this study point is presented in Chapter 3.

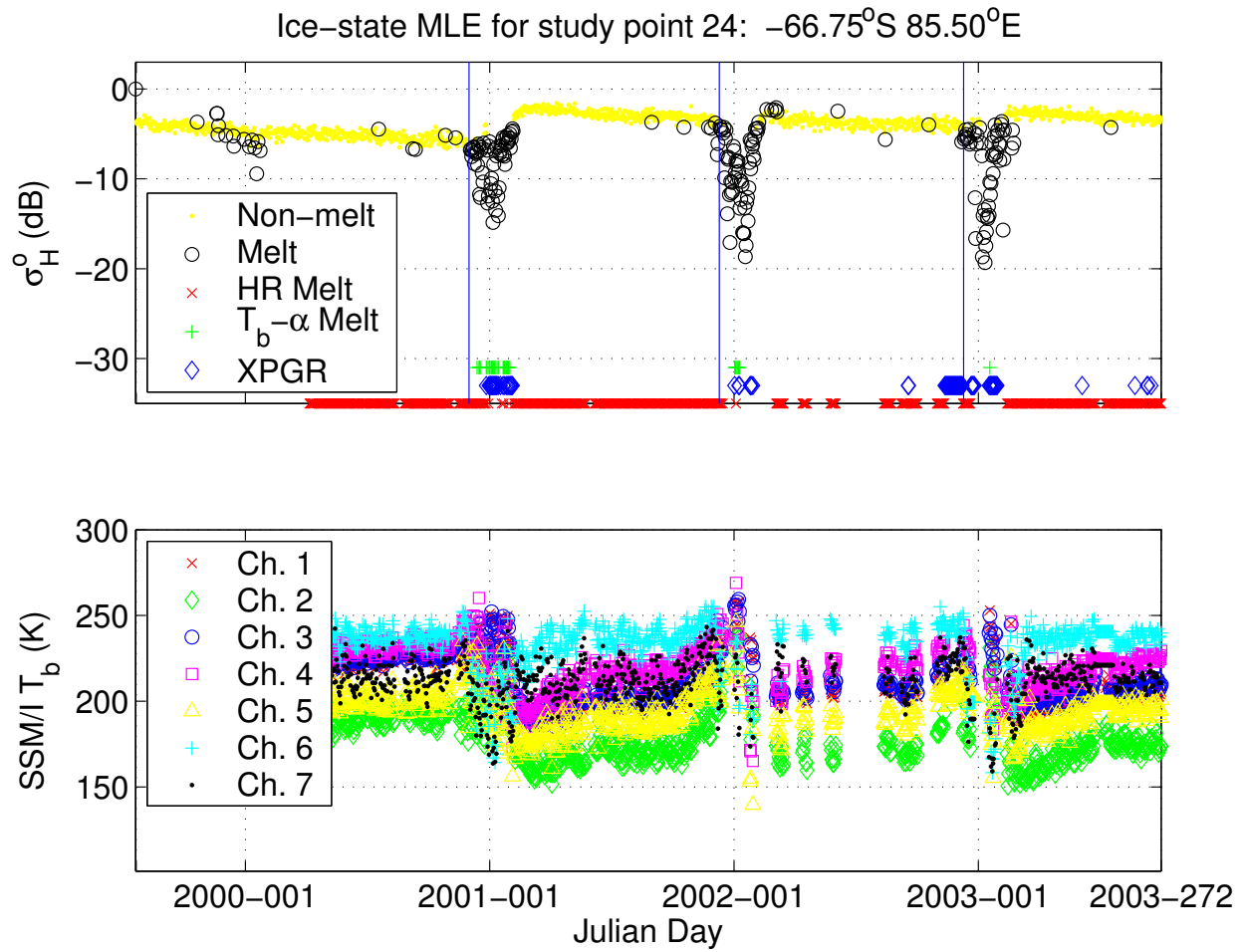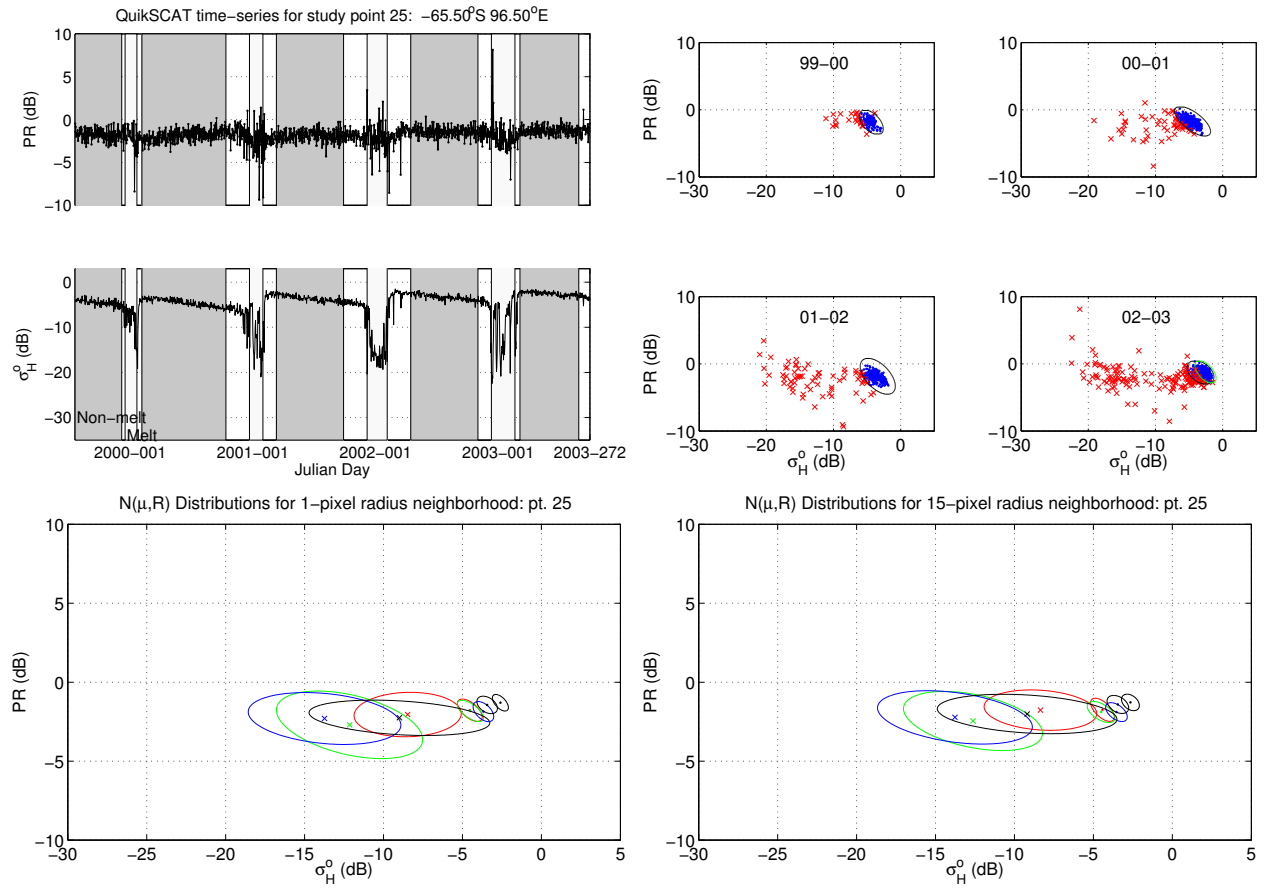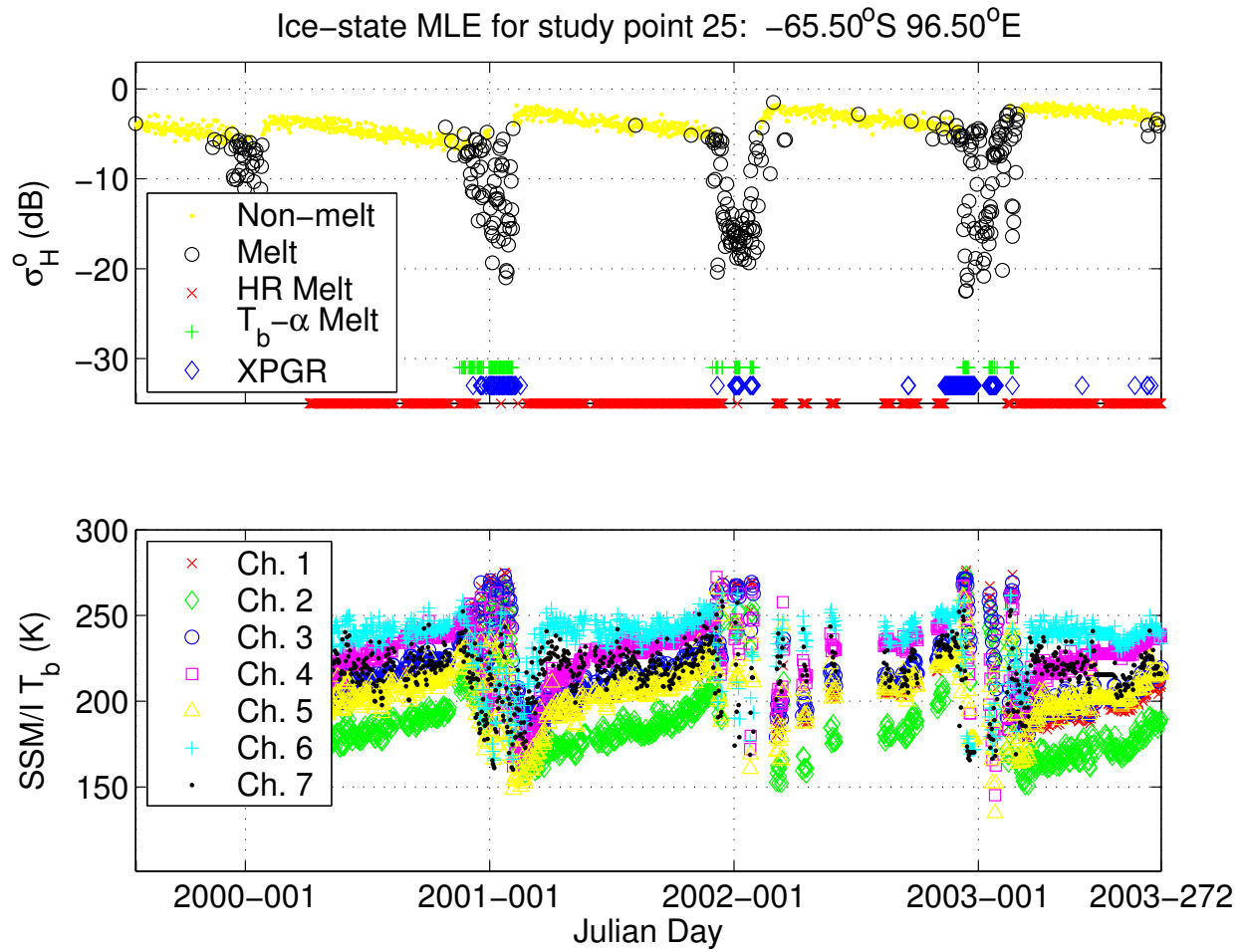Figure A.49: ML melt detection results for study point 25.

Figure A.50: Melt detection results for study point 25 from the ML method using QuikSCAT and the HR, T_b-α, and XPGR methods using SSM/I.

The melt detection results from all methods, except HR, match well for study point 25. Periods of reduced backscatter and increased brightness temperature are properly identified as melt events.

Appendix B

Additional Calibration Results

This appendix contains results from the calibration verification of selected areas of the Amazon rainforest (see Figure B.1). Regions 1 and 2 lie within the masked area used in Chapter 4. Region 3 is on the fringe of the masked region and contains terrain with a slightly less homogenous response than the other regions. Region 4 lies completely outside of the masked region. The analysis shows the importance of using homogenous targets when applying incidence-angle correction to backscatter measurements. These subregions are not suitable to use for corrections, whereas the masked Amazon and Sahara regions from Chapter 4 are adequately homogenous.
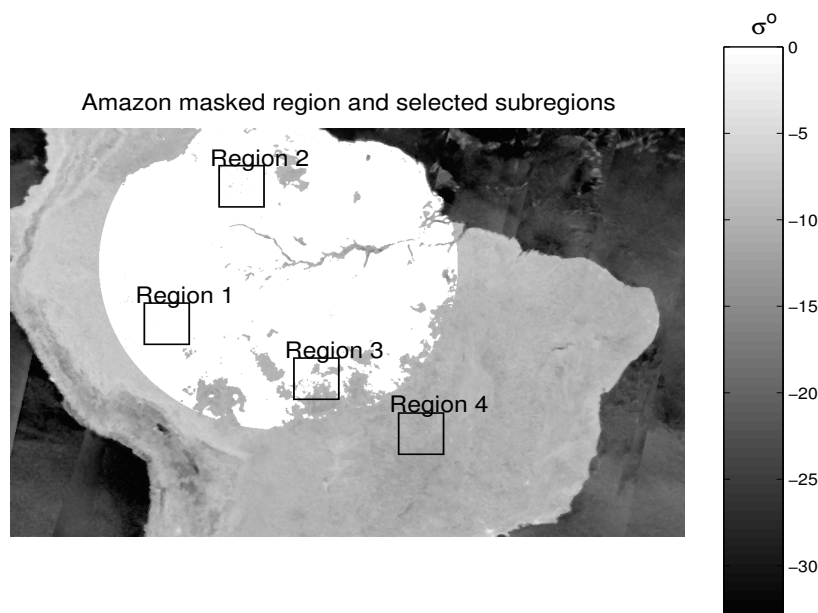

Figure B.1: The subregions analyzed for calibration verification. Each region is roughly 350km by 350km.

The standard deviation of the daily mean corrected backscatter for each subregion is generally much greater than for the masked region (see Table B.1 and Figure B.2). Region 4 exhibits the largest temporal variation in σ^o and region 3 displays the highest daily standard deviation (Table B.2). The backscatter standard deviation observed in region 4 also increases as the daily mean σ^o value decreases over time. This suggests that regions with higher mean backscatter values tend to be more temporally stable. The radar response for the masked region is nearly constant from day to day and the mean value is roughly 3 dB higher than in region 4. The higher standard deviation of daily σ^o values recorded in region 3 is expected since this area contains both locations included in and excluded from the stable masked region.

Table B.1: The correction results for each subregion. Only 'v'-pol slice values are presented as results from 'h'-pol and egg resolution data are similar. The standard deviation of the daily mean σ^o is given for both uncorrected and incidence-angle corrected values. These values are computed in log space. QuikScat is denoted as QS and SeaWinds as SW. In each data column the uncorrected results are given first and the corrected are shown after the slash "/".

Sensor	Pass	Region 1 uncorr./corr.	Region 2 uncorr./corr.	Region 3 uncorr./corr.	Region4 uncorr./corr.
QS	ascending	0.255 / 0.234	0.144 / 0.138	0.278 / 0.263	0.304 / 0.304
	descending	0.062 / 0.074	0.041 / 0.062	0.083 / 0.096	0.165 / 0.166
SW	ascending	0.185 / 0.201	0.099 / 0.123	0.199 / 0.213	0.226 / 0.221
	descending	0.093 / 0.088	0.047 / 0.059	0.121 / 0.126	0.256 / 0.250

Table B.2: The mean daily standard deviation of σ^o for each subregion.

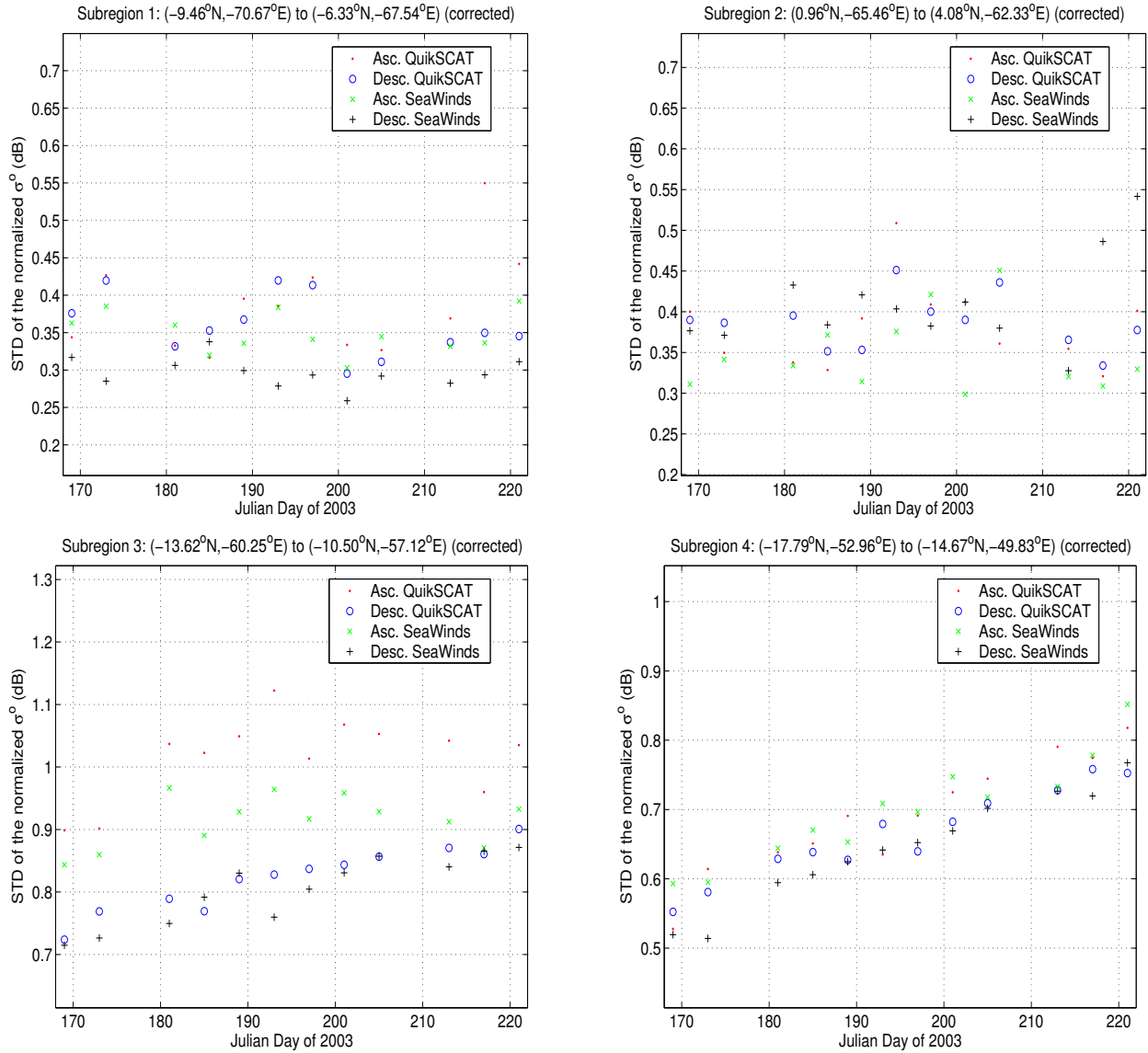| Sensor	Pass	Region 1 uncorr./corr.	Region 2 uncorr./corr.	Region 3 uncorr./corr.	Region4 uncorr./corr.
QS	ascending	0.375 / 0.387	0.373 / 0.381	1.016 / 1.017	0.692 / 0.692
	descending	0.344 / 0.360	0.377 / 0.386	0.822 / 0.822	0.665 / 0.665
SW	ascending	0.338 / 0.350	0.342 / 0.348	0.914 / 0.914	0.699 / 0.699
	descending	0.309 / 0.296	0.390 / 0.410	0.797 / 0.804	0.645 / 0.645

Figure B.2: Standard deviation time-series of corrected 'v'-pol slice values for 2003 JD 169-221 in subregions 1 (upper left), 2 (upper right), 3 (lower left), and 4 (lower right). The latitude and longitude of each subregion is given in the title of each regions respective plot.

A polarization bias is present in the uncorrected data for the masked region and each of the subregions, with values measured from 'h'-pol about 1.5 dB higher than for 'v'-pol (Figures B.3-B.4). Region 3 is the least homogenous and shows less bias relating to the diurnal cycle but still exhibits polarization dependence of σ^o. All of the observations discussed in this section apply to both "egg" and "slice" resolution SIR-format data images used in the correction method.

Figure B.3: Mean σ^o time-series of uncorrected 'h'-pol (left column) and 'v'-pol (right column) slice values for 2003 JD 169-221 in regions 1 (top row) and 2 (bottom row).

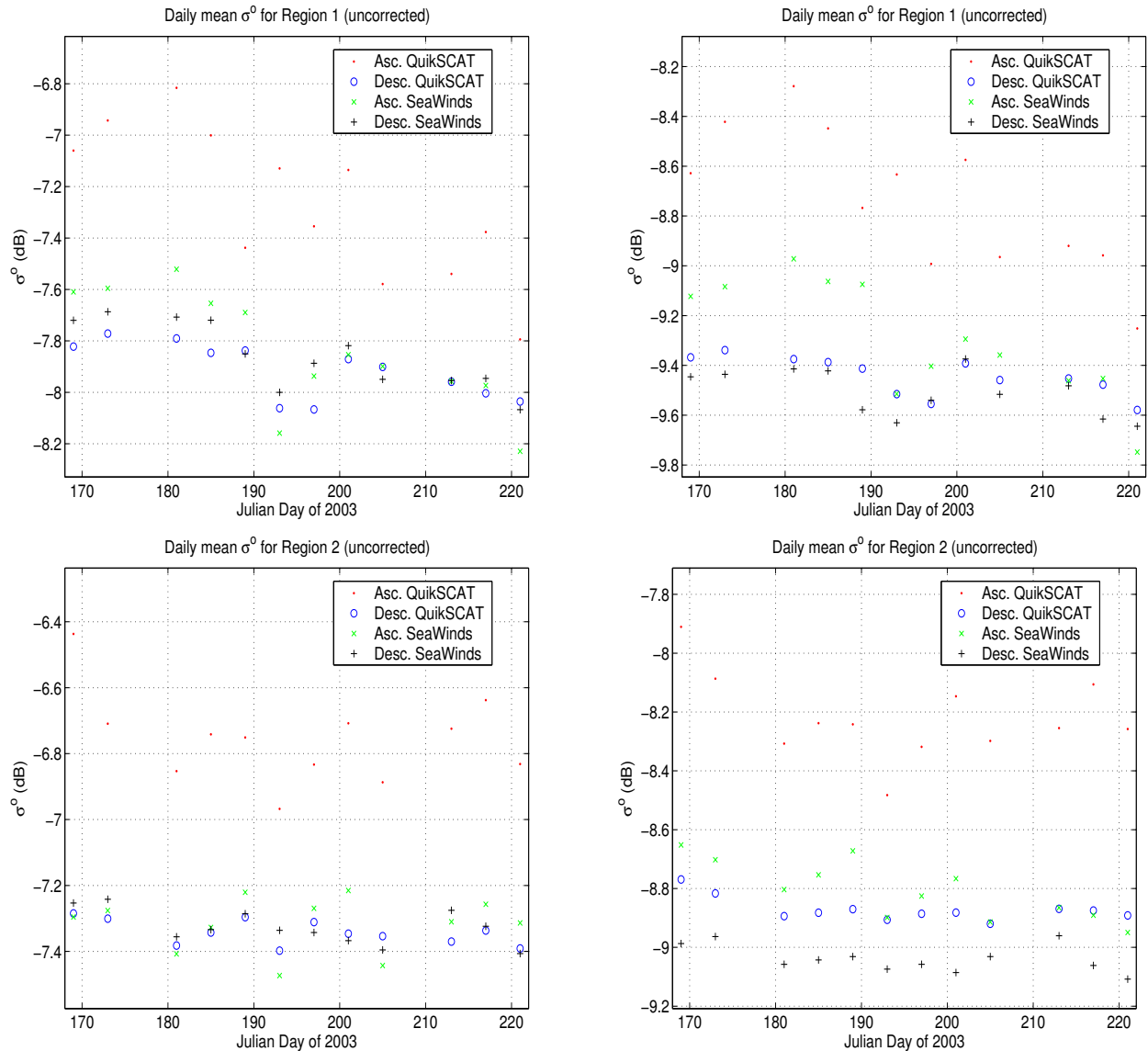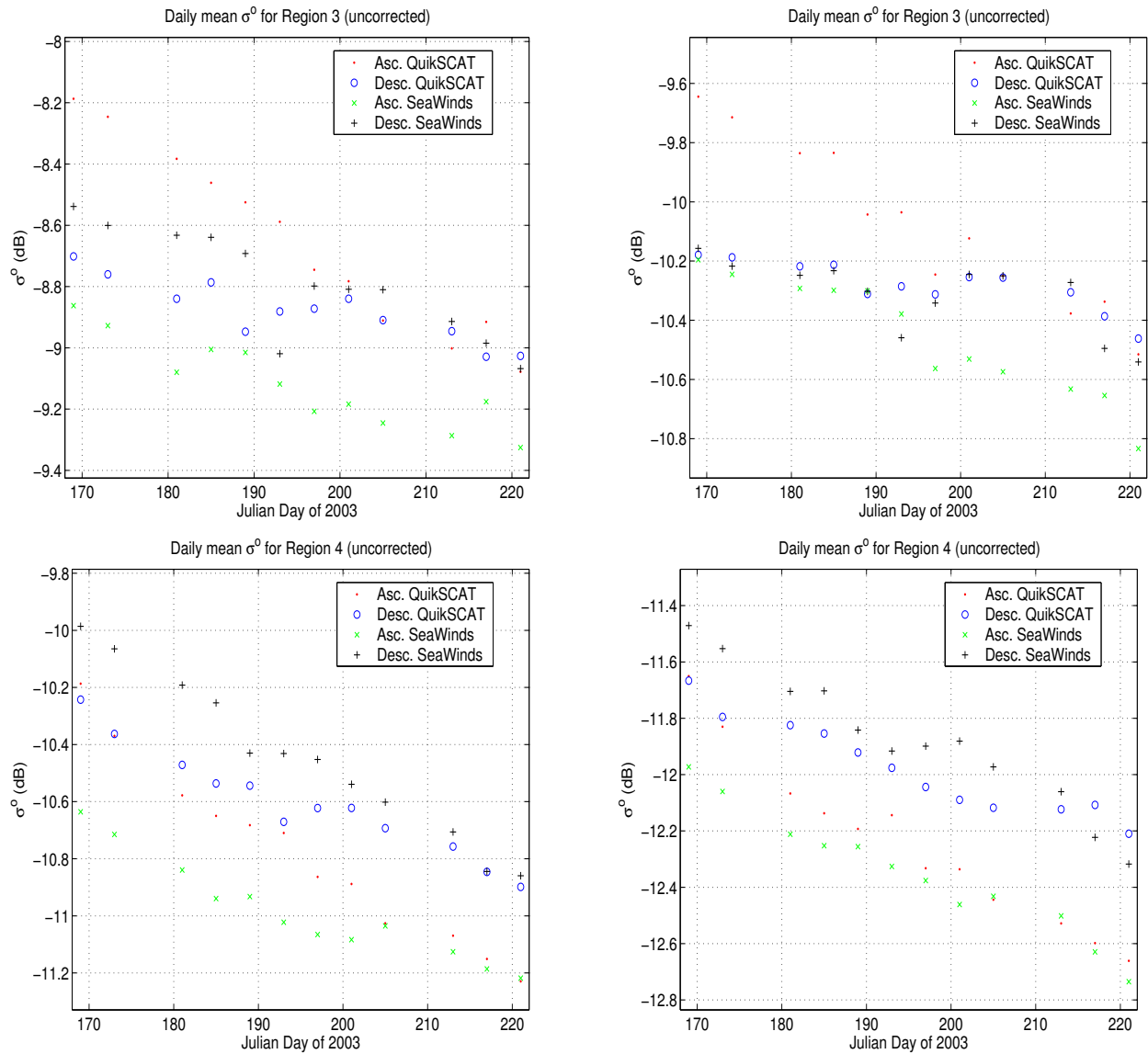Figure B.4: Mean backscatter time-series of uncorrected 'h'-pol (left column) and 'v'-pol (right column) slice values for 2003 JD 169-221 in subregions 3 (top row) and 4 (bottom row).

Figure B.5 contains scatterplots of σ^o vs. incidence angle (θ_i) for each of the subregions. The linear least-squares fit to the data shows a larger variation with incidence angle in the subregions than for the masked region (see also Table B.3). This is due to the difference in relative size of the regions as well as the increased variability of the daily σ^o values for the subregions. Similar to the Amazon masked region used in Chapter 4, the B values for the 'v'-pol backscatter are generally higher than for the 'h'-pol.

In general, using spatially masked regions to correct for the incidence-angle dependence in the backscatter measurements appears to be much better than using smaller subregions. Care must be taken to ensure that the calibration reference region is suitably homogenous and temporally stable in order to verify the cross-calibration of scatterometers.

Table B.3: The incidence angle dependence coefficients (B in dB/degree) for each region's respective polarization and resolution calculated from all passes of both sensors. 'h'-pol measurements are normalized to an incidence angle of 46° and 'v'-pol to 54°.

Polarization	Resolution	Region 1	Region 2	Region 3	Region 4
horizontal	slice	0.7297	0.3185	0.5987	0.3595
	egg	0.2880	2.7227	2.4910	0.3362
vertical	slice	1.4715	1.3470	0.8613	0.0233
	egg	3.8244	3.7907	3.4476	0.6117

For completeness, the daily mean and standard deviation time-series for the Sahara desert region using "egg" resolution 'v'-pol and 'h'-pol images are also presented (Figures B.6 and B.7). Note that there are no significant differences from the "slice" observations presented in Chapter 4.
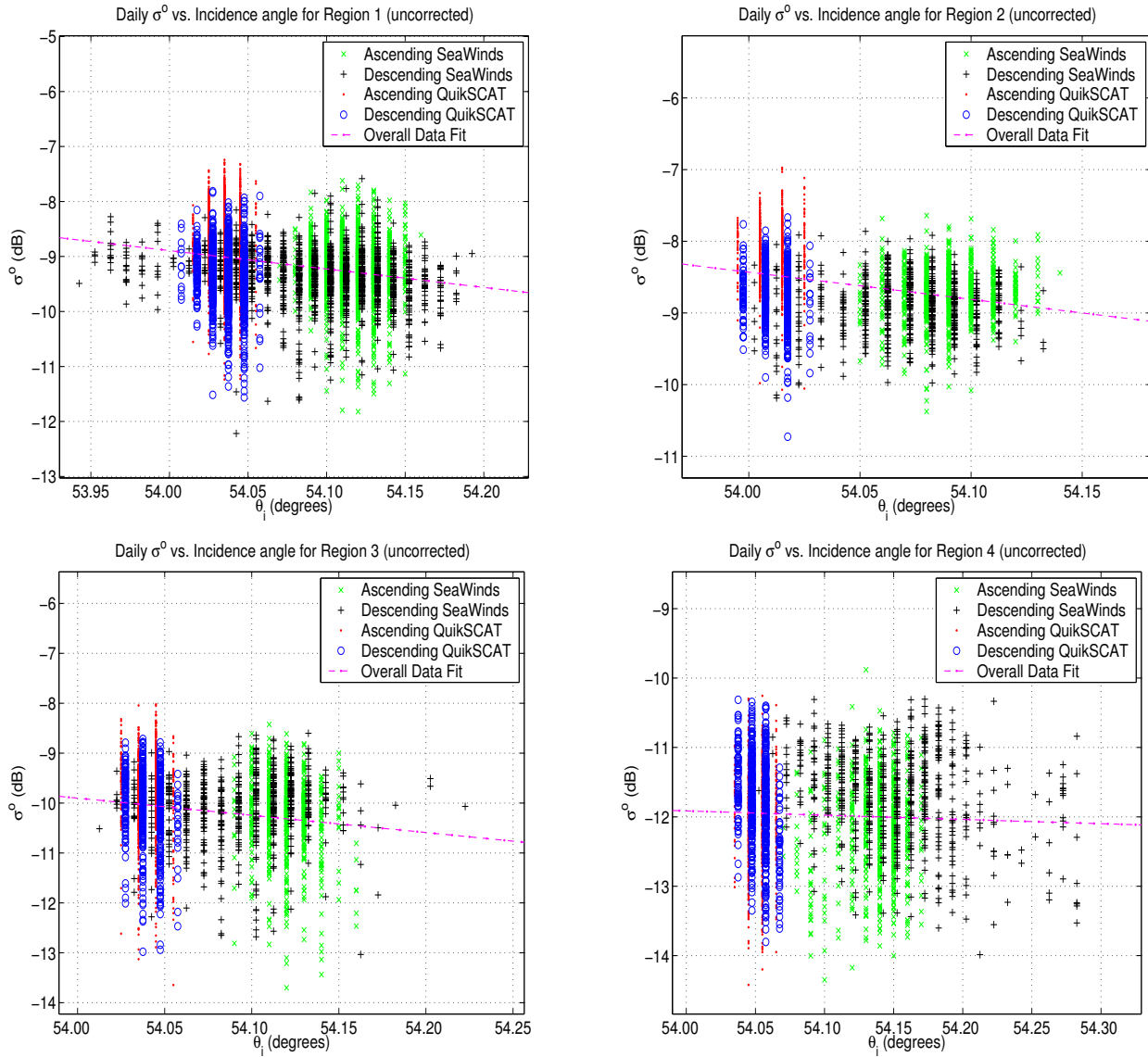
Figure B.5: Plots of σ^o vs. θ_i for uncorrected 'v'-pol "egg" data from subregions 1 (upper left), 2 (upper right), 3 (lower left), and 4 (lower right). The B values are much larger in magnitude for these regions than the masked Amazon region of Chapter 4 (Table B.3).
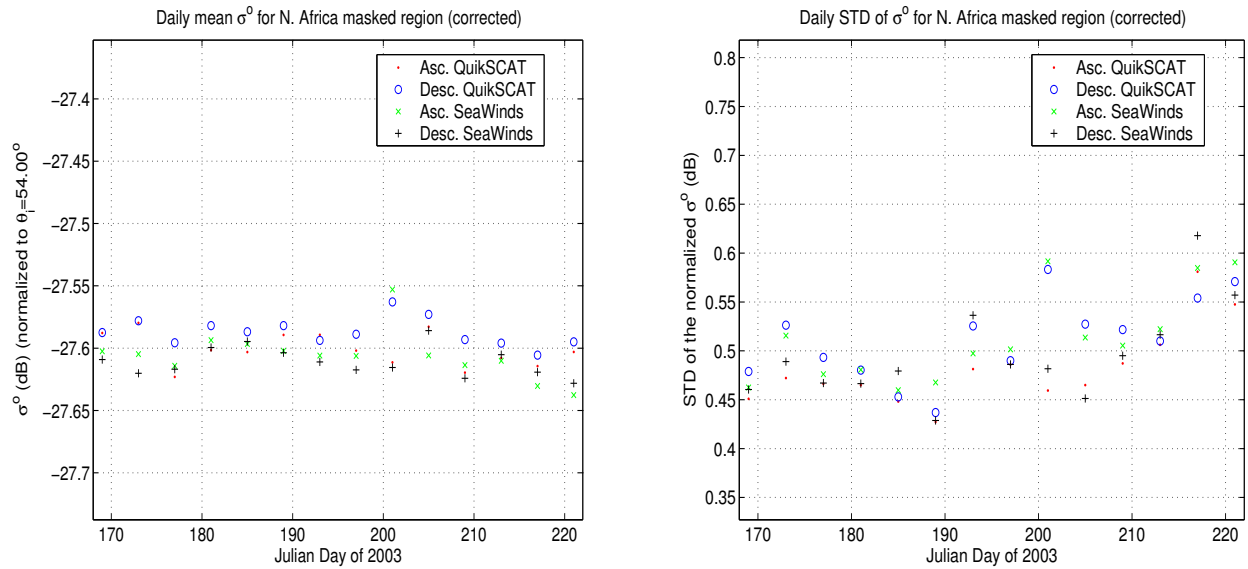
Figure B.6: Mean (left) and standard deviation (right) time-series of corrected 'v'-pol egg values for 2003 JD 169-221 in Sahara. 'v'-pol slice results are given in Chapter 4.
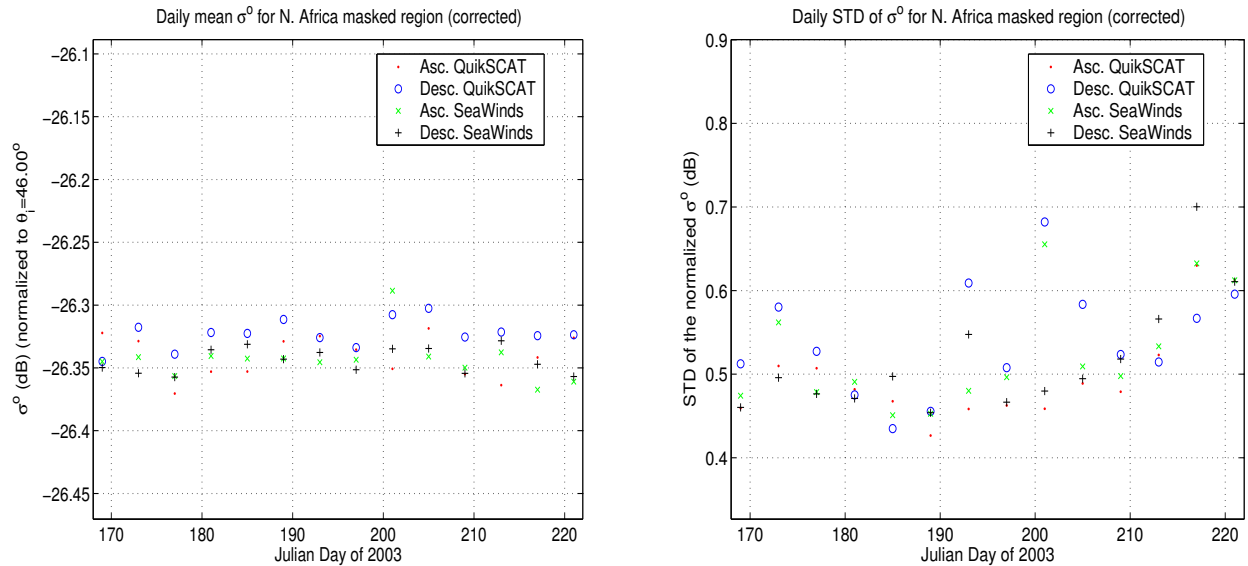

Figure B.7: Mean (left) and standard deviation (right) time-series for corrected 'h'-pol egg values for 2003 JD 169-221 in Sahara.

Bibliography

[1] W. J. Campbell, P. Gloersen, and H. J. Zwally, "Aspects of Arctic sea ice observable by sequential passive-microwave observations from the Nimbus 5 satellite", in *Arctic Technology and Policy*, I. Dyer and C. Chryssostomidis, Eds., pp. 197–222. Hemisphere Publishing, New York, 1984.

[2] M. R. Anderson, "The onset of spring melt in first-year ice regions of the Arctic as determined from SMMR data for 1979 and 1980", *Journal of Geophysical Research*, vol. 92(C12): 13,153-13,163, 1987.

[3] K. Garrity, "Characterization of snow on floating ice and case studies of brightness temperature change during the onset of melt", in *Microwave remote sensing of sea ice*, F.D. Carsey and 7 others, Eds., 68, pp. 313–328. American Geophysical Union, Washington, D.C., 1992.

[4] R. R. Forster, D. G. Long, K. C. Jezek, S. D. Drobot, and M. R. Anderson, "The onset of Arctic sea-ice snowmelt as detected with passive- and active-microwave remote sensing", *Annals of Glaciology*, vol. 33, pp. 85–93, 2001.

[5] M. R. Drinkwater and X. Liu, "Seasonal to interannual variability in Antarctic sea-ice surface melt", *IEEE Trans. Geosci. Remote Sensing*, vol. 38, no. 4, pp. 1827–1842, July 2000.

[6] T. A. Scambos, C. Hulbe, M. Fahnestock, and J. Bohlander, "The link between climate warming and break-up of ice shelves in the Antarctic Peninsula", *Journal of Glaciology*, vol. 46, no. 154, 2000.

[7] J. Zec, D. G. Long, and W. L. Jones, "NSCAT normalized radar backscattering coefficient biases using homogenous land targets", *Journal of Geophysical Research*, vol. 104, no. C5, pp. 11557–11568, May 1999.

[8] S. Dunbar et al, *QuikSCAT Science Data Product User's Manual, version 1.1*, Number D-18053. October 1999.

[9] B. R. Mahafza, *Radar Systems Analysis and Design Using MATLAB*, Chapman and Hall CRC, Baton Raton, FL, 2000.

[10] F. D. Carsey, *Microwave Remote Sensing of Sea Ice*, American Geophysical Union, Washington, D.C., 1992.

[11] F. T. Ulaby, R. K. Moore, and A. K. Fung, *Microwave remote sensing, active and passive. Vol. 2. Radar remote sensing and surface scattering and emission theory*, Addison-Wesley Publishing Co., Reading, MA, 1982.

[12] F. T. Ulaby, R. K. Moore, and A. K. Fung, *Microwave Remote Sensing Active and Passive*, vol. 1, Artech House, 1981.

[13] W. Abdalati and K. Steffen, "Greenland ice sheet melt extent: 1979-1999", *Journal of Geophysical Research*, vol. 106, no. D24, pp. 33983–33988, December 2001.

[14] I. S. Ashcraft and D. G. Long, "Comparison of methods for melt detection over Greenland using active and passive microwave measurements", *IEEE Trans. Geosci. Remote Sensing*, 2004, in review.

[15] D. G. Long and D. Daum, "Spatial resolution enhancement of SSM/I data", *IEEE Trans. Geosci. Remote Sensing*, vol. 36, pp. 407–417, 1997.

[16] "Scatterometer Climate Record Pathfinder", http://www.scp.byu.edu/, 2004.

[17] T. K. Moon and W. C. Stirling, *Mathematical methods and algorithms for Signal Processing*, Prentice Hall, Upper Saddle River, NJ, 2000.

[18] D. P. Winebrenner, D. G. Long, and B. Holt, "Mapping the progression of melt onset and freeze-up on arctic sea ice using SAR and scatterometry", in *Recent advances in the analysis of SAR data of the Polar Oceans*, C. Tsatsoulis and R. Kwok, Eds., pp. 129–144. Springer-Verlag, Berlin, Germany, 1998.

[19] D. G. Vaughan and C. S. M. Doake, "Recent atmospheric warming and retreat of ice shelves on the Antarctic Peninsula", *Nature*, vol. 379, no. 6563, pp. 328–331, 1996.

[20] D. G. Long and G. B. Skouson, "Calibration of spaceborne scatterometers using tropical rain forests", *IEEE Trans. Geosci. Remote Sensing*, vol. 34, no. 2, pp. 413–424, March 2001.

[21] I. J. Birrer, E. M. Bracalente, J. Sweet, and G. Berthold, "σ^o signature of the Amazon rainforest obtained from the Seasat scatterometer", *IEEE Trans. Geosci. Remote Sensing*, vol. GRS-20, no. 1, pp. 11–17, 1982.

[22] M. Satake and H. Hanado, "Diurnal change of Amazon rain forest σ^o observed by Ku-band spaceborne radar", *IEEE Trans. Geosci. Remote Sensing*, vol. 42, no. 6, pp. 1127–1134, June 2004.

[23] W. Tsai, E. Graf, C. Winn, J. N. Huddleston, S. Dunbar, M. H. Freilich, F. J. Wentz, D. G. Long, and W. L. Jones, "Postlaunch sensor verification and calibration of the NASA scatterometer", *IEEE Trans. Geosci. Remote Sensing*, vol. 37, no. 3, May 1999.